^{11}C-acetate as an Imaging Biomarker of Radioresistance in Mouse Models of Non-Small Cell Lung Cancer

Emer Curley, MSc

Submitted in fulfilment of the requirements for the Degree of Doctor of Philosophy

Beatson Institute for Cancer Research

College of Medical, Veterinary & Life Sciences

University of Glasgow

September 2024

Abstract

Background

This thesis uses PET imaging to explore the use of ^{11}C-acetate, a radiotracer that maps fatty acid synthesis, as a predictive imaging biomarker of radioresistance in subcutaneous allografts and Genetically Engineered Mouse Models (GEMMs).

Aims/ Objectives

The primary aim of this project was to assess whether ^{11}C-acetate PET could be used as an imaging biomarker of radioresistance using LSL-Kras$^{G12D/+}$ Rosa26-LSL-Myc (KMyc) and Kras$^{G12D/+}$ p53$^{-/-}$ (KP) GEMMs and subcutaneous KP allografts. To ensure that the treatment was accurately delivered treatment verification was undertaken using γH2AX to verify the coverage of subcutaneous and GEMM tumours. A normal tissue study assessing aeration ratio and mean Hounsfield Units (HU) as methods of evaluating radiation induced lung damage was also performed using Cone Beam Computed Tomography (CBCTs) from the SARRP's onboard scanner.

Methods/Results

Statistically significant differences were found in the percentage of γH2AX positive nuclei between irradiated and unirradiated tumours in both the GEMM ($p=0.0055$) and subcutaneous ($p=0.0001$) groups, indicating that targeted tumours were being irradiated, and a statistically significant correlation between the change in aeration ratio from Week 0 to Week 4 and the survival time was found in the Radiation Induced Lung Damage Study (r_s = -0.94868, p (2-tailed) = 0.01385). In the ^{11}C-acetate PET study the KMyc cohort showed a statistically significant correlation between the ^{11}C-acetate SUVMax and the change in longest length (R^2=0.8786, $p=0.0058$).

Acknowledgements

I would like to thank my wonderful supervisors David Lewis and Anthony Chalmers for their help over the last several years, and the people in R07, M12, the Central Services team and the Beatson in general who were always around to make things easier whenever I needed it. It would be impossible to name everybody who helped me at the Beatson as everyone has been so kind, but in particular I would like to thank Katrina Stevenson, Gaurav Malviya, Irene Caldera-Quevedo, Robbie Bielik, Agata Mackintosh and Emma Johnson for their friendship and assistance over the years.

I would also like to thank my family and in particular my mother for their support, and my friends both inside the lab and out for listening to me talk about mice for four years and still spending time with me.

Author’s Declaration

I declare that I am the author of this thesis and that the work presented herein is my own unless explicitly stated otherwise in the text.

I confirm that no part of this thesis has been submitted for consideration of any other degree at the University of Glasgow or elsewhere.

Emer Curley

August 2024

Works Arising from Thesis

E. Curley, K. Stevenson, A. Mackintosh, G. Malviya, I. Caldera-Quevedo, A. Chalmers, D. Lewis	Poster Presentation (presenter) ^{11}C-acetate PET as an imaging biomarker of radioresistance	RadNet PhD and Postdoc Symposium 19/06/23
E. Curley, K. Stevenson, A. Mackintosh, G. Malviya, I. Caldera-Quevedo, A. Chalmers, D. Lewis	Poster Presentation (presenter) ^{11}C-acetate PET as an imaging biomarker of radioresistance	Association for Radiation Research Conference 4-6/06/23
E. Curley, K. Stevenson, A. Mackintosh, G. Malviya, A. Chalmers, D. Lewis	Poster Presentation (presenter) Pre-treatment ^{11}C Acetate PET/MRI as an Imaging Biomarker of Radioresistance	ScoRRF 10th Annual Scientific Meeting 10/11/22
E. Curley, K. Stevenson, A. Mackintosh, E. Johnson, G. Malviya, I. Caldera-Quevedo, A. Chalmers, D. Lewis	Poster Presentation (presenter) Metabolic Imaging for Precision Image Guided Lung Radiotherapy: Initial findings from subcutaneous tumour pilots	International PhD Student Conference Europe 14/06/21

Table of Contents

List of Figures

List of Equations

List of Tables

List of Abbreviations

^{18}F-FDG	^{18}F-Fludeoxyglucose
γH2AX	The phosphorylated form of H2A histone family member X
AAPM	American Association of Physicists in Medicine
ACC	acetyl-CoA carboxylase
ACSS2	acetyl-CoA synthetase enzyme
AIB	Alpha-Aminoisobutyric Acid
APPA	Ant-Post Parallel Opposed beams
BRAF V600	Proto-oncogene B-Raf V600
CBCT	Cone Beam Computed Tomography
CIP	Chest Imaging Platform
CO2	Carbon Dioxide
COPD	Chronic Obstructive Pulmonary Disease
CRUK	Cancer Research UK
CT	Computed Tomography
CTV	Clinical Target Volume
D100	Dose to 100% of the volume
DMEM	Dulbecco's Modified Eagle Medium
DNA	Deoxyribonucleic acid
DPC	Dose Painting by Contours
DPN	Dose Painting by Numbers
DSB	Double Stranded Break
DTA	Distance to Agreement
DVH	Dose Volume Histogram
EBRT	External Beam Radiotherapy
EGFR	epidermal growth factor receptor

FASN	Gene that encodes for Fatty Acid Synthase
FBS	Fasting Blood Sugar
FBS	Foetal bovine serum
FFPE	Formalin-Fixed Paraffin-Embedded
FLT	3′-Deoxy-3′-[18F]-fluorothymidine (FLT)
GEMM	Genetically Engineered Mouse Model
GLUT1	Glucose transporter 1
GPR	Gamma passing rate
GRE	Gradient echo sequence
GTV	Gross Tumour Volume
HIER	heat induced epitope retrieval
HU	Hounsfield Units
IHC	Immunohistochemistry
IMRT	Image Modulated Radiotherapy
KMyc	LSL-$Kras^{G12D/+}$ Rosa26-LSL-Myc
KP	$Kras^{G12D/+}$ $p53^{-/-}$
METex14	Mesenchymal Epithelial Transition exon 14 skipping mutation
MRI	Magnetic Resonance Imaging
NICE	National Institute for Health and Care Excellence
NOD	Nonobese diabetic
NSCLC	Non-small cell lung cancer
NSG	NOD.Cg-Prkdcscid Il2rgtm1
NTCP	Normal Tissue Complication Probability
NTRK	Neurotrophic tyrosine receptor kinase
OAR	Organs at risk
PBS	Phosphate buffered saline

PET	Positron Emission Tomography
PFU	Plaque forming units
PTV	Planning Target Volume
QA	Quality Assurance
QABB	Quality Assurance Ball Bearing
RET	Rearranged during Transfection
RGB	Red Green Blue
ROI	Region of Interest
ROS	Reactive Oxygen Species
SABR	Stereotactic Ablative Body Radiotherapy
SACT	Systemic Anti-Cancer Therapy
SARRP	Small Animal Radiotherapy Research Platform
SCID	Severe Combined Immunodeficiency
SCLC	Small Cell Lung Cancer
SUVMax	The maximum standard uptake value (highest uptake pixel in the ROI)
TCP	Tumour Control Probability
TG61	Task Group 61 (low energy dosimetry task group for AAPM)
TPS	Treatment Planning System
V100	Volume Receiving 100% of the Dose

1. INTRODUCTION

1.1 Overview

In this Chapter, non-small lung cancer, radiotherapy and Positron Emission Tomography will be discussed. The chapter will begin with a summary of the hallmarks of lung cancer, moving onto lung cancer subtypes and lung cancer as a cancer of unmet need. The principles behind radiotherapy and its use in the treatment of Non-Small Cell Lung Cancer (NSCLC) will then be discussed. Following this, Positron Emission Tomography (PET) and its use preclinically will be reviewed, and ^{11}C-acetate introduced as the tracer that this thesis focuses on. Treatment Planning for radiotherapy will be discussed, and finally the experimental objectives of the project and the hypothesis will be stated.

1.2 Non-small cell lung cancer: An introduction

1.2.1 What is lung cancer?

Like all cancers, lung cancer is the uncontrolled growth and division of cells and is characterised by features known as hallmarks of cancer. These six properties, originally proposed by Hanahan and Weinberg in their 2000 paper 'The Hallmarks of Cancer' (Hanahan & Weinberg, 2000) were updated in 2011 to include two further hallmarks and two enabling characteristics (Hanahan & Weinberg, 2011) and in 2022 to propose one additional hallmark (Hanahan, 2022). These hallmarks are summarised below in Figure 1.

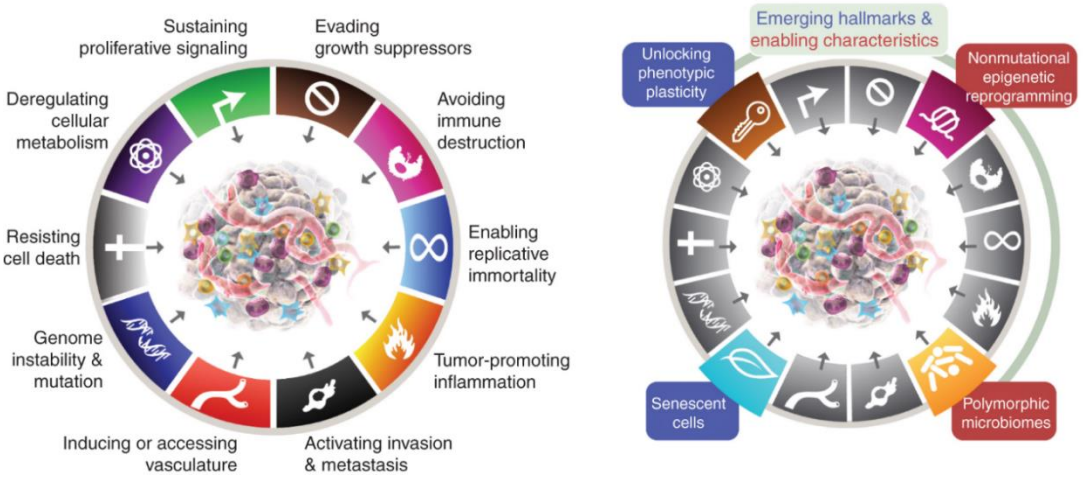

Figure 1. Summary of the Hallmarks of Cancer, reprinted from Cancer Discovery, January 2022, 12(1), 31-46, Douglas Hanahan, Hallmarks of Cancer: New Dimensions, with permission from AACR.

The hallmarks most relevant to this thesis and how they are exploited by radiotherapy will be discussed in section 1.

1.2.2 Lung Cancer Subtypes

Most lung cancers (~99%) can be broadly classified into two groups; small cell lung carcinoma (SCLC) and non-small cell lung carcinoma (NSCLC) (Ettinger et al, 2022) with NSCLC the most commonly diagnosed of the two. NSCLC can be further divided into different subtypes that vary by cell of origin:

- Adenocarcinoma: The most common form of lung cancer, this subtype of lung cancer originates in the epithelial cells in the outer lining of the lungs and accounts for 40% of lung cancers.
- Squamous cell carcinoma: making up 25% of lung cancers, squamous cell carcinoma originates in the squamous cells of the inner lung lining.
- Large cell carcinoma: an undifferentiated tumour that looks neither like adenocarcinoma nor squamous cell carcinoma and constitutes 10% of lung cancers.

1.2.3 Lung Cancer as a Cancer of Unmet Need

Treatments for NSCLC vary based on subtype, stage, treatment intent (radical or palliative) and the capacity of the patient to tolerate the treatment, with patients usually receiving at least one and often a combination of surgery, chemotherapy, or radiotherapy (NICE, 2024). The prognosis for lung cancer in the UK remains poor, with only 9.5% of 2013-2017 patients predicted to survive ten years or more post treatment (CRUK, 2023a), and it is the cancer that had the second smallest improvement in survival from 1971-1972 to 2010-2011 (CRUK, 2023b).

There are many contributing factors to the lack of improvement in outcomes for lung cancer. Firstly, patients are often diagnosed at a late stage. This happens even when patients present early because their symptoms often mimic those of other respiratory conditions such as Chronic Obstructive Pulmonary Disease (COPD) (Ellis and Vandermeer, 2011) that are common in the smokers that make up the majority of lung cancer patients in the UK, with 72% of lung cancers caused by smoking (CRUK, 2023a). Secondly, lung cancer generally and NSCLC specifically are heterogenous diseases, with oncogenic mutations and metabolic variations causing differing treatment responses even in cancers of the same subtype (Das et al, 2010; Tang et al, 2018). The poor prognosis and complications surrounding the treatment of lung cancer led Cancer Research UK (CRUK) to name lung cancer as one of the cancers of unmet need in the UK and granting additional funding to research surrounding it (CRUK, 2015).

The benefits from the increased focus on lung cancer are already being reflected in the treatment pathways for NSCLC. A recent update to the NICE guidelines included guidance on personalised Systemic Anti-Cancer Therapy (SACT) pathways for advanced NSCLC that account for how oncogenic mutations affect the viability of certain treatments. Examples of oncogenic mutations that affect treatment efficacy include:

- KRAS G12C, which is a KRAS mutation that triggers uncontrolled cell growth and increases treatment resistance (O'Sullivan et al, 2023).
- RET fusion, where kinase activation causes increased cell proliferation and survival (Novello et al, 2023).
- NTRK fusions, which encode TRK fusion proteins that drive cancer growth (Cocco et al, 2018).
- METex14 skipping mutations, which lead to the activation of signalling pathways involved with proliferation and survival of cancer cells (Socinski et al, 2021).
- BRAF V600, which activates the BRAF protein kinase to promote cell growth (Kiel et al, 2016).

Distinct treatment pathways have been identified for all of the above mutations (NICE, 2024). These additions validate the argument that stratified treatments for NSCLC that recognise the heterogeneity of the disease are the way to improve outcomes for patients.

However, these guidelines focus on chemotherapy and other drug therapies, and include only oncogenic mutations as an additional way to stratify treatment in addition to more conventional methods like staging and histological subtype. This means that further research into topics such as how to adjust treatments like radiotherapy to account for sources of tumour heterogeneity like metabolic phenotype remain potentially fruitful avenues for the development of personalised treatments. The metabolic phenotype of a cancer describes how it utilizes different substrates. Cancer cell metabolism is often abnormal (Park et al, 2020), which can be exploited in treatment and for the development of imaging biomarkers, which will be discussed further in Section 1.4.

1.3 Radiotherapy as a treatment for lung cancer

1.3.1 What is radiotherapy?

Radiotherapy in cancer treatment involves using ionising radiation to damage the DNA of cancer cells. There are several radiotherapy treatment modalities available in the UK. These include external beam radiotherapy, which uses high energy X-rays; particle radiotherapy, which uses charged particles; and internal radiotherapy, which involves the insertion of a radioactive source into the patient. As external beam radiotherapy is the form most used in the treatment of lung cancer this modality will be focused on for the remainder of the introduction.

The purpose of radiotherapy is to deliver sufficient dose to tumour while sparing the surrounding normal tissue. The therapeutic ratio is the ratio of probability that a tumour will be controlled by the treatment, the Tumour Control Probability (TCP) and the probability of adverse effects on the normal tissue, the Normal Tissue Complication Probability (NTCP). Another concept relating to the balance between effective treatment and toxicity is the therapeutic window, which unlike the therapeutic ratio refers to a range of doses rather than a ratio of probabilities (Chang et al, 2014). The therapeutic ratio is generally graphically represented on a dose response curve, and an example of this can be found in Figure 2.

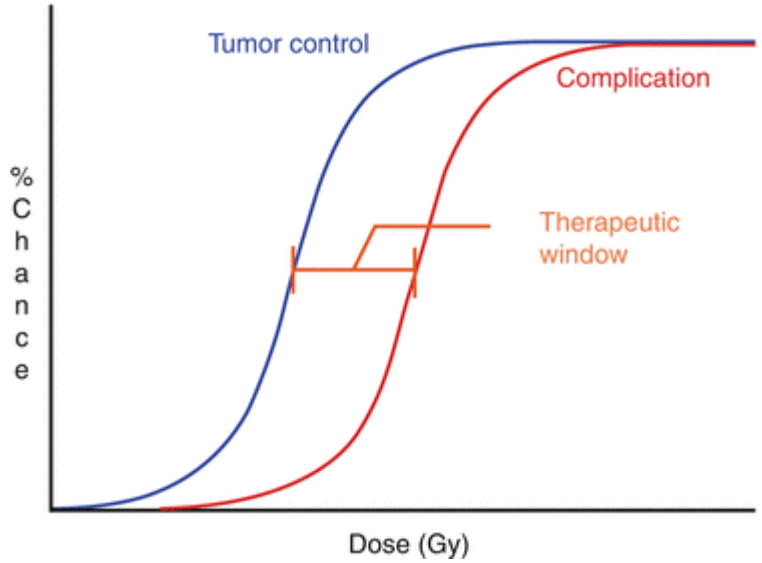

Figure 2. Dose response curve showing a representation of the therapeutic window reprinted from Chang et al, Therapeutic Ratio, Basic Radiotherapy Physics and Biology, Fig. 27.3, 2014, Springer Nature with permission.

The X axis is the dose delivered in Gray and the Y axis represent the percentage chance of tumour control (the blue line) and complications (shown by the red line). The therapeutic window is the range of doses in the region where the probability of complications is low, and the probability of tumour control is high.

1.3.2 X-ray interactions with matter

Ionising radiation is radiation with sufficiently high energy to remove a valence electron from an inner shell. This can occur through direct ionisation, which occurs during charged particle collisions due to electrostatic force, and indirect ionisation, which is the kind of ionisation that occurs during photon beam therapy. The three most common forms of indirect ionisation are pair production, Compton scattering and the photoelectric effect, seen in Figure 3.

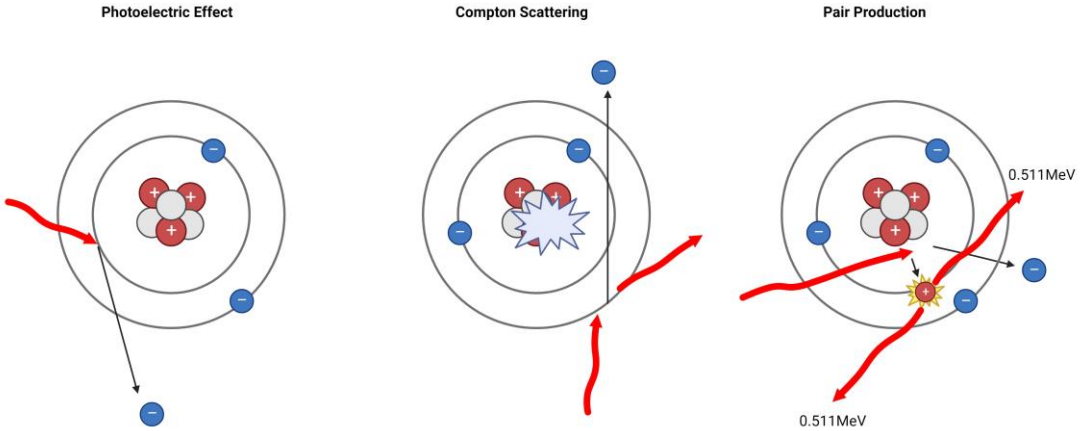

Figure 3. Summary of X-ray interactions with matter.

The photoelectric effect (left) occurs when a photon is completely absorbed by an inner shell electron, resulting in the emission of a photoelectron. Compton scattering (middle) happens when a photon imparts some of its energy to an outer shell electron, resulting in a scattered electron and the emission of a Compton electron. Pair production occurs when photons with an energy of at least 1.022MeV create an electron-positron pair near a nucleus, resulting in the annihilation of the positron with a free electron and the emission of two antiparallel 0.511 keV photons. Created in Biorender.com

Compton scattering is most prevalent at energies commonly used in clinical and preclinical radiotherapy (Abeloff et al, 2008). Note that, as shown in Figure 3, this process results in the loss of an electron and the ionisation of the material being interacted with, which is fundamental to the indirect damage that constitutes the two thirds to three quarters of damage done by external beam radiotherapy (EBRT) (Beyzadeoglu, Ozyigit & Ebruli, 2010).

1.3.3 Direct and indirect action of radiation on DNA

DNA damage caused by radiotherapy can either be direct or indirect, with direct damage being caused by dose deposition in the atoms of the cancer cell's DNA and indirect damage being caused by the downstream effects of the radiation's interaction with other molecules surrounding the DNA. Direct and indirect action of radiation and the types of damage that can result are detailed in Figure 4.

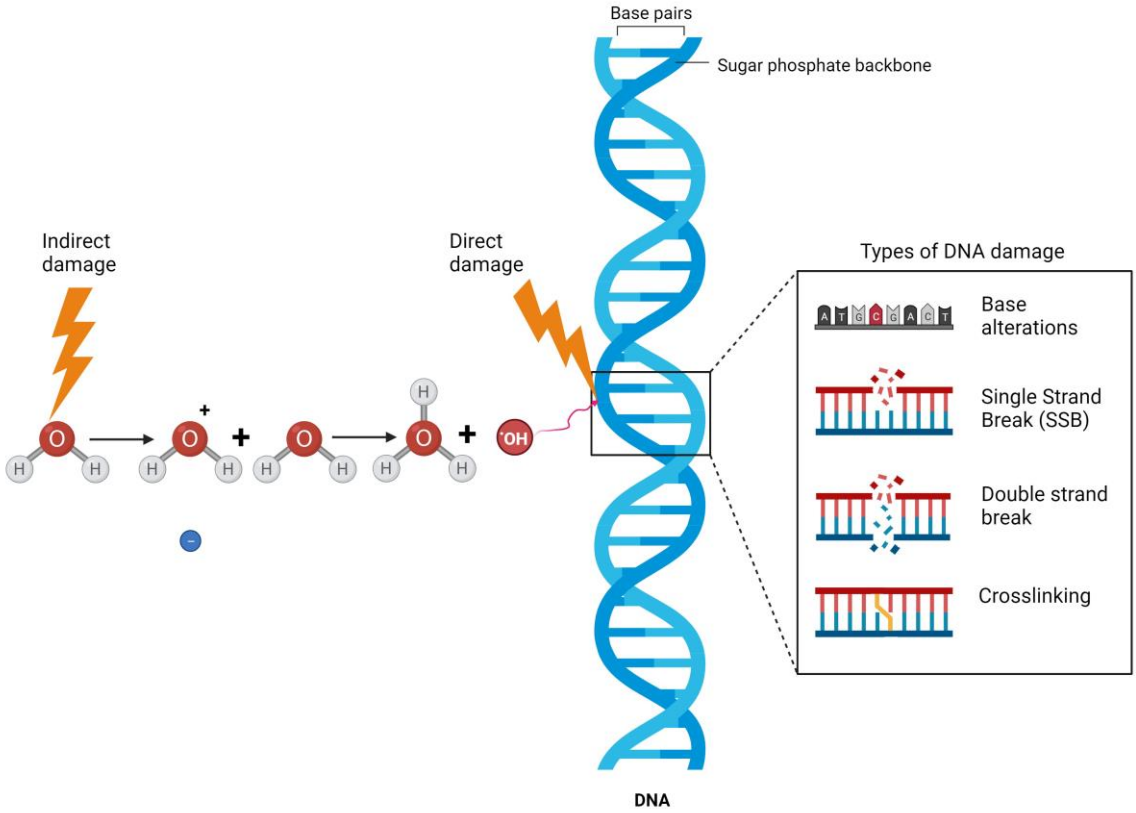

Figure 4. Summary of mechanisms of radiation induced DNA damage and repair.

This figure shows how radiation can interact with the DNA itself to cause direct damage and with the molecular environment to cause indirect damage using hydroxyl production as an example. Other free radical and Reactive Oxygen Species (ROS) can also be created by indirect action. Created in Biorender.com.

As shown in Figure 4, the same kind of damage can be caused by both the direct action of radiation and the indirect action, although direct action induces double stranded breaks (DSB) more often. Cells are particularly sensitive to radiation induced DNA damage during G2 and M phase (Hall & Giaccia, 2006); this is because in M phase the DNA is exposed and because DNA damage that happens during G2 phase may not be detected and adequately repaired prior to replication, which can result in cell death through a process called mitotic catastrophe even after sublethal damage (Sazonova et al, 2021).

1.3.4 Exploiting the vulnerabilities of cancer cells with radiotherapy

Figure 5 summarises the relationship between radiation biology concepts and the Hallmarks of Cancer (see Figure 1 for the original diagram of the Hallmarks of Cancer).

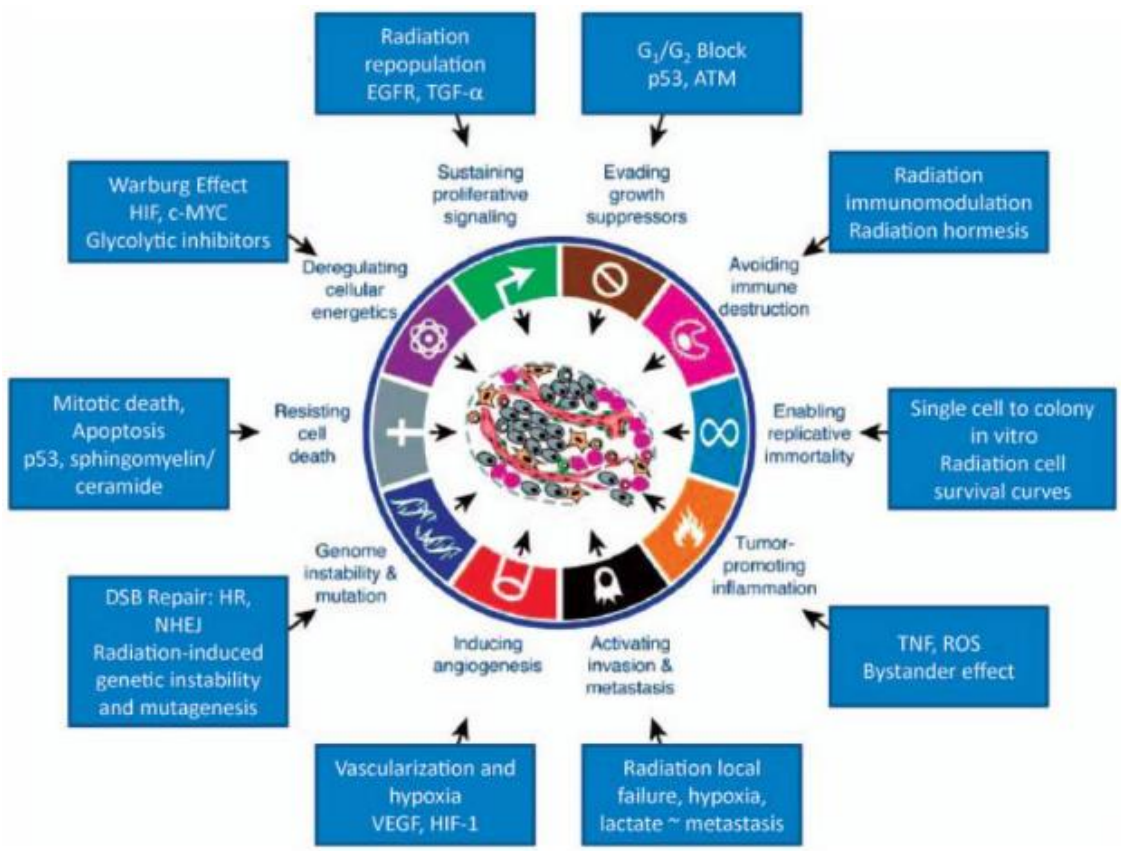

Figure 5. Summary of radiation biology and the Hallmarks of Cancer

This was reprinted from Figure 5 of Radiation Research, May 2014, 181(6), 561-577, Boss, Bristow and Dewhirst, Linking the History of Radiation Biology to the Hallmarks of Cancer, with permission from the Radiation Research Society (© 2024 Radiation Research Society).

In particular, the following Hallmarks can be exploited or circumvented by radiotherapy: Resistance to Cell Death; Genome Instability and Mutation, Sustaining Proliferative Signalling, Tumour-Promoting Inflammation and Evading Growth Suppressors.

The capacity of cancer cells to sustain proliferative signalling, evade growth suppressors and enable replicative immortality (Hanahan & Weinberg, 2010) ensures that they often divide and replicate at much higher rates that normal

tissue. As discussed in the previous section, cells are especially sensitive to radiation during division, and since cancer cells have a high proliferative capacity, they are more likely to be in a radiosensitive state compared to the cells in most normal tissues.

Radiotherapy can also have a beneficial effect on the ability of the immune system to identify and kill cancer cells, counteracting the cancer's ability to avoid immune destruction. Radiation exposure can promote tumour antigen presentation, improving the capacity of the immune system to recognise the cancer (Wu et al, 2017). Radiation can also influence metastasized tumours that are outside the target volume. This effect is known as the abscopal effect and occurs as the result of antigens that are released when a tumour is exposed to radiation. These antigens prompt a systemic immune response that targets unirradiated tumours (Craig et al, 2021).

However, the effects of radiation on the immune system are dependent on the dose, the volume and the target; for example, low doses of radiation can have an immunosuppressive effect that is utilised as an osteoarthritis treatment in some countries (Dove et al, 2022). Conventional radiotherapy often generates immunosuppressive effects (Ladbury et al, 2019) that negatively affect therapeutic outcomes and potentially induce radiation-induced lymphopenia, especially when large volumes are irradiated (Wirsdörfer et al, 2016; Tubin et al, 2020). As such, while radiotherapy can be immunostimulatory this is highly dependent on the specific nature of the radiotherapy treatment.

The ability of cancer cells to induce angiogenesis is exploited by radiotherapy treatment methods. As tumours grow the core slowly becomes starved of oxygen as more distance is created between the centre and the surrounding blood supply, leading to the formation of a highly radiotherapy resistant necrotic core as the absence of oxygen decreases the chance of irreparable DNA damage in accordance with the oxygen fixation hypothesis (Hall & Giacca, 2012), which is the principle that the presence of oxygen permanently 'fixes' the DNA damage caused by free radicals. When treated with radiotherapy often only the outer part of the tumour is initially affected by the radiation; however, because of the tumour's capacity for angiogenesis the inner part can quickly reoxygenate, an effect observed as early as 1955 by Thomlinson and Gray (Thomlinson & Gray,

1955). To accommodate this, it is common for radiotherapy treatments to be fractionated, a process which both radiosensitizes the previously necrotic core and reduces the risk of normal tissue complications by giving the normal tissues, which has a better capacity for repair than most tumour cells, a chance to recover.

1.3.5 Challenges in Radiotherapy for NSCLC

Radiotherapy is often used to beneficial effect in NSCLC, with one study of 288,670 Americans showing it improved survival across all ages, genders and histological subtypes (Cheng et al, 2019). However, there are still many complications associated with it that largely arise from the significant inter- and intratumour heterogeneity exhibited, with genetic and metabolic variations resulting in large disparities in treatment responses.

Intratumour heterogeneity in NSCLC is apparent both genetically and metabolically. NSCLC has been shown to exhibit signs of branched mutations and genomic alterations that vary based on what part of the tumour is sampled (De Bruin et al, 2014). De Bruin's paper suggested that this would be a problem for the efficacy of targeted drug therapies but given the wide variation in radiation response noted within the same subtypes of NSCLC, particularly adenocarcinoma (Carmichael et al, 1989) it is possible that these genetic variations could cause an uneven treatment response to radiotherapy as well. Intratumour metabolic heterogeneity occurs both as a function of genetic heterogeneity (Lv et al, 2023) and because of the tumour microenvironment, with poorly perfused parts of NSCLC tumours utilizing glucose and better perfused volumes using other substrates (Hensley et al, 2016).

The cause of intertumour heterogeneity can vary from oncogenic mutations like KRAS G12C to metabolic adjustments such as enhanced glycolysis and the ability to rely on a diverse range of nutrients to support proliferation (ibid). One particularly interesting metabolic pathway that varies between different tumours in NSCLC is fatty acid synthesis.

The fatty acid synthesis pathway consists of a series of enzyme catalysed reactions where acetyl-CoA are converted to long chain fatty acids. Fatty acid

synthase (FASN) is one of the key enzymes in this process. Figure 6 depicts this pathway in detail.

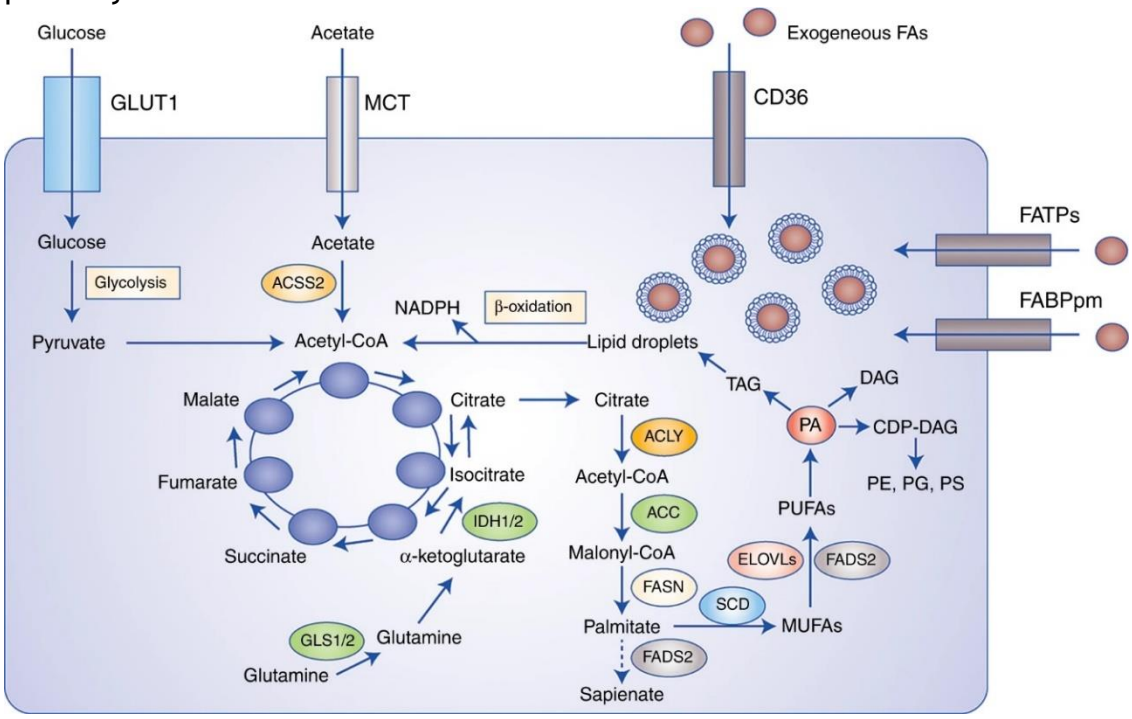

Figure 6. Diagram showing an overview of the metabolic pathways for fatty acid synthesis, reproduced from Figure 2 of British Journal of Cancer, 2020, 122, 4-22, Nikos Koundouros & George Poulogiannis, Reprogramming of fatty acid metabolism in cancer.

Acetyl-CoA can be converted from pyruvate through glycolysis from glucose transported through GLUT1 transporters, and from acetate which is converted by ACSS2 that is transported through MCT transporters. Acetyl-CoA produces citrate in the TCA cycle, which is converted to acetyl-CoA by ACLY. ACC converts acetyl-CoA to malonyl-CoA, which is then converted to palmitate by FASN.

Fatty acid synthesis is known to support membrane creation and repair (Currie et al, 2013), the formation of lipid rafts that contain many proteins relevant to signalling (Fu et al, 2021) and produce triglycerides that can act as an energy store (Cheng et al, 2022), all of which contribute to radioresistance. Additionally, hypoxic tumours (Mylonis, Simos & Paraskeva, 2019) and cancer STEM cells (Li, Feng & He, 2020), both of which are notably radioresistant, upregulate fatty acid synthesis.

Tumour biopsies can provide useful information on some tumour characteristics; however, because of the spatial heterogeneity within the tumours and the fact that NSCLC often undergoes metabolic reprogramming to sustain its growth and proliferation (Eltayeb et al, 2022) single biopsies are unable to provide

information on the tumour as a whole or predict how it will react over time. Even studies with multiple biopsies are limited due to their inability to longitudinally monitor tumour progression without subjecting patients to repeated invasive procedures and still do not provide an overview of the whole tumour. One non-invasive method that allows for data collection proximate to radiotherapy treatment with minimal discomfort to the patient, something that can be achieved for the metabolic shifts in cancer using nuclear imaging, specifically Positron Emission Tomography (PET).

1.4 Positron Emission Tomography

1.4.1 What is positron emission tomography?

Positron Emission Tomography (PET) imaging is a functional imaging technique that visualizes and quantifies physiological processes in the body. It involves the use of radiotracers, which are short-lived radioactive compounds labelled with positron-emitting isotopes such as ^{18}F or ^{11}C that are injected, ingested or inhaled by the patient.

PET radiotracers are compounds of biologically active molecules, which will be preferentially taken up by certain cells, and radionuclides, which will decay allowing localisation of the PET radiotracer (Schrevens, 2004). The radiotracer is 'trapped' within the cell, either temporarily or permanently, with the antiparallel 0.511 MeV photons created as a result of annihilation of the positron in the attached radionuclide's decay chain detected in co-incidence to generate a signal that corresponds to the amount of the radiotracer accumulated in a region (ibid). The radiotracer most commonly used clinically is ^{18}F-FDG. FDG is a glucose analogue, and the preference for aerobic glycolysis in malignant cells relative to healthy cells makes it an attractive radiotracer for the detection of many cancers (Liberti & Locasale, 2016). Despite its undeniable usefulness, ^{18}F-FDG only provides information regarding glucose metabolism, and the potential benefits that further information on the uptake of particular metabolites in response to and prior to radiotherapy could provide has led to the development of different PET radiotracers that explore several metabolic pathways.

While PET has utility, it also has a number of limitations. One such limitation is its precision, with PET scans often being noisier than CT and MRI scans and having lower resolutions (Teymurazyan et al, 2012). Sources of noise include local statistical noise caused by attenuation in the body reducing the count rate (Kitamura et al, 2010) and respiratory motion or movement of the mouse. Additionally, issues that affect the distance between detected effects and the location of the tracer in the body such as scattering, attenuation and the range the positron travels prior to annihilation all contribute to an effect known as the partial volume effect, where the uptake in smaller tumours is underestimated due to the limited resolution of the modality (Soret et al, 2007). This can be

particularly problematic in preclinical experiments given the size of the tumours being imaged. These factors can also lead to misalignment between the PET and the MRI or CT that it is registered to, which in turn can affect the accuracy of any subsequent regions of interest drawn for analysis and the tracer uptake within them (Vogel et al, 2007).

Practically, PET imaging can be expensive compared to CT and MRI, more novel radiotracers can be difficult to source, and many hospitals do not have the necessary facilities for PET imaging. The length of the scans can also cause discomfort for patients who struggle to lie still for long periods of time. This means that to justify the use of PET there needs to be a strong indication that it could provide clinical benefit.

This evidence exists for some radiotracers; for example, the radiotracer most commonly used clinically is ^{18}F-FDG. FDG is a glucose analogue, and the preference for aerobic glycolysis in malignant cells relative to normal cells makes it an attractive radiotracer for the detection of many cancers (Liberti & Locasale, 2016). As ^{18}F-FDG only provides information regarding glucose metabolism, the potential benefits that further information on the uptake of other metabolites could provide predictively and in examining radiotherapy response has led to the development of different PET radiotracers that explore several metabolic pathways.

1.4.2 ^{11}C-acetate PET

The majority of PET guided radiotherapy research focuses on ^{18}F-FDG and hypoxia tracers as the mechanisms behind how these pathways influence radiosensitivity are relatively well established (Young et al, 1999) (Rockwell et al, 2009). However, as recent research in NSCLC has indicated that fatty acid synthesis may be a predictor of radioresistance (Zhan et al, 2018), research into the radioresistance of tumours with avidity for ^{11}C-acetate and the possibility that fatty acid radiotracers can provide metabolic information in vivo regarding radioresistance that might be clinically relevant seems justified. Previous research has indicated an ability for ^{11}C-acetate to detect fatty acid avid, slow growing, lung tumours, which would have been a false negative on ^{18}F-FDG scans

(Nomori et al, 2008). Establishing whether the biological information obtained from ^{11}C-acetate scans can be used either prognostically to establish how well a tumour will respond to radiotherapy or for adaptation of treatment regimens to account for inter-tumour heterogeneity has obvious translational potential.

1.4.3 Preclinical radiotracers for Lung Cancer

To investigate what radiotracers are currently being developed in the preclinical setting and what they are being used for, a literature search focused on PET guided preclinical radiotherapy of the lung was performed using Scopus. The purpose of this search was to ensure that any research that was planned was novel and to establish what characteristics radiotracers chosen for the purposes of this project would need to have.

The following search terms were used:

image OR imaging OR imageable OR scan OR scanning OR scannable OR PET OR "positron emission tomography"

AND

pre*clinical OR mouse OR mice OR "small*animal*" OR “in*vivo”

AND

radiotherapy OR "radiation therap*" OR "radiation treatment*" OR "irradiation therap*" OR "irradiation treatment*" OR "X-ray therap*" OR "X-ray treatment*" OR "gamma therap*" OR "gamma treatment*"

AND

lung* OR SCLC OR "small*cell lung" OR NSCLC OR "non*small*cell lung" OR "lung W/8 Adenocarcinoma" OR "lung W/8 squamous cell" OR "lung W/8 large cell carcinoma" OR "Undifferentiated non*small cell lung")

Exclusion Criteria

- Primary focus of the paper should be on image guided radiotherapy, papers where adjuvant radiotherapy is administered alongside another treatment which is the primarily focus of the research will not be

considered to avoid attributing the results of the other treatment to the radiotherapy.

- Preclinical studies involving animals other than mice and clinical studies will be excluded due to biological differences between the animals.
- Studies without a PET element excluded as these are not relevant to the thesis.
- Guidelines and grey literature have not been included as guidelines are not original research and grey literature can be subject to less rigorous review. However, if guidelines pointed towards specific papers that are relevant to the topic these would have been included.
- Radiotherapy modalities other than external beam radiotherapy were excluded as this does not fit the scope of this thesis.
- If no therapeutic irradiation occurs, the paper will be excluded to avoid including papers where radiation is used for purposes such as inducing tumour growth.

1.4.4 Literature Review on Preclinical PET

In total 118 search results were reviewed and 6 met the criteria described in section 1.4.3. All the papers included had been published in academic journals and been subject to peer review.

Dose Painting

In dose painting, standard uptake values (SUVs) representing the tracer uptake within the tumours are used to identify areas for dose escalation. Doses are "painted" either with discrete thresholds, where regions are defined by contours (dose painting by contours or DPC) or a continuous assignment of doses based on the brightness of the individual voxels (dose painting by numbers or DPN) (Thorwarth, Geets & Paiusco, 2010). Li et al's 2019 paper focused on dose painting with ^{18}F-FLT. This is a tracer that is used to map tumour and cell proliferation. In the paper it is being assessed for its ability to identify areas of accelerated repopulation and increased tumour cell proliferation for enhanced

irradiation. This was demonstrated by significant correlation ($p < 0.001$) between the ^{18}F-FLT uptake and the Ki-67 labelling index retrieved through immunohistopathology (Li et al, 2019). Another review study corroborated this relationship (Zhang et al, 2017). As accelerated repopulation is associated with poorer prognosis and recurrence, the option to target relevant areas and escalate would be invaluable (Corry & Rischin, 2004). Hypoxia tracers, like ^{18}F-EF5, have value for the same reason as imageable hypoxia is of similar prognostic value (Ali et al, 2015).

While ^{18}F-FLT has not been the subject of any large dose painting clinical trials and the results from ongoing hypoxia trials are not yet available, research into ^{18}F-FDG dose painting is much more advanced. As with ^{18}F-FLT and ^{18}F-EF5, ^{18}F-FDG imaging is potentially valuable because local recurrence in NSCLC has been shown to be primarily located in areas of high uptake of ^{18}F-FDG (Abramyuk et al, 2009) (Aerts et al, 2009). Perhaps the biggest difference is that ^{18}F-FDG uptakes remain relatively stable throughout fractionated treatments, while both ^{18}F-FLT (Qu et al, 2015) and ^{18}F-EF5 (Zhang et al, 2017) vary between fractions. The changes between fractions are expected for ^{18}F-FLT and ^{18}F-EF5 as ^{18}F-FLT is a proliferation marker and ^{18}F-EF5 is a hypoxia marker, both of which would change as radiotherapy perturbs cell division by damaging DNA (Liu et al, 2021) and fractionated radiotherapy can lead to iterative reoxygenation of previously hypoxic regions of the tumour (Beckers et al, 2024).

It appears from initial ^{18}F-FDG trials that dose painting by contour is feasible clinically, and that the dose boosts do not significantly impact mean tumour dose. One randomised phase II trial showed that mean doses of 86.9 Gy (± 14.9 Gy) could be achieved in boosted regions, while maintaining a similar mean dose across the tumour (77.3 Gy ± 7.9 Gy for the non-boosted volumes 77.5 Gy ± 10.1 Gy for the boosted volumes) (Van Elmpt et al, 2012). However, to achieve the desired escalation the dose to the OARs was increased until it was close to the threshold (ibid), a decision which may have factored into the increased risk of both early and late radiation side effects noted for PET-boost patients in the recent follow-up to this trial (Van Diessen et al, 2019).

Normal tissue response

The increased OAR toxicity in the ^{18}F-FDG trial highlights the risks of prioritizing tumour control probability (TCP) over Normal Tissue Complication Probability (NTCP), particularly in patients with a poor prognosis, as side effects could significantly impact quality of life with minimal benefit. One way to reduce NTCP would be to utilize PET not only as a means of understanding the tumour microenvironment but also to monitor changes in the surrounding tissue before, during and after irradiation, which can theoretically be done using some of the same radiotracers used for tumour imaging. As well as the possibility of using ^{18}F-FLT and ^{18}F-EF5 as measures of post radiotherapy response, one preclinical ^{18}F-FDG paper found uptake in normal tissue post Irradiation (Kesner et al, 2008). Lung tissue showed a 16% average increase in FDG uptake post irradiation relative to the baseline ($p < 0.0001$), a response posited to be related to radiation induced inflammation (ibid). ^{18}F-FDG as a measure of inflammatory response to radiation is particularly relevant due radiation pneumonitis, a severe early radiation effect with treatment limiting and, in severe cases, potentially life-threatening consequences (Wang et al, 2002). Clinical studies verify this relationship between FDG avidity and radiation pneumonitis prognosis post treatment (Hassabella et al, 2005), (McCurdy et al, 2012), (Adjari et al, 2019) and also indicate that increased signal in FDG PET can identify pre-treatment inflammation in the lung due to increased FDG uptake, which can be used to determine what parts of the lung may be particularly sensitive to radiation pneumonitis prior to irradiation, with research confirming the correlation between this and pre-treatment FDG uptake (Petit et al, 2011), (Castillo et al, 2014), information that would be invaluable to treatment planning.

Tumour Response

However, the FDG avidity of inflamed tissue can also mask metabolic changes within the tumour, limiting the efficacy of ^{18}F-FDG as an early metric of tumour response to irradiation (Tsuji et al, 2015). The final study in the review proposes 3-^{11}C- Alpha-Aminoisobutyric Acid (AIB), with AIB being a stable non-natural amino acid with less normal tissue uptake than other amino acid tracers, as an alternative to ^{18}F-FDG to examine early metabolic response to radiation. As the lack of correlation between 3-^{11}C-AIB uptake, apoptosis and proliferative activity

indicates that the former two processes are not likely to have significantly influenced the uptake (ibid), 3-^{11}C-AIB uptake could effectively be interpreted as a surrogate for the immediate efficacy of radiotherapy.

1.4.5 Developing ^{11}C as an imaging biomarker for radioresistance

In the previous section, four radiotracers that exploit different metabolic pathways were explored: ^{18}F-EF5, a hypoxic tracer; ^{18}F-FDG, a glycolic tracer; ^{18}F-FLT, a proliferation tracer; and 3-^{11}C-AIB, an amino acid tracer. While ^{11}C-acetate, as a method of diagnosis and staging for tumours with preferential fatty acid uptake such as the prostate, is an active field of research (Nitsch et al, 2016), far less attention has been paid to the possibility of using ^{11}C-acetate to inform radiotherapy treatments, as shown by the fact that none of the studies focused on ^{11}C-acetate or even fatty acid synthesis tracers in general. This shows that there is a gap in literature that this project could address to produce novel research.

Having reviewed the other radiotracers, it is apparent that the following things should be investigated to assess ^{11}C-acetate's suitability.

- **What any variation we measure represents:** whether any fluctuations in ^{11}C-acetate uptake correlate with biological mechanisms that could influence radiotherapy outcomes
- **Whether there is overlap between the information provided by this tracer and others:** whether ^{11}C-acetate provides novel information that is relevant to radiotherapy treatments or if other tracers provide the same information. This particularly relevant in comparison glucose avidity as clinicians will be unwilling to use a radiotracer with a short half-life that is more difficult to administer if there is an easier established alternative (in this case ^{18}F-FDG).
- **Response to radiotherapy:** whether the models that we use sufficiently respond to radiation.

However, before beginning experiments to test whether our models adequately respond to radiotherapy it is necessary to ensure that any radiotherapy

treatments we deliver are delivered as planned, create clinically relevant normal tissue sparing plans insofar as is reasonably possible and understand how the limitations of our preclinical treatment delivery systems might affect our experiments.

1.5 Treatment Plan Verification

1.5.1 What is Radiotherapy Treatment Planning?

Radiotherapy treatment planning is the process of producing a personalised plan adapted to the individual anatomy of the patient and the shape of the tumour. Treatment planning is usually based on CT scans as these provide electron density maps that allow the treatment planning system to calculate the dose deposited in the patient using dose calculation algorithms. However, it is common to use Magnetic Resonance Imaging (MRI) scans to complement the CT scans in sites that would benefit from improved soft tissue contrast and increasingly even as the basis for planning with the aid of synthetic CT images generated from the MRI scans (Owrangi, Greer & Glide-Hurst, 2018).

To create a treatment plan, it is necessary to identify and delineate both the tumour and organs at risk (OARs) around the tumour as sparing normal tissue as much as possible is necessary to reduce the incidence and severity of radiotherapy related complications post treatment. Figure 7 gives a breakdown of how the tumour margin is grown to ensure coverage and how this can result in the OARs receiving high doses of radiation.

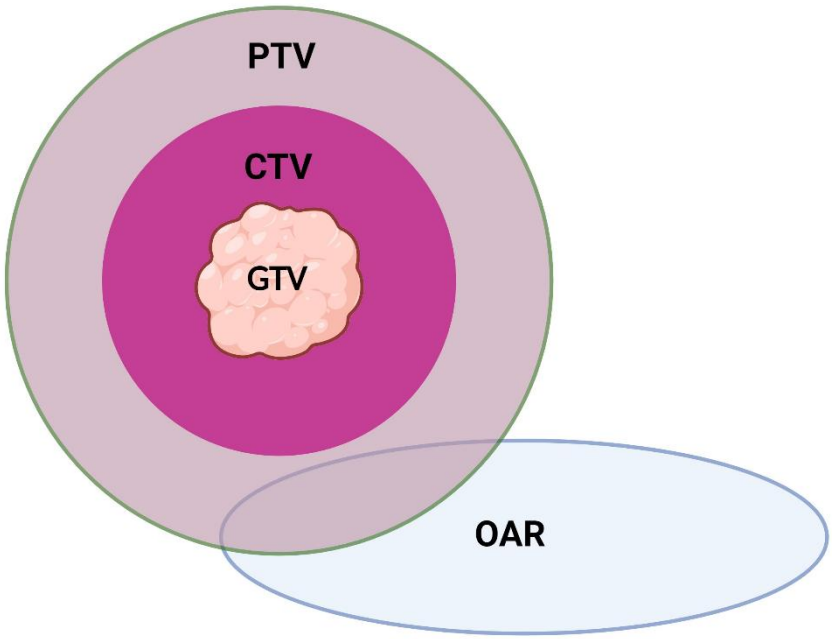

Figure 7. Diagram showing the target volumes used in a conventional forward planned 3D conformal radiotherapy plan and an overlapping OAR.

These volumes are the Gross Tumour Volume or GTV, which is the palpable or imageable tumour volume, the Clinical Target Volume or CTV, which is grown from the GTV to account for subclinical spread, and the Planning Target Volume or PTV, a volume which is grown from the subclinical spread to account for uncertainty. More complicated plans such as those for inverse planned Image Modulated Radiotherapy (IMRT) will contain additional volumes. The intersecting OAR shows how the margins necessary for covering the tumour entirely can result in dose to surrounding critical structures. Created in Biorender.com.

Balancing the probability of tumour control with the likelihood of damaging the normal tissue is known as the therapeutic ratio and is expressed below in Equation 1.

$$Therapeutic\ ratio = \frac{TCP}{NTCP}$$

TCP= Tumour Control Probability

NTCP= Normal Tisue Complication Probability

Equation 1: Formula for the therapeutic ratio in radiotherapy.

To optimise this ratio the angle, motion and energy of beams is varied to improve tumour dose and minimise the dose to the normal tissue. How well a plan fulfils these objectives is measured by creating graphs for each region of interest (ROI) called ‘dose volume histograms’ (DVHs).

1.5.2 What is Dose?

In a clinical setting therapeutic irradiation and accidental exposures are most often expressed in terms of the absorbed dose. This is generally expressed in terms of Gray, but its base unit is J/kg. The equation for absorbed dose can be seen below in Equation 2.

$$AD = \frac{d\,\bar{\in}}{dm}$$

d$\bar{\in}$=mean energy (J)

dm=mass (kg)

Equation 2. Absorbed dose formula

1.5.3 Dose Volume Histograms and Quality Metrics

While dosimetry allows medical physicists to check the function of their machines, dose volume histograms (DVHs) are a quality check for the physicists themselves, specifically their treatment plans. DVHs relate the radiation dose to the volume of tissue that it irradiates for any outlined ROIs such as the tumour or surrounding OARs. An example of a DVH for tumours in genetically engineering mouse models (GEMMs) can be found below in Figure 8.

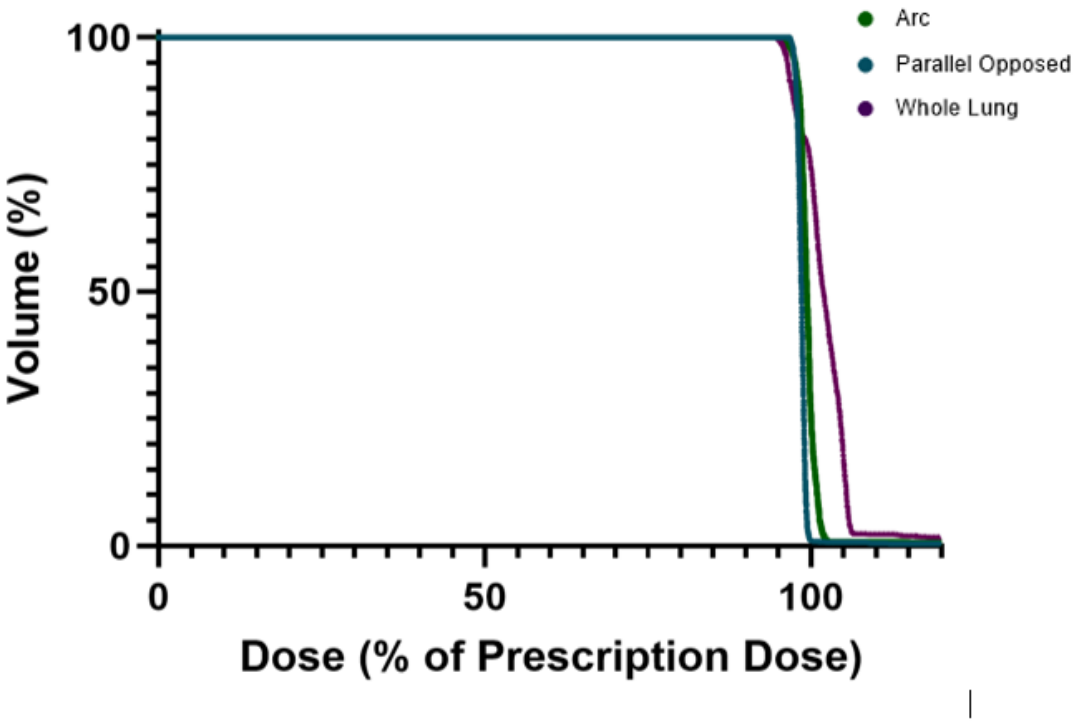

Figure 8. Dose Volume Histogram showing the average doses to tumours across 3 different plan types (Arc, parallel opposed beams targeted on individual tumours and a whole lung ant-post parallel opposed pair) for KP GEMM mice (N=8).

An ideal graph for tumour coverage should look like a right angle at 100% as this would indicate that the tumour is receiving 100% of the prescription dose and there are no regions receiving more than 105% of the prescription dose (these regions are known as 'hot spots'). From this graph we can see that the tumours are covered well by all three plans, and that only the whole lung plan results in hot spots.

The quality of the plan is then assessed by pulling values from these graphs and comparing them to plan quality metrics.

The most common quality metrics are variations on dose to a certain percentage of the volume (DXX) and volume receiving a certain percentage of the dose (VXX). An example of each is D50 (the minimum dose to 50% of the volume) and V95 (the percentage of the volume that received 95% of the dose).

1.5.4 How do preclinical and clinical treatment plans differ?

The margins, quality metrics and treatment planning methods in clinical treatment plans are informed by rigorous clinical studies and benefit from the full range of advanced technology available in the linear accelerators used at clinical sites. The growth margins necessary for coverage of the subclinical spread (as accounted for by the CTV) and the geometric uncertainty accommodated by the PTV are generally well established and the beam can be shaped to conform to the PTV using multileaf collimators. Preclinically these standards are far less established, not least because the technology to deliver treatments targeted to individual tumours came much more recently to preclinical sites than clinical ones, with one of the most common targeted preclinical irradiation platforms used today, the Small Animal Radiotherapy Research Platform (SARRP) being developed less than 20 years ago (Deng et al, 2007).

As noted in the 'Roadmap for Precision Preclinical X-Ray Radiation Studies', while many centres use less clinically relevant models that involve irradiating large amount of normal tissue, the technology available for preclinical research has advanced to the stage that more clinically relevant models can be applied (Verhaegen et al, 2023). This technology has been utilized at several sites, including the brain, where there are studies comparing dose distributions between parallel opposed beams and arcs plans (Mowday et al, 2020) and the pancreas, where targeted arc therapy has been used to irradiate pancreatic tumours in KPC mice (Tesson et al, 2024).

Precise targeting of lung tumours has also been performed, with treatment plans including irradiation of a single nodule with lateral and dorsal beams using a 5x5 mm collimator (Herter-Sprie et al, 2014) and 4 field beam arrangements consisting of pairs of parallel opposed beams when treating a single implanted orthotopic tumour (Wang et al, 2023). However, while it is possible to treat lung nodules with clinically relevant radiotherapy, complications can arise due to respiratory motion, with one phantom study indicating that respiratory motion could potentially contribute to over 4mm of movement in the Z-direction (Heyden et al, 2017).

Clinically, the effect of respiratory motion can be reduced through Deep Inspiration Breath Hold techniques (Josipovic et al, 2019) or respiratory gated radiotherapy (Keall et al, 2006). This allows for smaller margins to be used around the tumour due to reduced geometric uncertainty. Preclinically, beam gating has been added to some of the commercially available preclinical irradiators, including the SARRP (Hill et al, 2017). However, as many centres do not have access to this technology, with the centre this study was performed at only installing this capability after the GEMM experiments detailed in this study had begun, the effect of respiratory motion should be carefully considered when creating treatment plans, and the margins used should ideally be verified histologically to ensure that the tumour is being irradiated.

There is also a lack of consensus in preclinical treatment verification techniques. While the American Association of Physicists in Medicine (AAPM) Task Group 61 does provide guidance on how to perform x-ray dosimetry in the energy range used preclinically (AAPM, 2001), many centres lack either the equipment or the expertise to carry out these tasks independently (Biglin et al, 2019). As a result, it was necessary to decide on our own parameters for accuracy, using recent audits performed by the National Physics Laboratory (Patallo, 2020) and the University of Manchester (Biglin et al, 2022) for guidance.

1.5.5 Achieving clinically relevant preclinical plans

As discussed in the previous section, there is no consensus between centres on what planning techniques to use preclinically. As a result, there is significant heterogeneity in the beam arrangements used at different sites. Examples of three different types of treatment plan can be found in Figure 9.

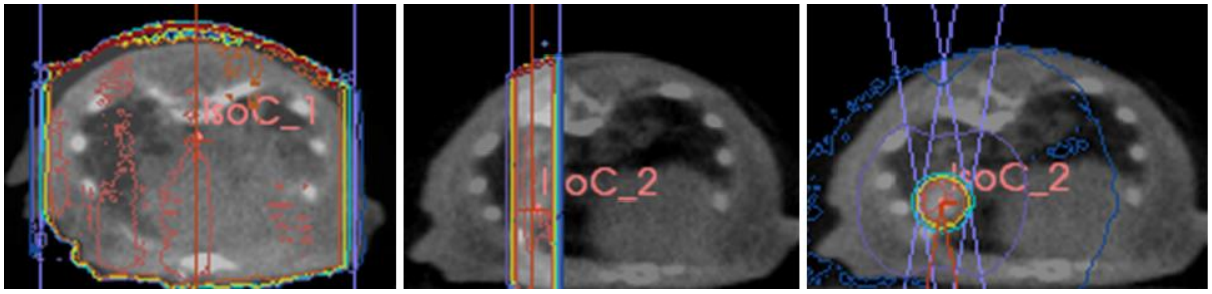

Figure 9. Three treatment plans for a KP GEMM tumour; from left, a whole lung ant-post parallel opposed beam plan (also known as an 'APPA' plan), a targeted parallel opposed beam plan and an arc.

The purpose of this figure is to show the proportion of the normal tissue that is irradiated with each plan. The whole lung plan consists of two beams shaped to the dimensions of the lung using the SARRP's variable collimator, the targeted parallel opposed beam plan uses two opposed and collimated beams to confirm to the shape of the tumour and the arc plan rotates around the mouse, creating a low dose bath in the normal tissue of the mouse and dosing the tumour at the isocentre.

Of the three plans shown, the arc spares the most normal lung tissue, and both the parallel opposed targeted beams and the arc completely spare the heart. However, respiratory motion in the lung complicates treatment planning, and using an arc instead of parallel opposed beams potentially contributes to error unless very wide margins are used. A study of respiratory motion in a murine phantom found that the tumour could be displaced as much as 1.4mm in the Y-direction during the breathing cycle (Heyden et al, 2017). As the ant-post parallel opposed beam completely removes the potential for error in the Y plane as mice were treated with these instead of arc beams.

1.6 Preclinical Mouse Models of NSCLC

1.6.1 Difference between human and mouse lungs

There are a number of noted differences between mouse and human lungs than can complicate the use of mice in preclinical studies. Key differences between mouse and human lungs can be found in Figure 10.

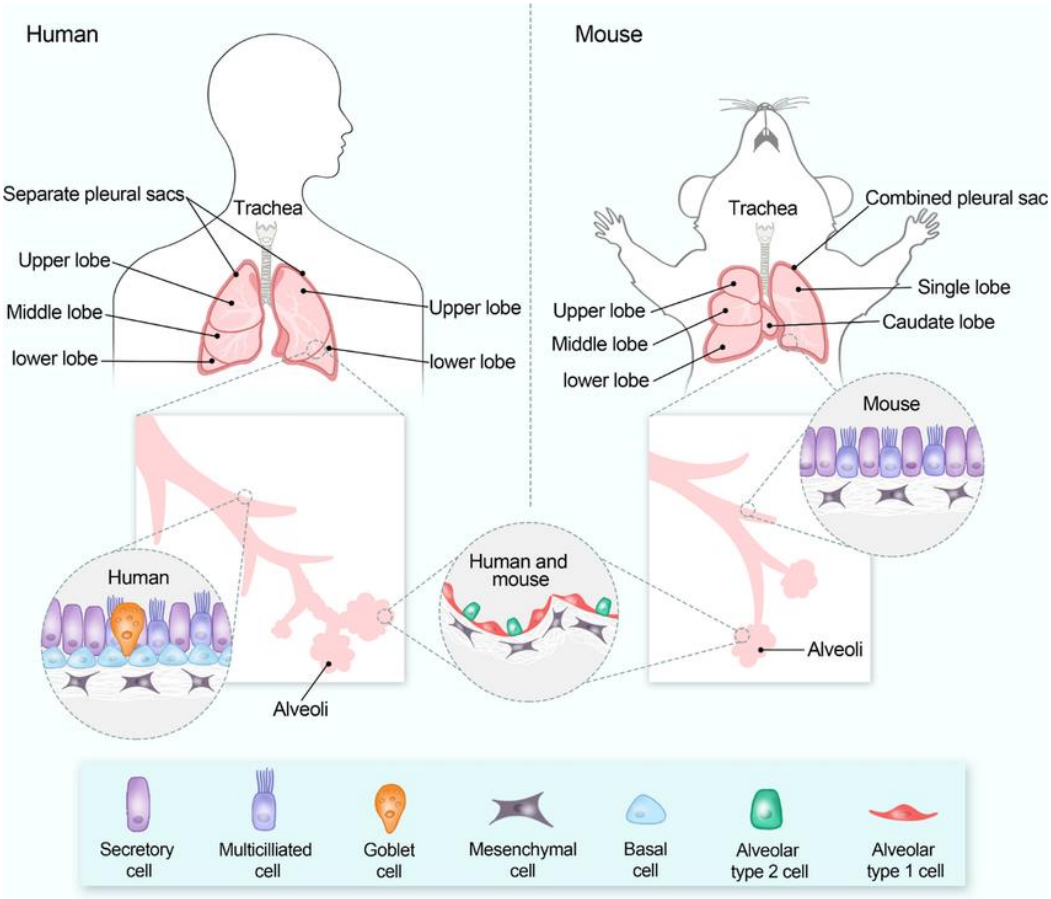

Figure 10. Key differences between the structure of mouse lungs and human lungs, reprinted from Journal of Translational Medicine, 2024, 22, article number 25, Zhang et al, Translational medicine for acute lung injury.
This diagram highlights differences in two key areas; gross and microscopic anatomy. In terms of gross anatomy, human lungs have 3 lobes on their right lung and 2 lobes on their left while mice have 5 lobes on their right lung and 1 lobe on their left, and mouse lungs are enclosed in a single pleural sac while humans have one for each lung. Microscopically, mice only have basal cells in their trachea while human lungs contain these cells in their bronchi as well and the distribution of cell types along the lungs of humans is less uniform than that of mice. Mice also have different and simpler airway branching patterns compared to humans. Goblet cells also generally only appear in mice after the airway is damaged in some way while they are common in humans (Miller & Spencer, 2017).

While the differences between human and mouse lungs should be taken into account when attempting to generalise preclinical studies results to humans,

there are still a number of advantages to using mice; they are easy to use, genetically similar to humans (Verhaegan et al, 2023) and can be used to create GEMMs which can spontaneously grow orthotopic tumours that recapitulate the tumour microenvironment (Singh et al, 2012), with GEMMs having the potential to closely mirror human tumours' molecular and histopathological characteristics (Kersten et al, 2017). As a result, despite their drawbacks they remain the most popular animal for preclinical radiotherapy research, and there are a number of murine models that can be used to explore cancer generally and NSCLC specifically.

1.6.2 Types of preclinical mouse model

Cell Line Models

Cell line models are derived from the tumours of humans or mice. When these models are derived from humans and implanted into mice they are called 'xenografts', and when they are derived from murine tumours and implanted into mice they are called 'allografts'. Cell line models can be implanted into sites other than the site of origin of the tumour, with subcutaneous flank tumours being one of the most common examples of this.

Subcutaneous tumours have a number of advantages, being easy to use, faster growing than alternative models and possibly more reproducible, with the final volume of subcutaneous tumours potentially varying less than in orthotopic models (Fernandez et al, 2023). However, they also have a number of disadvantages, as subcutaneous tumours do not have the same inflammatory responses (Tan et al., 2021) or immune microenvironment (Horton et al., 2021) that orthotopic tumours have. Subcutaneous tumours also have a greater number of functional blood vessels, which could be an issue for radiotherapy as these better perfused tumours may be more radiosensitive, making them less of an accurate model for gauging radiotherapy response (Guerin et al, 2020).

Some of the disadvantages of cell line models can be removed by implanting these tumours orthotopically. These models can be useful as they recapitulate the tumour microenvironment more faithfully than subcutaneous tumours while

allowing the creation of single tumours that can be easily targeted for normal tissue sparing, clinically relevant treatment planning (Wang et al, 2023). However, even when implanted orthotopically into immunocompetent mice these models do not recapitulate the tumour microenvironment as faithfully as GEMMs (Verhaegan et al, 2023).

GEMMs

GEMMs are mice which have been genetically altered to better model human diseases. For cancer research, they are often created through oncogene activation or inactivation of tumour suppressors (Kersten et al, 2017). When these alterations to promote tumorigenesis have been performed, tumours then grow spontaneously within the mouse (ibid). GEMMs have a number of advantages over subcutaneous models, including recapitulation of the tumour microenvironment and immunocompetence. Orthotopic implantation of xenografts or allografts can also have these advantages to an extent, but do not mirror the tumour microenvironment as closely as GEMMs (Verhaegen et al, 2023) and do not have other advantages associated with GEMMs such as the fact that they can be used to model tumour progression from its earliest stages (Hill et al, 2021). GEMM models are also particularly useful because they allow for study of specific mutations with specific characteristics. For example, in this thesis the GEMM models KP and KMyc are used, the former for its noted radioresistance (Herter-Sprie et al, 2014) and the latter Myc's apparent role in regulating fatty acid synthesis across multiple sites (Singh et al, 2020; Furuya et al, 2012; Hall et al, 2016). As a result of all these advantages, spontaneously growing tumours are considered to be better predictors of radiotherapy response than other models (Verhaegan et al, 2023).

1.7 Hypothesis

This introduction discusses how already established clinical tools like ^{11}C-acetate PET can be used as a way of monitoring the fatty acid synthesis pathway of individual tumours non-invasively, how fatty acid synthesis potentially contributes to radioresistance, and how we can use preclinical radiotherapy models and clinically relevant radiotherapy techniques to investigate radioresistance.

The experiments in this thesis aimed to develop a validated treatment method for GEMM and subcutaneous allograft tumours that also spared normal tissue in the case of the GEMMs. The effect of radiation induced lung damage in normal tissue was also considered to better understand how this could affect the experimental outcomes in the GEMM experiments, and possible early imaging biomarkers of radiation induced lung damage were evaluated.

Ultimately, it was hypothesized that baseline ^{11}C-acetate uptake would be predictive of radioresistance in the preclinical models of NSCLC selected (KP and KMyc GEMMs and KP allografts), and that it would be possible to deliver these treatments in a tissue sparing, clinically relevant manner.

2. QUALITY ASSURANCE, TREATMENT PLANNING AND DOSE VERIFICATION FOR PRECLINICAL RADIOTHERAPY TREATMENTS USING THE SARRP

2.1 Introduction

2.1.1 Background

In preclinical studies, high precision and accuracy are required to reduce experimental uncertainties and ensure high reproducibility. A consistent treatment planning method is also necessary to reduce variation between the doses the mice received both to the tumours and the OARs. In this Chapter, we aimed to establish the mechanical precision of the SARRP using a retrospective audit of quality assurance data, used data from this to inform margins for a dose volume histogram (DVH) based planning study, and then verified the chosen beam arrangement in a phantom using film and analysed the results using a method known as a gamma index analysis.

2.1.1 Objectives and Analysis

- Determine the mechanical uncertainties associated with the SARRP.

Daily QABB testing is performed on the SARRP to ensure that the treatment will fall within the manufacturer's tolerance, which is given in arbitrary units. A retrospective audit of these QA tests was performed after converting these arbitrary units to millimetres to determine the SARRP's mechanical uncertainties. These data are presented in the form of a scatter plot. A scatter plot was used as it would clearly visually represent the precision of the SARRP and standard deviations were calculated to assess the variance.

- Assess the degree to which using targeted parallel opposed beams and whole lung APPA plans instead of the more clinically relevant arc plans affects dose to the OARs.

The CT scans from 8 GEMM mice with imageable tumours were used as the basis for a treatment planning study that compared whole lung irradiation, targeted parallel opposed beams and arc plans. As it was decided that arc plans would not be used to reduce uncertainty due to respiratory motion, the purpose of this was to establish whether treatment with the less clinically relevant parallel opposed beam arrangement would negatively impact tumour or OAR coverage. DVHs will be used to compare doses between different treatment planning methods for the tumours and the OARs as these are commonly used clinically and in similar treatment planning studies.

- Validate the SARRP's capacity to deliver the planned treatment.

For treatment verification, a phantom film study was performed, and gamma index analyses were used to determine the difference between the planned dose and the dose delivered to the film. A graph showing gamma passing rates for distances to agreement of 1 and 2mm is used to present these data. This treatment verification method was used as film studies and gamma index analyses are well established for use preclinically and clinically and more complex technology such as using a multidetector array was not an option.

2.2 Materials and Methods

2.2.1 Imaging Quality Assurance using the Ball Bearing Phantom

The Quality Assurance Ball Bearing (QABB) phantom produced by Xstrahl consists of a single ball bearing embedded in plastic which is used for daily alignment and QA, as shown in Figure 11.

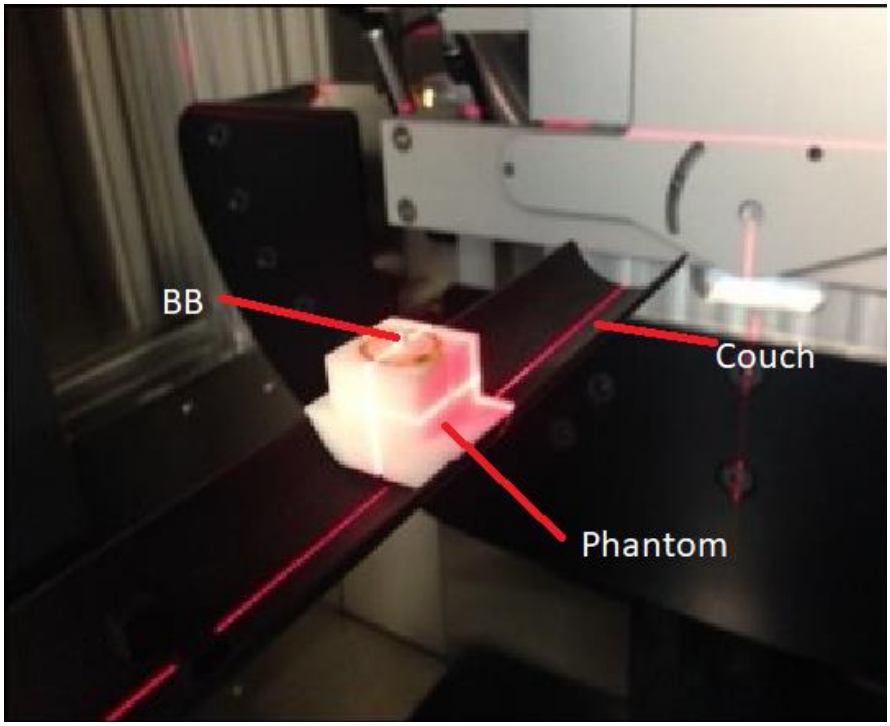

Figure 11. QABB phantom placed on couch for daily QA.

The QABB phantom is shown on the couch aligned with the SARRP's internal lasers prior to CT scanning. These CT scans are performed to ensure that the treatment isocentre, CT and couch are correctly aligned (Xstrahl, 2018).

The QABB phantom was placed on the mouse bed and the ball bearing aligned with the positioning lasers. The SARRP's onboard cone beam CT was used to acquire images, with 360 projections at 60kVp and 0.8mA using the fine focal spot (1mm) being taken. The Feldkamp, Davis, and Kress CBCT algorithm was used for reconstruction of CT images (Feldkamp, Davis & Kress, 1984). Murislice was used to identify the centre of the ball bearing, and the positioning of the treatment bed is adjusted so the imaging and treatment isocentre should be shifted to these co-ordinates. A 3x3 collimator is affixed to the X-ray tube and a planar image of the phantom is acquired at the same settings as the CT.

This raw image file was exported to ImageJ, which is an open-source image analysis program developed by the Laboratory for Optical and Computational Instrumentation National Institutes of Health (Rueden et al, 2017) The thresholding tool in ImageJ was used to adjust the levels until the ball bearing was clearly visible. For consistency the same thresholding settings were originally used across all the images. It became apparent, however, that this was unsuitable as the installation of an on-treatment dose monitor affected beam

quality. Thus, two sets of threshold settings were used; before installation of the dose monitor, a minimum threshold value of 0 and a maximum threshold value of 10280 were used, and after installation of the dose monitor a minimum threshold value of 0 and a maximum threshold value of 5140 were used. A region of interest was then drawn around the ball bearing, which was used to define its centre and compared to the manufacturer co-ordinates to ensure the isocentre was within tolerance, as shown in Figure 12.

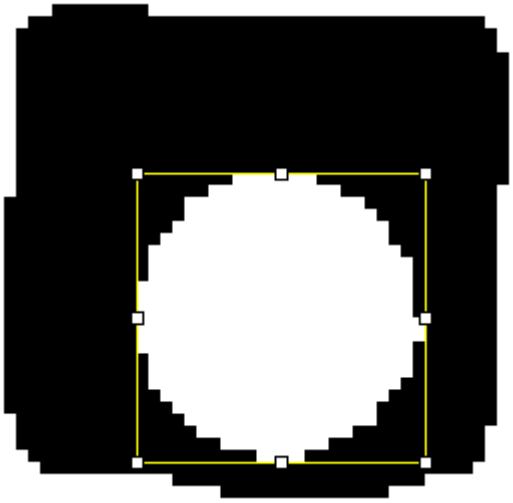

Figure 12. Example of the ball bearing from the Quality Assurance Ball Bearing used for daily QA in the SARRP outlined in ImageJ

This image was taken using the SARRP's onboard X-ray tube (60keV and 0.13mA settings). To maintain consistency in dealing with the noise on the outer edge of the ball bearing anything any single pixel noise was excluded but anything with multiple pixels was included.

While this shows that the displacement meets manufacturer standards, knowing the distance between the planned and imaging/treatment isocentres is necessary for understanding how this disparity should be accounted for in the margin applied around the Genetically Engineered Mouse Models. To convert these co-ordinates into millimetres a correction factor was calculated and applied in ImageJ. This correction value was calculated using the known length of whole phantom and verified using the known length of the collimator in the planar images. In total 247 daily QA results were included, and displacement from the isocentre was plotted for each value.

2.2.2 Treatment Planning

Mice

Kras$^{G12D/+}$ p53$^{-/-}$ (KP) genetically engineered mice (n = 8) were induced via AdenoCre inhalation. These mice were induced at low titre (5 x 10^4 pfu/ml) to ensure large, isolated tumours suitable for individual targeting. Using a lower titre means that fewer tumours grow, often resulting in the tumours being spaced further apart, and allowing individual tumours to grow larger without connecting. The reason that KP mice specifically were used is that these mice were originally intended to be included in the ^{11}C-acetate PET experiment described in Chapter 6, but due to COVID they had to be culled to reduce stock and the final 8 scans from this cohort were then used in this study. KP mice also work well for this study as their tumours are sufficiently far apart to allow for individual targeting.

Cone Beam CT Protocol

Mice were monitored for clinical signs that were listed in the SOP for this model (weight loss, hunching and respiratory distress) twice a week and CT scanned once a month to monitor tumour growth. CT scans of the mice with two or more tumours with diameters greater than 1 mm were selected for this study. The SARRP's onboard cone beam CT was used to acquire images, with 1440 projections at 60 kVp and 0.8 mA using the fine focal spot (1 mm) being taken. 8 scans were used because this was the total size of the cohort. The final scan was used for each mouse.

Treatment Planning

Three different plans were prepared for each of the eight CT scans to look at the dose volume relationships in the tumour, the heart and the liver; arc beams, parallel opposed beams targeting specific tumours and whole lung irradiation plans. The comparison between the arc beams and the parallel opposed beams was included because while arc beams are more clinically relevant and potentially offer the most favourable OAR doses, there are greater uncertainties

regarding respiratory motion compared to targeted parallel opposed beams as using the latter means that motion in one plane can be discounted. To reduce the potential for error we selected parallel opposed beams, and this treatment planning study can determine how use of this less clinically relevant technique might affect the dose to the OARs. As the *LSL-Kras$^{G12D/+}$ Rosa26-LSL-Myc* (KMyc) mice required whole lung irradiation as their tumours did not grow sufficiently far apart for individual targeting whole lung plans were also included in the analysis.

Plans were created in Muriplan (a 3D Slicer based treatment planning system developed by Xstrahl in collaboration with John Hopkins University) which uses a superposition-convolution algorithm for dose calculations. OARs and tumours were also outlined in Muriplan through visual assessment. Dose distributions were optimised by adjusting beam arrangements after dose calculations, visually assessing the changes and adjusting. The isodose lines on the plans were used to optimise the plans, particularly the 95% isodose line.

Acceptance criteria was D95 > 95% for the tumour and minimised dose to the surrounding tissue. Dose volume histograms (DVHs) which facilitate quantitative analyses of treatment plans were calculated and exported for analysis. The DVHs of each mouse were combined to create the mean DVHs for each plan type and for each region of interest in GraphPad Prism. It was not possible to assess contralateral lung as tumours appeared in both lungs and it was also not possible to outline the oesophagus as the CT did not show sufficient detail to delineate it, although these would normally be considered OARs clinically.

Figure 13 summarises the experimental workflow.

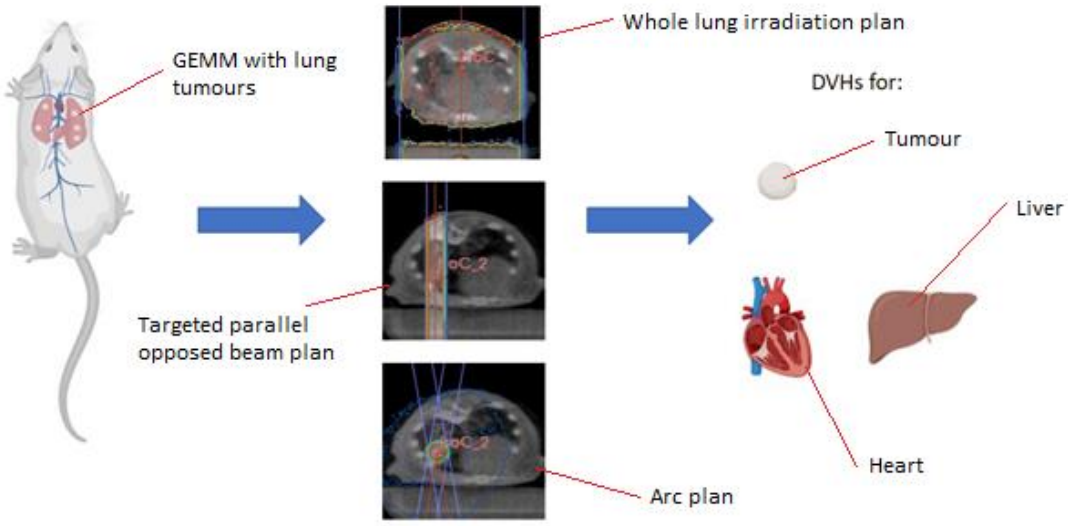

Figure 13. Experimental Design for Treatment Planning Study.

Illustration of the treatment planning study involving mice subjected to whole-lung irradiation using targeted parallel opposed beams and arcs. Mice were CT scanned, three treatment plans were drawn up for each plan and DVHs created for the tumour, liver and heart. The orange lines on the scans represent the 95% isodose line.

2.2.3 Treatment Verification of Parallel Opposed Beam Arrangement

Having found that the tumour coverage was acceptable using parallel opposed beams and that the heart dose was comparable to the arc it was decided that the method used would be the parallel opposed beam plan despite the increased liver dose to reduce the effect of tumour movement due to respiratory motion. The next step was to perform dosimetry to ensure that the doses calculated in the treatment planning system matched those delivered by the SARRP.

First the CT scans of the eight *Kras*$^{G12D/+}$ *p53*$^{-/-}$ (KP) genetically engineered mice induced via AdenoCre inhalation at a titre of 5 x 10^4 PFU/ml were assessed to determine what collimator would provide acceptable coverage of the tumours, and by testing different collimators in Muriplan and checking that they would leave a margin of at least 1mm around the tumour it was found that a collimator size of 5 x 5 mm would adequately cover these tumours.

Gamma index analyses were performed to verify the treatment plans. This analysis is a way to quantitively analyse the similarity between two dose

distributions by combining the difference in dose between the two distributions (measured in %) with the 'distance to agreement', or the distance between a specified pixel in the reference distribution and a pixel with a matching dose in the evaluation distribution (mm), and are thus measured in units of %/mm. A PTW UNIDOS E Farmer ionisation chamber was used as the absolute dosimeter to calibrate the GafChromic EBT3 film we used to assess the dose distribution. EBT3 film was used as its high energy independence over 100 keV has been verified (Ashland, n.d), making it suitable for the SARRP's 220 keV treatment beam energy, and film from the same batch was used to reduce the risk of interfilm variation. The solid water phantom for the ionisation chamber and film provided in the Xstrahl Physics QA kit were used for the film calibrations.

Calibrations were carried out in accordance with the AAPM TG61 guidelines for 40 - 300 kV x-ray beam dosimetry (Ma et al, 2001) under the conditions outlined in Table 1.

Source to Phantom Distance (cm)	Ionisation chamber depth (cm)	Field size (cm)	Copper filter thickness (mm)	Voltage (keV)	Current (mA)
33	2	17 x 17	0.15	220	13

Table 1: Table showing the setup of the ionisation chamber during the first stage of calibration.

Temperature and pressure corrections were applied. Five readings were taken at both -300 keV and -200 keV to account for ions lost due to 'self' or 'volume' recombination, five at 300 keV to account for the polarity effect and ramp-up was characterised by taking measurements at 6, 12, 18, 24, 30 and 60 seconds. These readings were adjusted in accordance with the absorbed dose calculation discussed in the Introduction to give the dose rate of the machine.

This dose rate was used to expose the 5 x 5 cm squares of EBT3 GafChromic film (Ashland LLC, Bridgewater, NJ) to 8 known doses up to 120% of the maximum prescription dose used in treatment planning in accordance with the instructions

given by the analysis software Radiochromic.com. Radiochromic is a Spanish cloud-based radiotherapy dosimetry system that uses the creators' own Multigaussian method of multichannel radiation dosimetry to create a calibration to allowing the creation of a calibration curve that can be used to calculate the dose distribution of the treatment film (Méndez et al, 2018).

An ant-post parallel plan created for a single tumour in a GEMM was used as the basis for the treatment verification. During verification, the beam arrangement used for the mouse was delivered to a film in the water equivalent phantom provided by Xstrahl under the same conditions used for calibration (see Table 1). A scalar dose volume for the irradiated plane is extracted from the created treatment plan for use in the gamma index analysis later. After allowing 48 hours to post exposure so the optical density of the film could settle, the 48-bit RGB scans were acquired in an Epson Perfection V850 scanner in transmission mode for both the calibration films and the treatment film.

These scans were uploaded to the analysis software Radiochromic.com, and a calibration curve was created using Radiochromic.com's Multigaussian model (Méndez, Esctuta and Casar, 2021). This calibration curve was applied to the scan of the treatment film in order to create a scalar dose volume which could be compared to the dose distribution calculated by the treatment planning system.

The settings used for the calibration and gamma index analysis where a threshold dose of 10% of Dmax, normalisation of Global (Dmax) and no lateral corrections were applied.

While 95% is the usual clinical standard for gamma passing rate (GPR), a more lenient approach was taken in this study as there are additional complications that arise from dosimetry for low energy radiotherapy. This is because at keV energies the photoelectric effect is more prominent than it is at typical clinical EBRT MeV energies (although Compton scattering is still the most prominent). As the photoelectric effect is highly Z dependent while Compton scattering is almost entirely dependent on the electron density treatment planning calculations are less accurate at keV range (Verhaegan et al, 2014). Acceptance criteria of 3%/2 mm, 3%/1 mm, 2%/2 mm, 2%/1 mm, 1.5%/2 mm and 1.5%/1 mm

were applied and the GPR plotted for each criterion. When a dose tolerance of 3% was not sufficient to ensure a GPR > 90%% the dose tolerance was increased in 2% increments up to 10% to assess whether raising the dose tolerance could result in a GPR of 90%.

2.3 Results

2.3.1 Retrospective audit of quality assurance data

A retrospective dosimetry audit was performed to assess the displacement of the QABB from the treatment isocentre in the x and y planes. The data presented in Figure 14 show that most values were within 0.5 mm of the isocentre, with only 4 out of 247 values exceeding this threshold in the X direction and none in the Y direction. The mean displacement and standard deviation were 0.25 mm and 0.13 mm in the X direction, and 0.23 mm and 0.06 mm in the Y direction, respectively. These results demonstrate that the SARRP system achieves sub-0.5 mm precision, accounting for mechanical and user errors in defining the isocentre in Murislice. The discrete distribution is due to the resolution of the image.

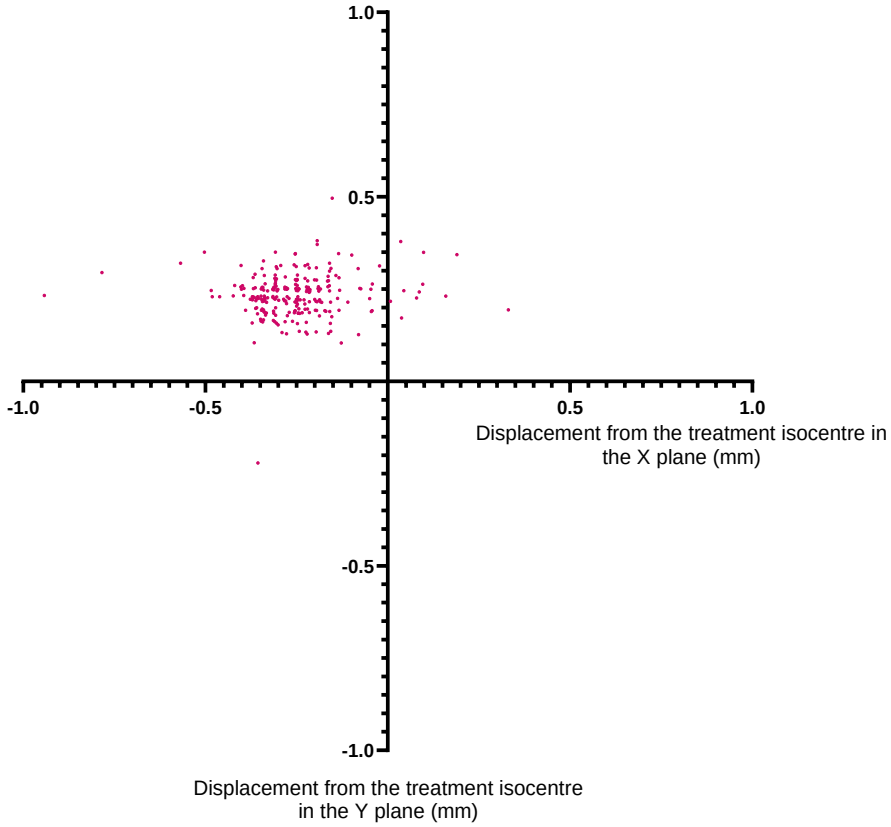

Figure 14. Displacement of the QABB from the treatment isocentre in the x and y planes. (N=247)

The graph illustrates the displacement of the QABB from the treatment isocentre in the X and Y planes. Most values were within 0.5 mm of the isocentre, with only 4 out of 247 values exceeding this threshold in the X direction and none in the Y direction. The mean displacement and standard deviation were 0.25 mm and 0.13 mm in the X direction, and 0.23 mm and 0.06 mm in the Y direction, respectively.

2.3.2 Treatment Planning

A treatment planning study that compared whole lung irradiation, targeted parallel opposed beams and arc plans was performed. DVHs were used to compare doses between different treatment planning methods for OARs, specifically the heart and the liver. The data presented in Figure 15 compare DVHs for the heart and the liver for the averaged arc plans, and show that the V50 for Heart in the Arc plan is 24.5% and the V50 for the Liver is 5.3%

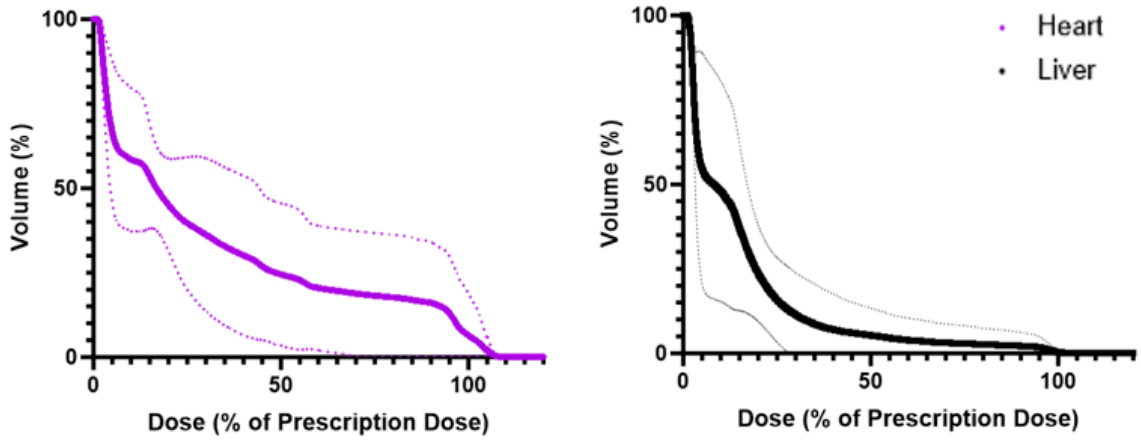

Figure 15. Mean Dose Volume Histograms (DVHs) for the OARs for the Arc plan (n. Plan=8)

These graph shows that the V50 for Heart in the Arc plan is 24.5% and the V50 for the Liver is 5.3%. The heart is shown in purple and the liver in black. The dotted lines correspond to the standard deviations for the averaged plans.

Figure 16 shows DVHs for the heart and the liver for the averaged parallel opposed beam plans. The V50 for the heart in the Parallel Opposed beam arrangement is 27% and the V50 for the liver is 31.5%. This means that the heart dose is comparable, but the liver dose is higher in the parallel opposed plan than the arc. The dotted lines correspond to the standard deviations for the averaged plans.

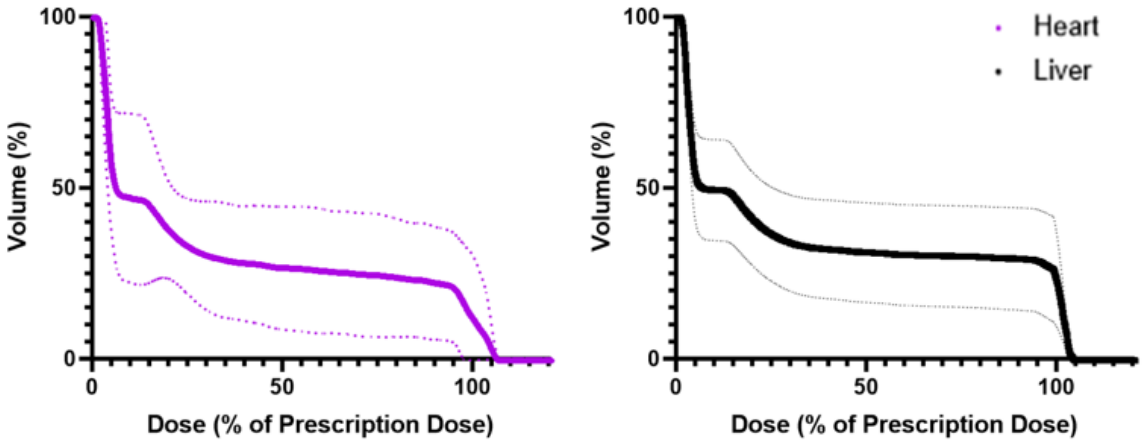

Figure 16. Mean Dose Volume Histograms (DVHs) for the OARs for the Parallel Opposed plan (n. Plan=8)

This graph shows that the V50 for the heart in the Parallel Opposed beam arrangement is 27% and the V50 for the liver is 31.5%. The heart is shown in purple and the liver in black.

Figure 17 shows DVHs for the heart and the liver for the averaged whole lung irradiated plans and show that the V50 for the heart in the Whole Lung beam arrangement is 99.7% and the V50 for the liver is 72%. This means that a higher percentage of the heart and liver are being irradiated by 50% of the prescription dose than in both the Arc and Parallel Opposed beam plans.

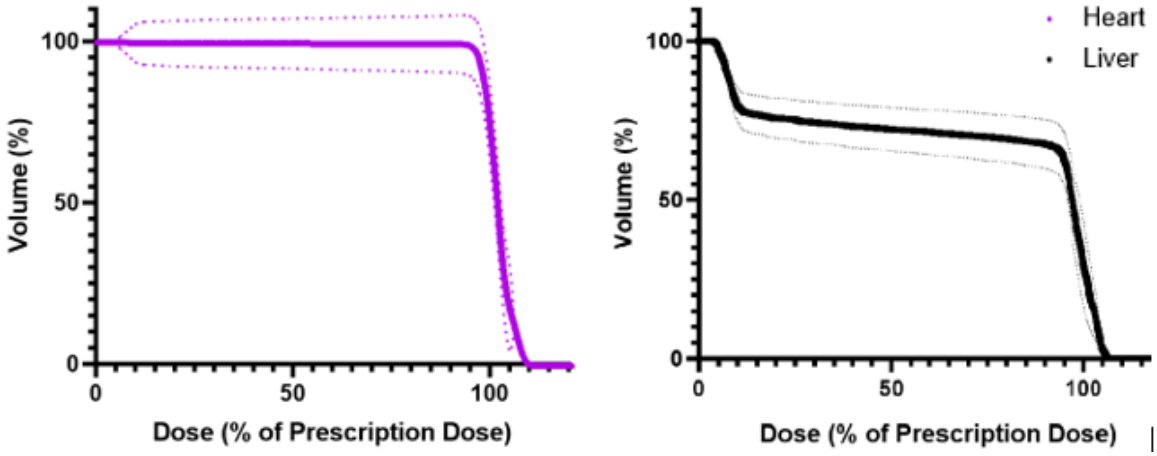

Figure 17. Mean Dose Volume Histograms (DVHs) for the OARs for the Whole Lung plan (n. Plan=8)

This graph shows that the V50 for the heart in the Whole Lung beam arrangement is 99.7% and the V50 for the liver is 72%. The heart is shown in purple and the liver in black. The dotted lines correspond to the standard deviations for the averaged plans.

2.3.3 Treatment Verification of Parallel Opposed Beam Arrangement

A phantom film study was performed, and gamma index analyses were used to determine the difference between the planned dose and the dose delivered to the film. Figure 18 shows gamma passing rates for distances to agreement (DTA) of 1 and 2mm. Requiring a Dose Tolerance of 10% at 1mm DTA and 9% at 2mm to reach a GPR of >90% indicated that there may be an issue with the output. This error was caused by values in the TPS not being updated when the software was upgraded, meaning that calibration should be performed after TPS upgrades in the future to prevent the error from reoccurring. Xstrahl were consulted and a fault was confirmed and fixed.

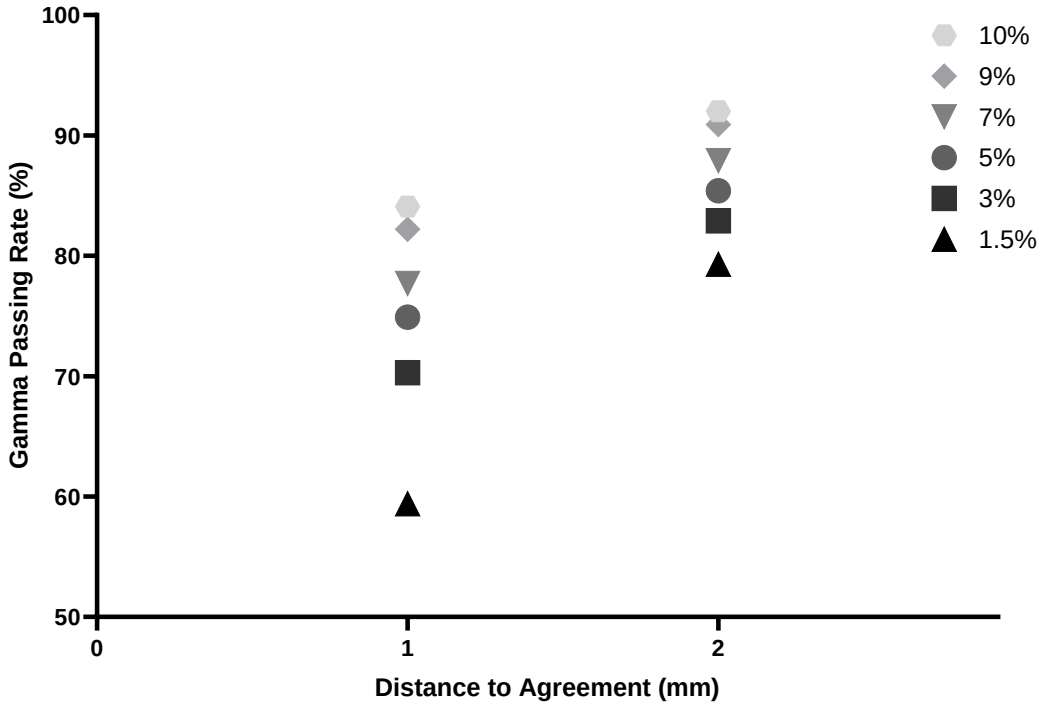

Figure 18. Figure showing results of first gamma index analysis. Each point represents different acceptance criteria applied to the same pair of calibrated film and scalar dose volume.

A Dose Tolerance of 10% at 1mm DTA and 9% at 2mm was required to reach a GPR of >90%.

Another phantom film study was performed after the correction of the issue indicated in Figure 18, and gamma index analyses were used to determine the difference between the planned dose and the dose delivered to the film. Figure 19 shows that gamma passing rates for acceptance criteria of 1.5-3%/1-2mm are >90%. Each point represents different acceptance criteria applied to the same pair of calibrated film and scalar dose volume. Figure 19 shows that the gamma passing rate varies from 98.3% for the loosest criteria (3%/3 mm) to 90.1% for the strictest (1.5%/1 mm).

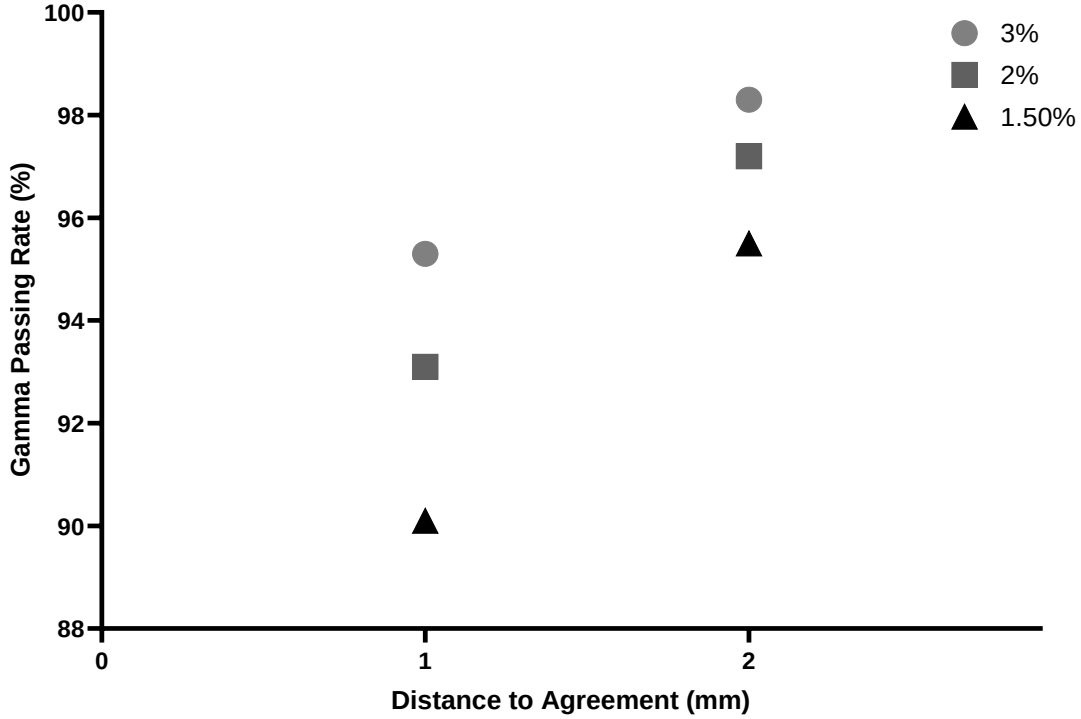

Figure 19. Graph showing the gamma passing rates for the selected criteria after issue with treatment planning system was corrected.

Gamma Passing Rates for Acceptance Criteria of 1.5-3%/1-2mm are >90%. Each point represents different acceptance criteria applied to the same pair of calibrated film and scalar dose volume.

2.4 Discussion

2.4.1 Summary of Objectives

- Determine the mechanical uncertainties associated with the SARRP.

A retrospective audit of the QABB test indicated that the SARRP is capable of sub 0.5 mm precision (see Figure 14).

- Assess the degree to which using targeted parallel opposed beams and whole lung APPA plans instead of the more clinically relevant arc plans affects dose to the OARs.

Figures 15, 16 and 17 show that targeted parallel opposed beam plan provides comparable heart sparing to the arc plans but delivers additional dose to the liver.

- Validate the SARRP's capacity to deliver the planned treatment.

A gamma index analysis performed after the correction of an error detected by the initial tests (Figure 18) showed that the SARRP can deliver treatment within the planned parameters (Figure 19).

2.4.2 Discussion

Quality Assurance Ball Bearing audit

Overall, the retrospective audit of the QA showed encouraging results and indicated that the SARRP is capable of sub-0.5 mm precision. However, there are a few things that need to be addressed in the findings. The first is that there is clearly a bias in the system, with results clustering in the upper left quadrant in a pattern that is highly precise but slightly inaccurate. This is likely because the commissioning and QA checks performed by the manufacturer focus on meeting a certain threshold of accuracy rather than routing out small but noticeable systematic errors. If this was addressed, then given the low standard deviations in both the X and Y directions (0.06 mm and 0.13 mm respectively) then sub-0.25 mm precision could be achieved.

Also, there are five results of the 247 that extend beyond 0.5 mm displacement from the treatment isocentre, although all are within 1mm of it. While this is a small proportion of the measurements, even one tumour being only partially irradiated could affect the results of a study, especially in small studies like the GEMM experiments in my thesis. It is likely that these results would have been queried on the day and either a set up error identified, or the experiments postponed if the fault was mechanical, but as I was not present during any of these five treatments to confirm that the result was out of tolerance, I cannot confirm that.

Treatment Planning Study

The biggest difference between the arc and parallel opposed beam plans is the increased dose to the liver that the latter delivers. Liver irradiation is associated with Radiation Induced Liver Disease (RILD), which causes clinical signs such as fatigue, pain, abdominal swelling and ascites (Benson et al, 2016). While it is a common complication of liver irradiation and often acts as a limiting factor preventing dose escalation for liver and other abdominal tumours (ibid), the conformal nature of lung radiotherapy planning in the clinic means that liver irradiation is rarely a concern, especially given that Stereotactic Ablative Body Radiotherapy (SABR) PTV margins are as low as 5mm (Jasper et al, 2021). This means that the use of not only the whole lung APPA beam arrangement but also the targeted parallel opposed beam plans. This is especially concerning as C57BL/6 mice can manifest many of the symptoms of RILD and are even used to model the disease (Kim & Jung, 2017), meaning that in a longer-term study this would be likely to affect the outcomes of the mice. While this would have a limited effect in a shorter-term study such as those carried out as part of this series of experiments, it raises concerns for how best to balance clinical relevance with the practical dosimetric concerns such as the potential for underdosing the tumour (Heyden et al, 2017) in longer studies.

Gamma Index Analysis

The most notable thing about this section is the less the success of the second set of analyses and more the extent of the error in the first. Upon recognising the error in readings, we contacted Xstrahl who after investigating informed us

that the commissioning data for the version of Muriplan that we were using had not been updated to accommodate changes to the SARRP and that mice treated on the machine had been being underdosed for several months (a ratio of the planned dose in the inaccurate version of Muriplan to the updated version of Muriplan indicated that mice were getting ~92% of the dose they had been prescribed).

This error was impossible to detect via the simple dose rate verification that most centres carry out routinely as it was built into the treatment planning system which is not used during such checks. This means that without performing treatment verification the error would have continued unnoticed until the new version of Muriplan was fully usable and those who had used the SARRP during this period would have been unable to adapt their experimental plans to accommodate the error. This emphasizes how fundamental dosimetry is to any radiotherapy project.

The gamma index analysis carried out after the adjustment of the treatment planning system shows how accurate the SARRP is when functioning correctly, with a gamma passing rate of >90% for the 1.5%/1mm criterion, exceeding the standards I had set for success. A widely accepted clinical standard is a GPR >95% 3%/3mm (Das et al, 2022), although many centres internally aim for 2%/2mm. However, as 1mm is a much larger proportion of the treatment volume for a mouse tumour than it is for a human tumour it seemed appropriate to use 1mm as the DTA parameter.

The results of this analysis are also broadly in line with a treatment verification study carried out in the SARRP attached to Glasgow Veterinary School which used the same phantoms and absolute dosimeter that this experiment did, with Rutherford et al's GPR for a single beam (closest to our ant post parallel opposed beam arrangement) being over 95% with acceptance criteria of 2%/1.5 mm (Rutherford et al, 2019). This increases confidence that the analysis is valid and the equipment working appropriately. A lower standard for a 'passing' GPR was used than in many clinical studies (>90% rather than >95%); this is because of noted inaccuracies relative to clinical treatment planning systems due to difficulties with the calculation of the dose distribution at kilovoltage ranges and in small beam apertures (Verhaegen et al, 2014).

2.4.3 Limitations

The weakest point in this study is the fact that the excessive dose to the liver makes the beam arrangement that was used less clinically relevant than the arc beam. However, adopting the arc beam would result in either an increased chance of underdosing the tumour or the need to apply wide enough margins that the arc for one tumour would risk overlapping with the arc for others nearby, potentially affecting any mice that were not induced at the lowest titre or for models like KMyc that grow tumours which cluster together.

One option to limit the effect of the respiratory motion would be to only analyse tumours that are sufficiently far away from the diaphragm. This is because superiorly located lung tumours experienced far less movement in the Z-direction than inferiorly located tumours do (Heyden et al, 2017). To do this it would be necessary to fully characterise the movement of the tumours within the lungs, something which could be achieved using dynamic MRI imaging, which has already been used to track tumour motion in human lungs (Kauczor & Plathow, 2006), or using a Compact Light Source (Gradl et al, 2018).

Tracking the motion of tumours in different regions would be especially useful for the KMyc tumours because these are smaller and closer together; the murine phantom study referenced above focused exclusively on large, solitary tumours that resemble the low titre KP tumours (Heyden et al, 2017), which may have different ranges of motion in comparison to smaller, closer together tumours like the KMycs as the differing tumours burdens could affect how the mouse breathes.

Regarding the treatment verification, the best way to make this study more robust would be to use multiple different dosimetry programmes to analyse the data. Currently the dosimetry tool used at our centre is the cloud-based software radiochromic.com, which uses a different method to convert the film to a scalar dose volume than the most popular dosimetry product on the market, FilmQA Pro (Méndez et al, 2018).

3. IN VIVO DOSE VERIFICATION FOR SUBCUTANEOUS ALLOGRAFTS, GENETICALLY ENGINEERED MOUSE MODELS AND NORMAL TISSUE

3.1 Introduction

3.1.1 Background

While the SARRP is mechanically capable of delivering very precise doses of radiation, other factors influence the dose delivered to the targeted area. Mechanical accuracy does not account for factors such as mouse movement and, for GEMM models, respiratory motion; to assess this verification that the treatment has been delivered as planned to the mouse needs to be performed. This chapter will discuss a series of experiments intended to demonstrate that the planned treatments are being delivered to the tumours and that the proportion of normal tissue being irradiated is the same as that indicated on the Treatment Planning System (TPS) using TPS calculated dose distributions and histological markers of radiation-induced DNA damage (Phospho-histone H2A histone family member X, or γH2AX, staining).

3.1.2 Biological Dosimetry

γH2AX staining is a common technique tracking Double Stranded Break (DSB) formation and repair in cells exposed to ionising radiation. The phosphorylation of the histone variant H2AX on Serine-139 resulting in the formation of γH2AX is an early cellular response to DNA DSBs, which is useful for assessing response to radiation exposure (Mah et al, 2010).

As γH2AX fluorescence intensity and foci increase with radiation dose it has been utilized to determine not only if a target has been irradiated, but also to evaluate the delivered dose. This is done by creating calibration curves of γH2AX fluorescence intensity against the radiation dose for tissues irradiated with

known radiation doses. Biological dosimetry using γH2AX is most commonly performed on blood samples after radiological emergencies (Chaurasia et al, 2021), and as γH2AX fluorescence intensity linearly increases with dose even with partial body exposures (Horn et al, 2011) it can also be used to determine the dose received in targeted therapies. Stained sections of organs have also been used after $^{111}InCl_3$ administration to study dose-response relationships in animal and human tissue (Stenvall et al, 2020).

The limitations of these more precise forms of biological dosimetry are that tumour heterogeneity can result in difficulties in applying the calibration curves as there can be inter- and intratumour variation in DNA repair proficiency. As a result of this and the low sample sizes in the studies in this section the γH2AX staining in these experiments will only be used to determine whether the tumour has been irradiated or not, not to determine the dose distribution.

3.1.3 Objectives and Analysis

- Ensure that the selected margins adequately cover the subcutaneous tumours.

For the KP allografts there are two treatment groups: the control group and the irradiated group. The percentage of γH2AX positive nuclei in each subcutaneous tumour will be plotted, with the control and treatment groups separated. All positive nuclei (strongly, moderately and weakly positive) were considered together for analysis as the purpose of this experiment was to assess dose coverage, not the relative radiosensitivity of each region. A Mann-Whitney test will be performed to determine whether there is a statistically significant difference between the two groups. A Mann-Whitney test was chosen because it is suitable for small sample sizes and does not assume a normal distribution.

- Ensure that margins cover the GEMM tumours.

For the GEMMs one tumour was treated in each mouse, with the rest being unirradiated (except for one case where an additional tumour was partially irradiated due to proximity). Each of the three mice in the cohort will be plotted seperately, with the irradiated, partially irradiated and unirradiated tumours

being represented by different symbols. All positive nuclei (strongly, moderately and weakly positive) were considered together for analysis as the purpose of this experiment was to assess dose coverage, not the relative radiosensitivity of each region. A Mann-Whitney test will be performed to determine whether there is a difference between the percentage of γH2AX positive nuclei in the treated tumours and the unirradiated tumours. A Mann-Whitney test was chosen because it is suitable for small sample sizes and does not assume a normal distribution.

- Check that the dose delivered to the OARs matches that calculated in the treatment planning system.

Uninduced mice were irradiated under anaesthetic (isoflurane in 95% oxygen) with different parallel opposed beam angles and aperture sizes to ensure different dose coverages to OARs that would be relevant for the GEMM experiments, the heart and the liver. V95, extracted from the DVH for each of the OARs, was used to measure heart and liver coverage. The percentage of γH2AX positive nuclei indicates the proportion of the heart and liver irradiated. A simple linear regression will be performed to assess whether there is a correlation between the treatment planning system's calculated dose distribution and the actual dose received by the heart.

3.2 Materials and Methods

3.2.1 Subcutaneous Allografts

Three cell lines from lung-derived $Kras^{G12D/+}$ $p53^{-/-}$ (KP) tumour were selected to correspond with the three cell lines used in the ^{11}C-acetate PET experiment. In vitro cell profiling performed previously by members of the laboratory group measuring ^{14}C-acetate uptake informed the decision regarding what cell lines to choose (Dzien, Bielik and Lewis, 2017; 2018a; 2018b). These experiments showed that T13, 19b and T25 represented the full range of acetate metabolism available in our cell lines; T13 had the highest normalised ^{14}C-acetate uptake across multiple experiments while T25 had the lowest, with T19b falling between the two (ibid). These cell lines were selected with the expectation that the range of acetate avidities observed in vitro would translate to a wide range of acetate avidities in our subcutaneous tumours. Additionally, all the cell lines selected were from different tumours in the same mouse with the intention of reducing non-metabolic variation between the tumours.

3.2.2 Cell culture

These cell lines (T13, T25 and T19b) were cultured in basic DMEM supplemented with 10% FBS and 8 mM of glutamine. When cells were 80% confluent, they were trypsinised with 1% trypsin to a single cell suspension. 2 x 10^6 cells were resuspended into 100ul of 50% sterile PBS and 50% Matrigel and sent to be implanted. The day before the implantation cells were tested for mycoplasma.

3.2.3 Implantation

Cells were transported to the implantation room on dry ice and then inverted a minimum of 10 times to ensure that they were sufficiently mixed prior to injection. A 25 G, 16 mm needle that had been refrigerated to prevent to solidification of the Matrigel was used to inject the cells. The mice were then scruffed using the thumb and forefinger to expose the skin on the flank and injected, with care taken to ensure that the syringe was inserted parallel to the body to avoid damaging any internal organs. Skin was pressed after removal of the needle to ensure that the injection site was sealed, and the animals were

returned to their cages and monitored by visual inspection to ensure no bleeding or signs of discomfort.

3.2.4 Genetically Engineered Mouse Models

Mice were induced between 8 and 15 weeks using AdenoCre inhalation after being anesthetized with isoflurane in oxygen (maintenance 1.5–2.0% v/v, induction 4-5% v/v). These mice were induced at low titre (5 x 10^4PFU/ml) to ensure large, isolated tumours suitable for individual targeting. This experiment was run alongside the ^{11}C-acetate PET studies detailed in Chapter 6 and provided an alternative pipeline for mice that developed tumours but had clinical signs that prevented their progression onto the PET study. Mice were monitored twice weekly for the following clinical signs: weight loss, hunching and respiratory distress (especially when scruffed).

Mice that had tumours larger than 1 mm in diameter and had lost >10% of their body weight prior to PET scanning, disqualifying them from the PET GEMM experiment, while not experiencing respiratory distress that would result in unnecessary suffering if they were to undergo further procedures were chosen for the experiment. As in the PET experiment, tumours that were pressed against the rib cage or diaphragm to the extent that differentiating them from the surrounding tissue became difficult were excluded.

Originally, a larger cohort was planned for this experiment, distinct from the cohort used for the PET mice studies. However, due to COVID-19, many of the mice intended for the initial experiments in this research had to be culled. Consequently, the sample size is smaller than initially intended. Therefore, the data produced should be considered to provide preliminary or proof-of-concept results rather than definitive conclusions. In total three mice met this selection criteria.

One tumour in each mouse was irradiated with 16.5 Gy/1#. A parallel opposed beam arrangement with a margin of at least 1 mm around the tumour was used in accordance with the findings in Chapter 2. In two of the mice, it was possible to irradiate a single tumour without irradiating the others. However, in the third partially dosing a second tumour was unavoidable due to its proximity to the target tumour. Mice were culled 30 minutes after irradiation using a schedule 1

method (CO_2 inhalation), lungs were extracted, put into labelled cassettes and so the orientation of the lungs could be more clearly determined and indicated on the stain as this made cross-referencing with the CT easier, formalin fixed for 24 hours and transferred to ethanol prior to being embedded in paraffin blocks for analysis.

3.2.5 OAR Experiments for Uninduced Mice

Uninduced mice were irradiated under anaesthetic (isoflurane in oxygen) with different parallel opposed beam angles and aperture sizes to ensure different dose coverages to OARs that would be relevant for the GEMM experiments, the heart and the liver. OARs for the subcutaneous cohort were not considered as there were fewer critical structures in proximity to the subcutaneous tumour and the subcutaneous experiments were intended to go on for a shorter time. The heart and liver were outlined and DVHs were prepared so the V95 could be extracted and compared to the proportion of the OARs shown to be irradiated on the stains. Mice were culled 30 minutes after irradiation using a schedule 1 method (CO_2 inhalation), lungs were extracted, put into labelled cassettes and so the orientation of the lungs could be more clearly determined and indicated on the stain as this made cross-referencing with the CT easier, formalin fixed for 24 hours and transferred to ethanol prior to being embedded in paraffin blocks for analysis. V95 was used as a measure of PTV coverage as it is a measure of the percentage volume receiving at least 95% of the prescription dose.

3.2.6 Staining

Immunohistochemistry (IHC) was performed by central services. To identify which regions had been irradiated Phospho-histone H2A histone family member X (γH2AX), which visualises DNA damage by staining gamma-H2A histone family member X (γH2AX) foci, was used. Phospho-Histone H2A.X (Ser139) (20E3) Rabbit mAb #9718 was purchased from Cell Signalling Technology.

This stain is used routinely by central services on mouse samples so further optimisation beyond the established protocol was not deemed necessary.

Staining took place on 4 μm formalin fixed paraffin embedded sections (FFPE) which had previously been incubated at 60 ºC for 2 hours.

All FFPE sections underwent on-board dewaxing (AR9222, Leica) and epitope retrieval using ER2 solution (AR9640, Leica) at 95 °C where sections for γH2AX for 20 minutes. Sections were rinsed with Leica wash buffer (AR9590, Leica) before peroxidase block was performed using an Intense R kit (DS9263, Leica) for 5 minutes. Sections were rinsed with wash buffer before application of primary antibodies at an optimised dilution (γH2AX, 1/120) for 30 minutes. Sections were rinsed with wash buffer, and all had rabbit envision secondary antibody (K4003, Agilent) applied for 30 minutes. Sections were rinsed with wash buffer and visualised using DAB in the Intense R kit. To complete the IHC staining sections were rinsed in tap water, dehydrated through graded ethanol solutions and placed in xylene. A cover slip was placed over stained sections in xylene using DPX mountant (SEA-1300-00A, CellPath).

3.2.7 Slide Analysis

Slides were scanned using a Leica Aperio AT2 scanner (Leica Biosystems, Wetzlar, Germany) and uploaded to Halo (Indica Labs, v3.6.4134), a quantitative histology analysis program. Training regions were defined using irradiated and unirradiated tumour slides and adjusted. Allograft tumours were outlined using the magnet and flood tools. Halo's analysis tool was used to identify the proportion of γH2AX positive nuclei within a tumour, and a ratio of this to the proportion of γH2AX negative nuclei was calculated to assess whether the tumour had been fully covered by the dose. A visual inspection of each slide was also performed to ensure that the tumour was fully covered. Necrotic tissue was excluded from the ROIs. Tumours with a necrotic core that was over 50% of the volume were excluded.

3.3 Results

Double strand break analysis was performed in control and irradiated KP allografts by γH2AX assay. The percentage of cells of γH2AX positive nuclei in the experimental groups are shown below. It should be noted that all the irradiated allografts except for one tumour had a percentage of γH2AX positive nuclei that exceeded 70% positive nuclei.

Figure 20 shows a comparison of double strand breaks between control and irradiated KP allografted tumours.

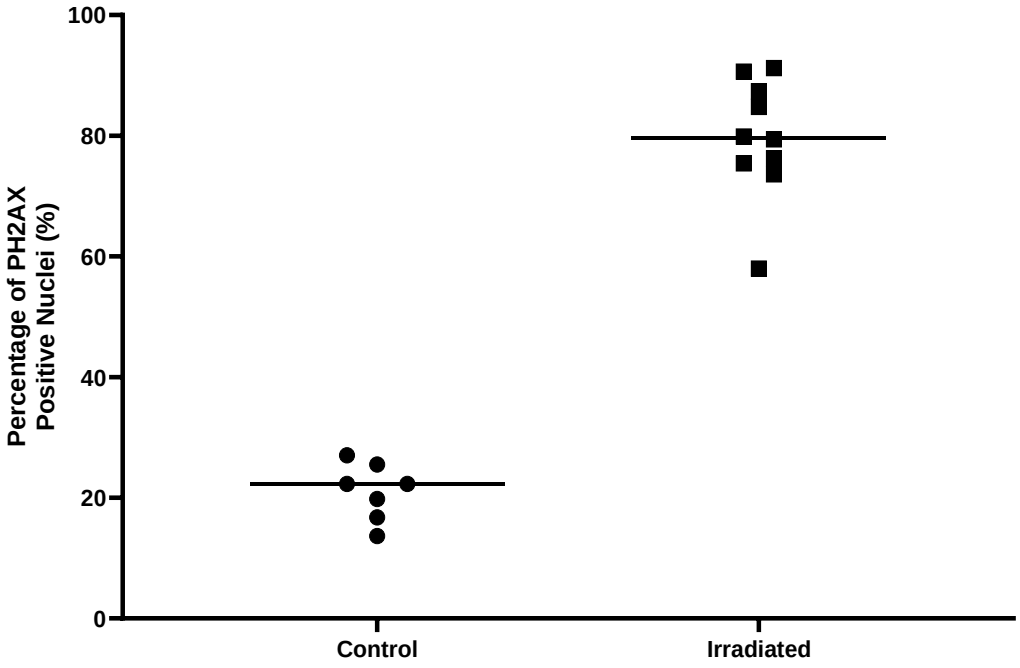

Figure 20. Graph with line representing the mean showing the percentage of γH2AX positive nuclei in each KP allograft subcutaneous tumour (N. tumour=12, N. tumour=17 as some mice received bilateral implants).

A Mann Whitney test was performed and determined that there was a statistically significant difference between the control and irradiated groups (p=0.0001). In addition to this it should be noted that all of the irradiated allografts bar one had a percentage of γH2AX positive nuclei that exceeded 70%.

Figure 21 shows γH2AX staining of irradiated allograft tumours from the data shown in Figure 20. A 1 mm margin was applied; however, it appears from this image that a part of the tumour has little to no positive staining, indicating that the 1 mm margin chosen did not adequately cover this KP subcutaneous allograft.

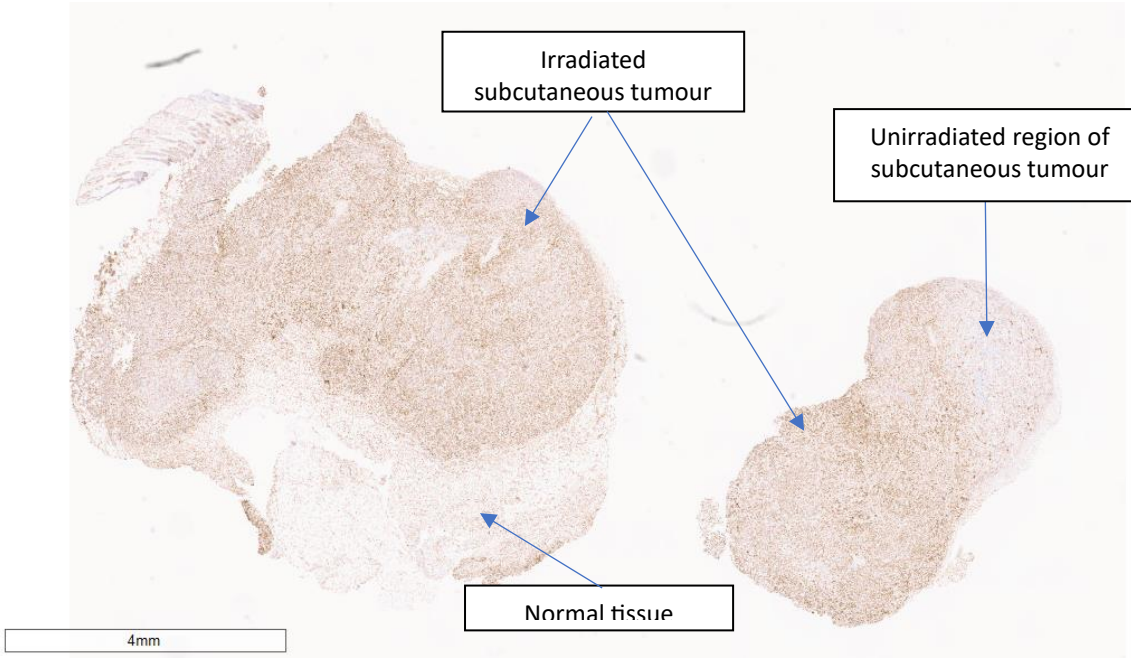

Figure 21. γH2AX stain of KP allograft with lowest γH2AX positive nuclei (right)

The figure above shows γH2AX staining of two subcutaneous KP allografts from the same NSG mouse. Both tumours were irradiated with 16.5Gy/1#. A 1 mm margin was applied.

Figure 22 shows the results of a study in which a single tumour in the lungs of KP GEMM mice were irradiated, except for Mouse 3, where an additional tumour was partially irradiated due to proximity. This figure demonstrates a single lung tumour in GEMM mice can be targeted by using γH2AX positive nuclei as an indication that a tumour has been irradiated. The clear distinction between irradiated and unirradiated tumours indicates that unirradiated tumours did not receive significant incidental radiation, confirming that in these GEMM mice 1 mm margins were adequate for precise targeting of lung tumours.

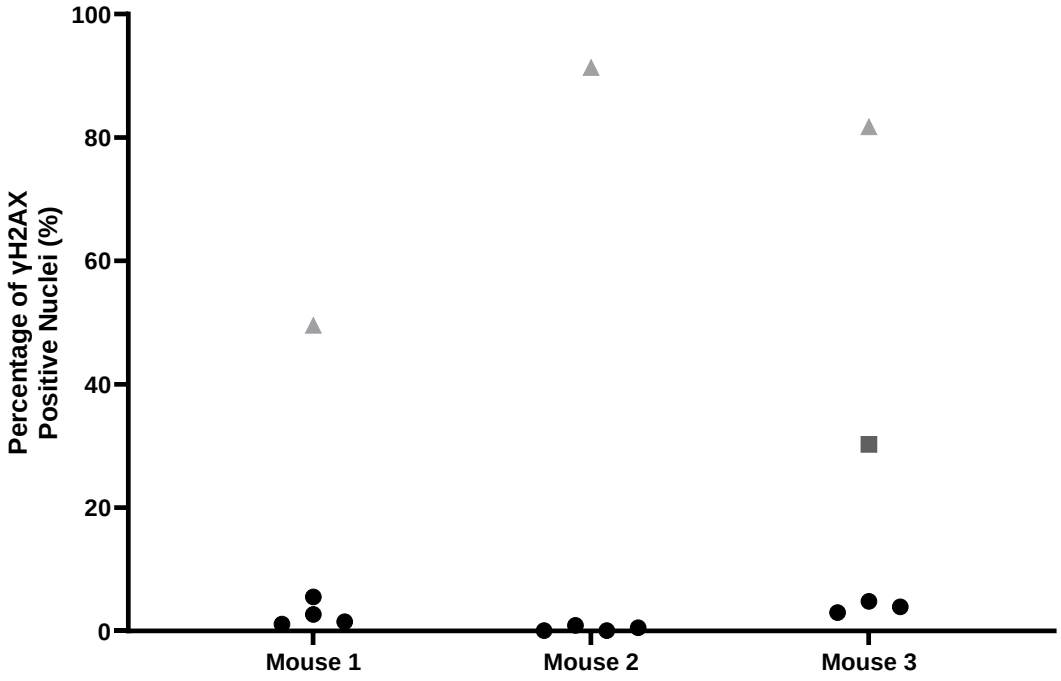

Figure 22. Graph depicting the percentage of γH2AX positive nuclei in tumours from three KP GEMM mice. Data points represent unirradiated (circle), partially irradiated (square), and fully irradiated (triangle) tumours.

A Mann Whitney test shows that there is a statistically significant difference in γH2AX positive nuclei percentage between irradiated and unirradiated tumours (p=0.0055).

Figure 23 presents the data from a study where the livers of uninduced C57BL/6 mice were irradiated. V95, extracted from the DVH for each of the OARs, was used to measure liver coverage. The percentage of γH2AX positive nuclei indicates the proportion of the heart and liver irradiated.

This graph demonstrates a strong correlation between the treatment planning system's calculated dose distribution and the actual dose received by the liver, indicating that the SARRP is delivering dose to the regions planned on the TPS. It should be noted that this only validates that the expected proportion of the liver was irradiated and does not validate the actual dose delivered.

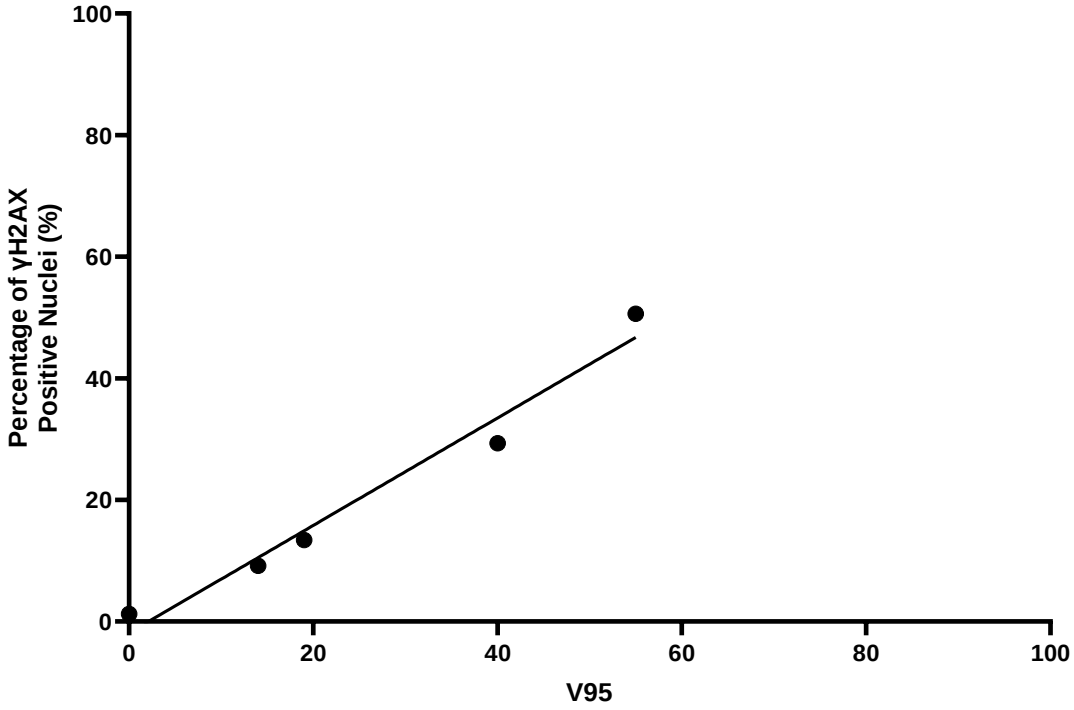

Figure 23. Graph showing the statistically significant correlation between liver V95 and γH2AX liver staining using simple linear regression in KP GEMM mice (N=5).

There is a significant correlation (R^2=0.9699, p=0.0022) between the percentage of γH2AX positive nuclei and the V95 for the liver ROIs. V95, extracted from the DVH, measures liver coverage. The percentage of γH2AX positive nuclei indicates the proportion of the OAR irradiated.

Figure 24 presents the data from a study where the hearts of uninduced C57BL/6 mice were irradiated. V95, extracted from the DVH for each of the OARs, was used to measure heart coverage. The percentage of γH2AX positive nuclei indicates the proportion of the heart and liver irradiated.

This graph demonstrates a strong correlation between the treatment planning system's calculated dose distribution and the actual dose received by the heart, indicating that the SARRP is delivering dose to the regions planned on the TPS. It should be noted that this only validates that the expected proportion of the heart was irradiated and does not validate the actual dose delivered.

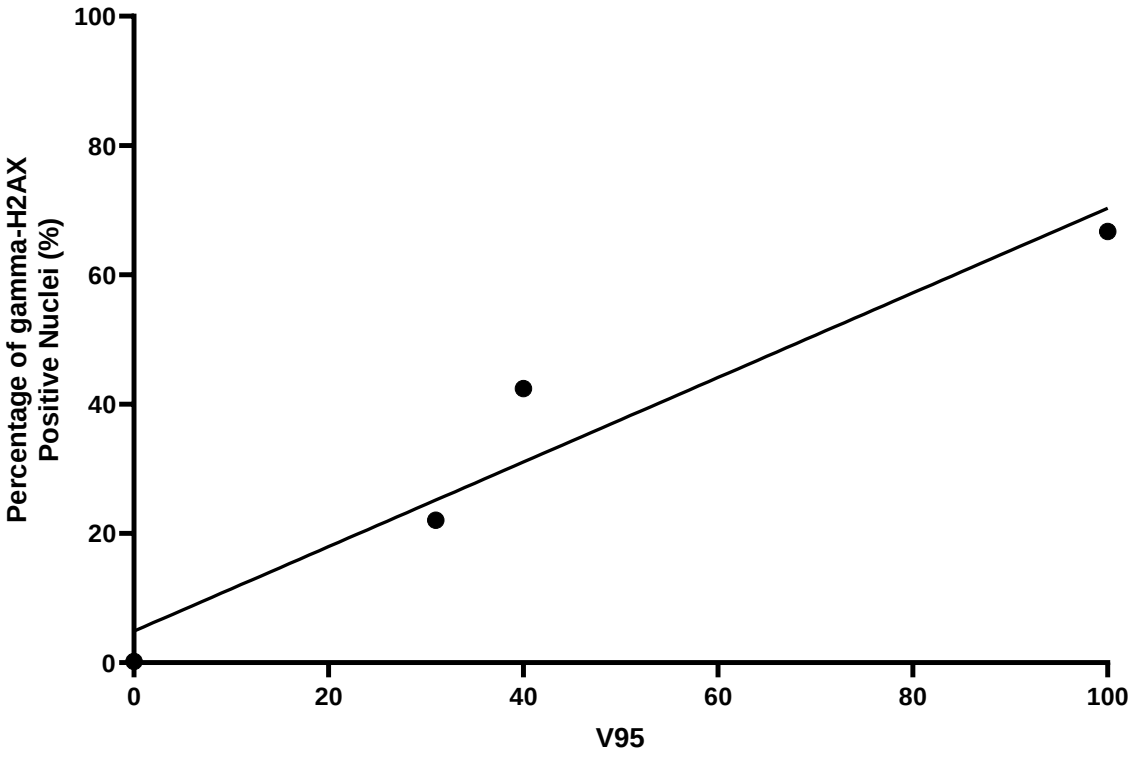

Figure 24. Graph demonstrating a statistically significant correlation between heart V95 and γH2AX heart staining using simple linear regression. (KP GEMM, N=5).

There is a statistically significant (p=0.0364) correlation (R2=0.9285) between γH2AX positive nuclei and the V95 for the heart ROIs. V95, extracted from the DVH, is being used as a measure of heart coverage

3.4 Discussion

3.4.1 Summary of Objectives

- **Ensure that the selected margins adequately cover the subcutaneous tumours.**

While Figure 20 shows that most tumours were covered by the chosen margin of at least 1mm, one tumour (shown in Figure 21) received less coverage than the others. The reasons for this were identified and treatments were adjusted for future mice. Histology confirmed that this only occurred in one tumour.

- **Ensure that margins cover the GEMM tumours.**

The margin of at least 1mm covered the three tumours irradiated adequately (see Figure 22). However, it was impossible to avoid dosing one of the surrounding tumours due to its overlap with the margin. This issue was highlighted by the treatment plan, so it does not qualify as an unexpected irradiation.

- **Check that the dose delivered to the OARs matches that calculated in the treatment planning system.**

There was a strongly significant difference between the volume in the OARS receiving 95% of the dose as calculated in the treatment planning system and the proportion of the liver and heart samples that were shown to have been irradiated using γH2AX, as shown in Figures 23 and 24.

3.4.2 Discussion

The results for the GEMM experiment showed that in the three mice it was possible to target individual tumours when there was no overlap, although due to the low sample size it should be interpreted as a proof of concept that a 1 mm minimum margin can work rather than a demonstration that it is always suitable. However, these findings also seemed to contradict those in the murine respiratory phantom study, which indicated that movement in the Z-direction could potentially result in partial irradiation due to movement of up to 4mm for tumours near the diaphragm (Heyden et al, 2017).

A possible reason why the 1 mm minimum margins may have been sufficient in this study but not in the murine respiratory model is because of the exclusion criteria applied to prevent inaccurate length measurements in the GEMM experiments. The mice in this experiment were sourced from GEMM mice that were originally intended for the PET experiments but displayed clinical signs that indicated they would not reach experimental endpoint. However, the criteria for tumour selection remained the same, including the stipulation that tumours that were pressed against the rib cage or diaphragm to the extent that differentiating them from the surrounding tissue would become difficult on CT should be excluded. While this was not intended to specifically exclude all tumours near the diaphragm, in practice tumours close to the diaphragm often ended up embedded against it. For the GEMM mice it also appeared as though superiorly placed tumours were more common than inferior tumours, which may be because of the intranasal induction method.

Another reason could be that the murine phantom modelled the movement of a single tumour in the lung. It is possible that having multiple tumours in close proximity may affect how free the tumour is to move and thus restrict its range of movement. While the results from the initial three irradiated tumours indicate that are margins are sufficient there are many aspects of GEMM tumour motion and tumour targeting that could benefit from further clarification.

One of the KP allografts only receiving a partial dose with a 1mm margin required investigation. After reviewing the γH2AX staining of the allograft on the post-treatment MRI and looking at the plan on the treatment CT it became

apparent that the issue was that two bilateral tumours had grown next to each other and it was impossible to treat them both separately due to their proximity; attempting to do so would have led to overlap of the treatment beams and one or both of the tumours receiving double the prescription dose (See Figure 25).

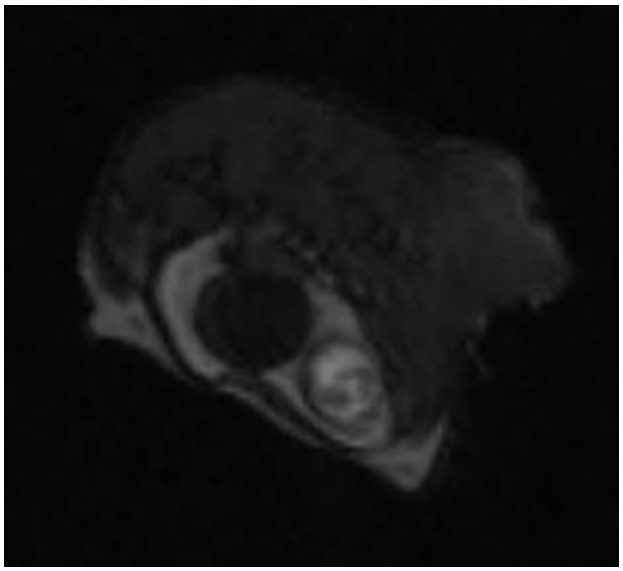

Figure 25. Post-treatment T1-weighted GRE MRI showing two subcutaneous KP allograft tumours in close proximity (N. Tumour=1). Tumours are located on the right flank of the mouse.

This growth pattern significantly impeded treatment planning and made it impossible to accurately target both tumours.

At the time it was decided that both tumours should be irradiated with a single beam using the motorised variable collimator to cover the whole area with a margin of 1 mm. However, the odd shape of the allograft and the awkward placement clearly resulted in the size of the tumour being miscalculated, resulting in the partial irradiation of one of the tumours that was then detected using γH2AX. Given this issue, the plan for dealing with tumours growing together as in this mouse was reassessed for Allograft Experiment 2.

The accordance between the OAR ROIs and the treatment planning system calculated quality metrics from the DVHs validated the calculation of the dose distribution from the treatment planning system. This means that further treatments could proceed with confidence that no structures were getting more than the known dose. However, this validation only counts for the ant-post parallel opposed beams used in the subcutaneous and GEMM experiments in this

thesis. An arc beam (or multiple arc beams) would potentially have a much more complicated dose distribution where some regions are partially irradiated, and while the normal tissue has a more homogenous radiation damage response than the tumours it could still contribute to uncertainty when determining what proportion of the tissue had been fully irradiated.

3.4.3 Limitations

One complication that arose was that in one of the GEMM mice there was no tumour that could be irradiated completely without partially irradiating another tumour. This is reflective of one of the issues that arose in the PET experiments detailed in Chapter 6 as well; targeting individual tumours is often difficult, and in models without sufficiently separated tumours (such as the KMyc model), impossible.

A larger dedicated GEMM experiment with low titre KPs would be beneficial; because the targeting experiment was just a supplement to the ^{11}C-acetate PET experiment, with the cohort being drawn from mice unsuitable for the PET experiments, very few tumours ended up being irradiated. A dedicated cohort of low titre KPs with far apart tumours which are less difficult to target would be ideal, and this dedicated cohort would mean a much larger sample size that would ensure that greater confidence in the targeted treatment planning techniques used.

To ensure full coverage of the subcutaneous tumours, margins were extended to 2 mm. The therapeutic ratio is of less concern in the subcutaneous tumours than for the GEMM tumours because there are fewer critical structures in proximity. It was also decided that if tumours with a similar growth pattern to that observed in the partially irradiated tumour were found again in allograft experiment 2 that only one of the tumours would be irradiated and that the other tumour would be discarded. This was to avoid partial irradiations potentially biasing the next study.

Another thing to consider regarding in vivo verification of margins is that while this study has attempted to characterise factors that contribute to the size of the planning target volume, no attempt has been made to estimate a margin to

grow the GTV by to create the CTV. A study using markers of proliferation such as the immunohistochemical marker Ki-67 or the in vivo PET imaging biomarker ^{18}F-3'-fluoro-3'-deoxythymidine (FLT) to assess subclinical spread could determine what margin is necessary to treat malignant tissue outside the GTV and would complement the work done here to address geometric uncertainties.

4. CT AERATION RATIO AS AN EARLY IMAGING BIOMARKER OF RADIATION INDUCED LUNG INJURY

4.1 Introduction

4.1.1 Background

In Chapter 3, γH2AX staining was used to determine whether tumours or organs had been irradiated by using γH2AX positive nuclei as an indication that a region had been exposed to radiation. An imaging biomarker of radiation induced lung damage in vivo would also be useful as this could both be used to identify mice that would benefit from enhanced inspection and, if it were proved to correlate with survival, could be used to explain differences in survival between mice with similar tumour burdens and other clinical signs.

This chapter explores the imaging biomarker explored in Mark Jackson's 2022 paper looking at the anti-inflammatory effects of low dose radiotherapy on a mouse model of COVID-19 (Jackson et al, 2022) to assess whether it could be useful in the context of radiation induced lung damage as well. This paper used the proportion of poorly aerated lung defined through HU thresholding as a marker of lung disease, as had been demonstrated previously in Ruscitti et al's 2017 paper assessing the correlation between Micro-CT quantified lung fibrosis and histological staining (Ruscitti et al, 2017). This section will discuss an experiment intended to demonstrate whether the CT quantified aeration ratio could be used as an early biomarker of radiation induced lung injury in mice, correlating the change in aeration ratio between 0 and 4 weeks with survival.

Three treatment groups were used in this experiment: a group where the whole lung was irradiated to represent the KMyc mice which could not have their tumours individually targeted as they were not sufficiently separated; a targeted parallel opposed beam treatment based on the treatment plan for an GEMM mouse that had already been scanned at the point of this experiment, and a sham irradiated group which acted as the control. Additionally, this study was

used to inform our approach to the PET experiments by providing information on how the mice responded over time after receiving radiotherapy.

4.1.2 Objectives and Analysis

- Determine whether the mice tolerate the treatment and what timeline can be expected for normal tissue effects to become apparent

The clinical signs and changes in body weight relative to baseline were plotted. Any changes to regimen for mouse welfare were noted and applied to the PET experiment.

- Assess whether aeration ratio of the lungs have predictive value as an early imaging biomarker of normal tissue damage

The Lung CT Analyzer tool in SlicerCIP was used to quantify poorly and normo-aerated volumes, and the change in the ratio of these volumes was correlated with the survival. A Spearman's Rank Correlation Coefficient was used as it is a non-parametric test that can be used with small sample sizes, although it should be emphasized that the small sample sizes mean that the data may not be generalisable. The change in Mean HU for each lung segmentation was also quantified and correlated with the survival to use as a comparison with the aeration ratio.

4.2 Materials and Methods

4.2.1 Mice

Female C57BL/6 mice (n = 20) were ordered from Charles River to ensure consistency across the cohort. To align these mice as closely as possible to the cohort of C57BL/6 mice that were to be used in the PET experiments, these mice were aged to 20 weeks prior to irradiation as tumour development takes at least 12 weeks in our models and mice are usually induced at 6- 8 weeks. This was done because age can affect the radiosensitivity of normal tissue in mice (Tong & Hei, 2020). Each treatment group was intended to have 6 mice; however, due to abnormalities in the initial CT scan 3 mice had to be culled due to lobe collapse. As these mice had not been treated, the lobe collapses that appeared across different cages of mice within the cohort were assumed to pre-date their arrival. The flowchart in Figure 26 shows the intended and actual cohort size, and the reasons for losses in the cohort at different stages.

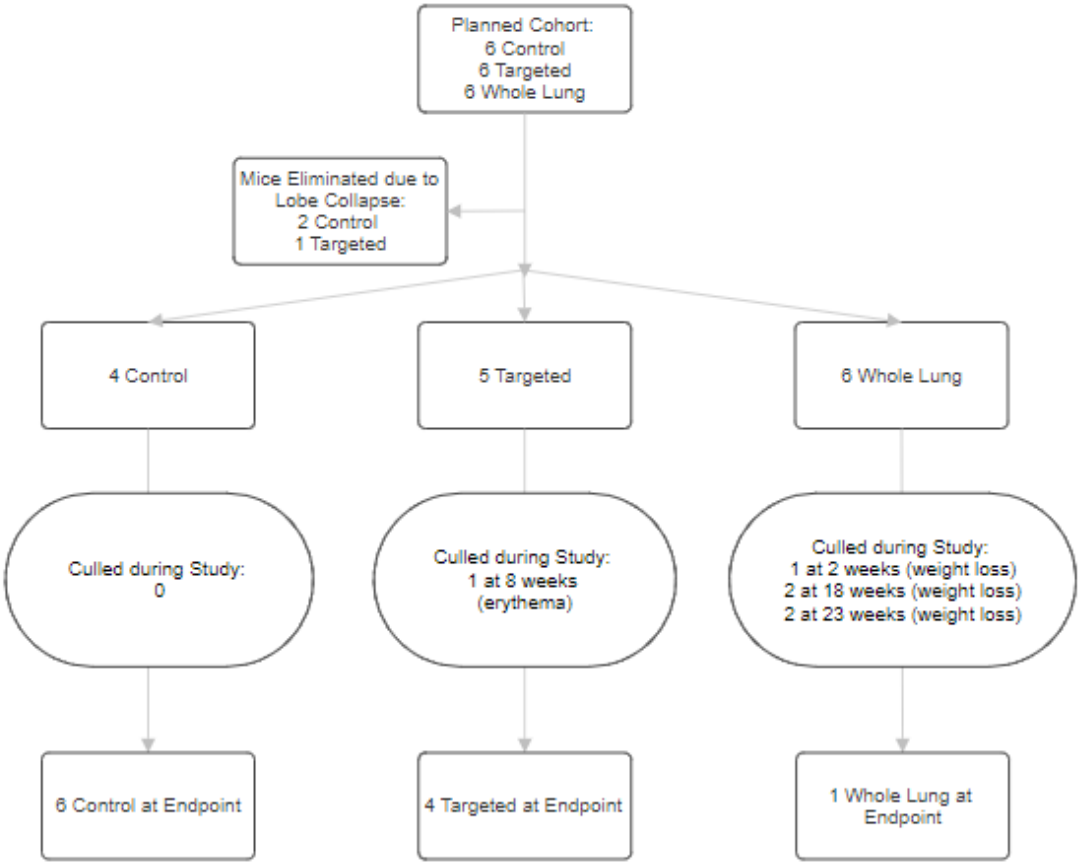

Figure 26. Flowchart showing causes of losses in the CT Aeration Ratio cohort.

From the planned cohort of 6 mice in the control, targeted and whole lung treatment groups, 3 mice were eliminated due to lung abnormalities; 2 from the control group and 1 from the whole lung group. 4 of 4 mice survived to endpoint in the control group, 4 of 5 in the targeted group and 1 of 6 in the whole lung group.

4.2.2 Experimental Timeline

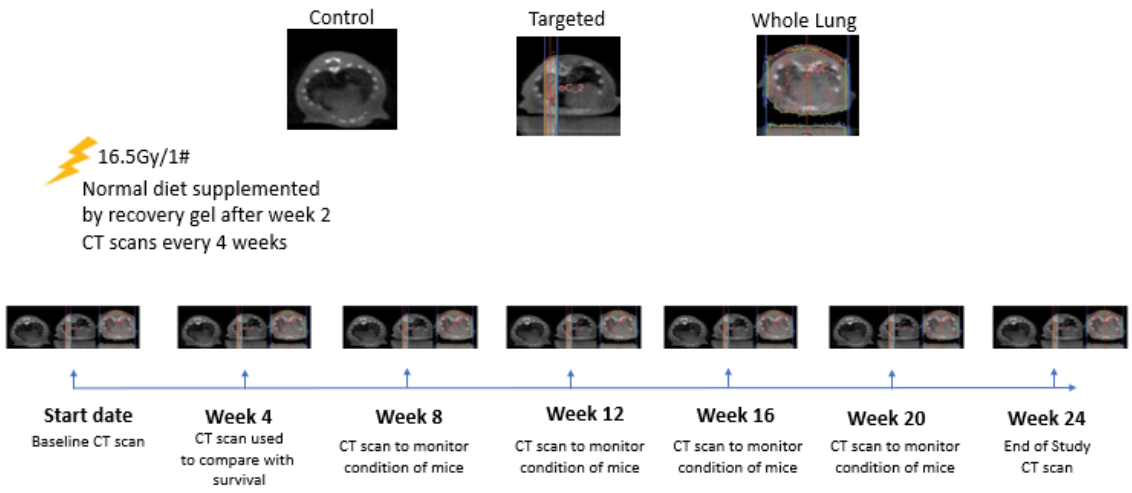

Figure 27. Experimental timeline for CT Aeration Ratio Experiment

There were three experimental groups, with 6 mice planned for each group: a CT only group, a targeted group based on a treatment plan adapted from a KP GEMM treatment plan, and a whole lung irradiated group. The irradiated mice received a single fraction of 16.5Gy to match the GEMM PET experiments.

4.2.3 Cone Beam CT Protocol

The SARRP's onboard cone beam CT, scanning with 1440 projections at 60 kVp and 0.8 mA using the fine focal spot (1 mm). The Feldkamp, Davis, and Kress CBCT algorithm was used for reconstruction of CT images (Feldkamp, Davis & Kress, 1984).

Mice were CT scanned prior to irradiation and screened to ensure that there were no lung abnormalities that could complicate CT analysis, and 5 mice were excluded due to partial lobe collapses. Mice were scanned at 1 month to acquire the images used to assess whether the aeration ratio of the lung could act as an early imaging biomarker for normal tissue complications and scanned monthly thereafter to monitor for pleural effusion and lobe collapses. This is summarised in Figure 27 above. The mice were monitored for pleural effusion as C57BL/6 mice are more prone to this than other strains (Jackson et al, 2010) and monitored for lobe collapse because of the abnormalities noted on the first CT scans prior to treatment.

4.2.4 Irradiation Protocol

All mice were anaesthetised with isoflurane in 95% oxygen prior to irradiation. Mice were assigned to 3 groups:

Whole Lung Irradiation group (n=6)

Mice were irradiated using a motorised variable collimator that was adjusted to give a 1 mm margin around the lungs and received a single fraction of 16.5 Gy (voltage and current settings for the treatment beam were 220 keV and 0.13 mA). An ant-post parallel opposed beam arrangement was chosen as this delivers a more homogenous dose across the lungs than a single ant beam or a lateral arrangement.

Targeted parallel opposed beams (n=5)

As these were non tumour bearing mice the treatment plans were based on a two isocentre APPA treatment plan ported from a treatment plan for a KP GEMM. They also received a single fraction of 16.5 Gy.

CT only (n=4)

This group received no treatment but were sham irradiated (CT scanned in the same session as the intervention group but did not receive radiotherapy) and acted as the control group.

4.2.5 CT analysis protocol

As CT output for the SARRP is in arbitrary units rather than Hounsfield Units (HU) prior to analysis it was necessary to perform a calibration. For this 3D Slicer Chest Imaging Platform's Lung CT inbuilt calibration tool was used. The lung was segmented using semi-automatic thresholding, with each segment being manually inspected and adjusted if necessary to exclude other tissues. The Lung CT Analyzer tool in SlicerCIP was used to quantify aerated and unaerated volumes, with normo-aerated lung defined as having -900 to -500 Hounsfield Units (HU) and poorly aerated lung being defined as having -500 to -100 HU (Jackson et al, 2022). The ratio of normo- to poorly aerated lung volume was calculated from these values generated by the Lung CT Analyzer tool. Examples of these ROIs can be found below in Figure 28.

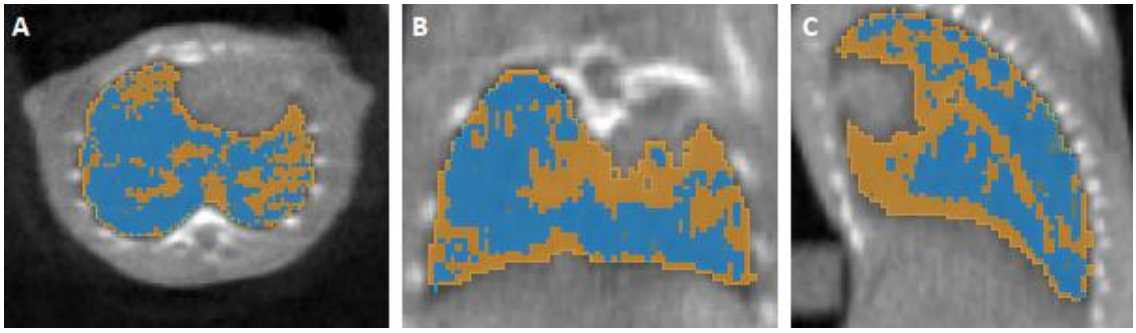

Figure 28. CT scan showing ROIs of the normo-aerated (blue) and poorly aerated (orange) lung volumes in the axial (A), sagittal (B) and coronal (C) views.

The aeration ratio of the mice at 4 weeks post treatment was compared to survival time to see if this could act as an early biomarker of normal lung damage.

4.3 Results

The clinical signs and changes in body weight relative to baseline were plotted for 15 mice (n. CT only=4, n. Targeted=5, n. Both lungs=6) were plotted. After initial decline from baseline weight was recovered through dietary changes (nutra-gel) for mice with both lungs irradiated and was then maintained relative to controls until the final 2 weeks of the experiment. Upon the initial weight loss in the whole lung group, nutra-gel was administered to all mice, resulting in the recovery of the whole lung mice within one week. The point at which nutra-gel was added is indicated on the graph with a black vertical line.

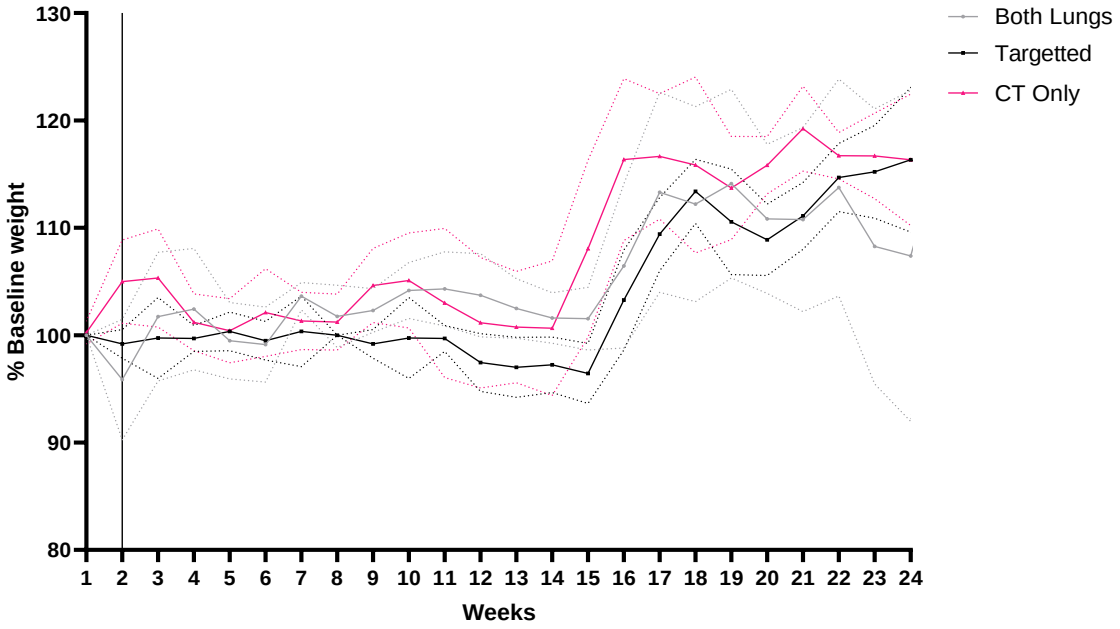

Figure 29. Weight trajectory over time for the control, targeted and whole lung irradiation groups (n. CT only=4, n. Targeted=5, n. Both lungs=6).

The graph shows the average weights of the 3 treatment groups per week. The dotted line represents the standard deviation.

A Spearman's rank correlation found a statistically significant correlation between the change in aeration ratio from Week 0 to Week 4 and the survival time (r_s = -0.94868, p (2-tailed) = 0.01385). This indicates that a larger change in aeration ratio (specifically when the proportion of poorly aerated lung has increased from the pre-treatment scan to Week 4) may be associated with a lower survival time for the mouse. However, due to the low sample size this result may not be generalisable. The data for mice in the other groups is not shown because all the mice in the control group survived for the full length of the experiment and all the mice in the targeted group also survived with the exception of one mouse which was culled due to erythema and showed no other clinical signs.

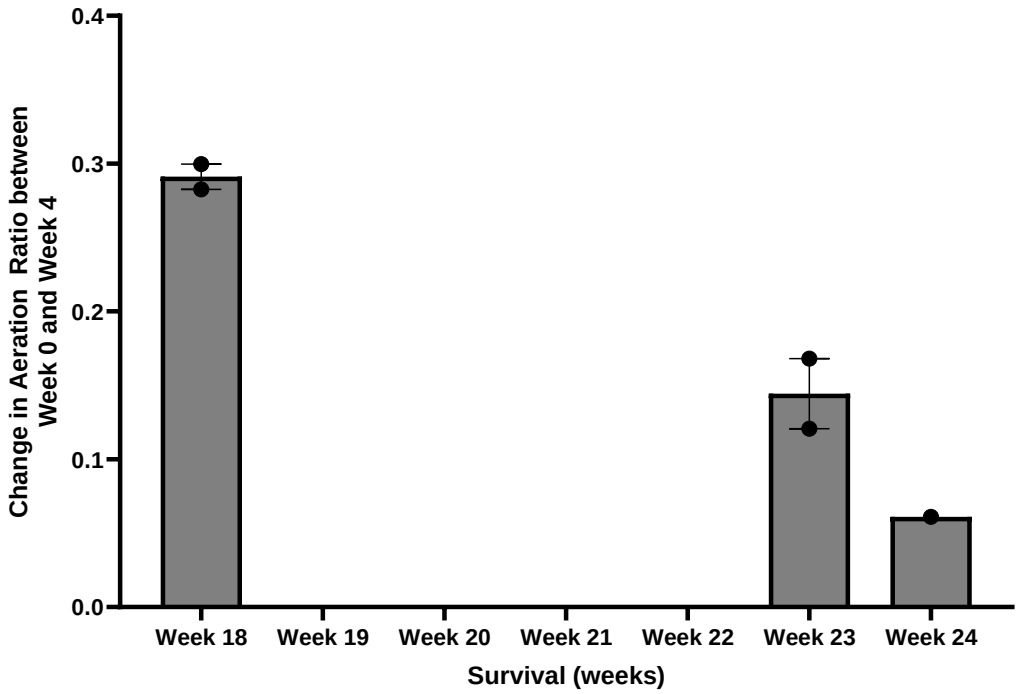

Figure 30. Bar chart illustrating the relationship between survival time (in weeks) and the change in aeration ratio between Week 0 and Week 4 CT scans for mice in the whole lung irradiation group (N=5).

The change in aeration ratio is the change in the ratio of poorly aerated to normo-aerated lung between weeks 0 and 4. The bars represent the mean and the individual values for each mouse are represented by the dots.

While there appears to be a trend with a greater change in Mean HU resulting in a shorter survival time, a Spearman's rank correlation found no statistically significant correlation between the two (rs = -0.73786, p (2-tailed) = 0.15462). As a statistically significant correlation was found between the change in aeration ratio and the survival in weeks this could indicate that this metric is less sensitive than the change in aeration ratio in Figure 30.

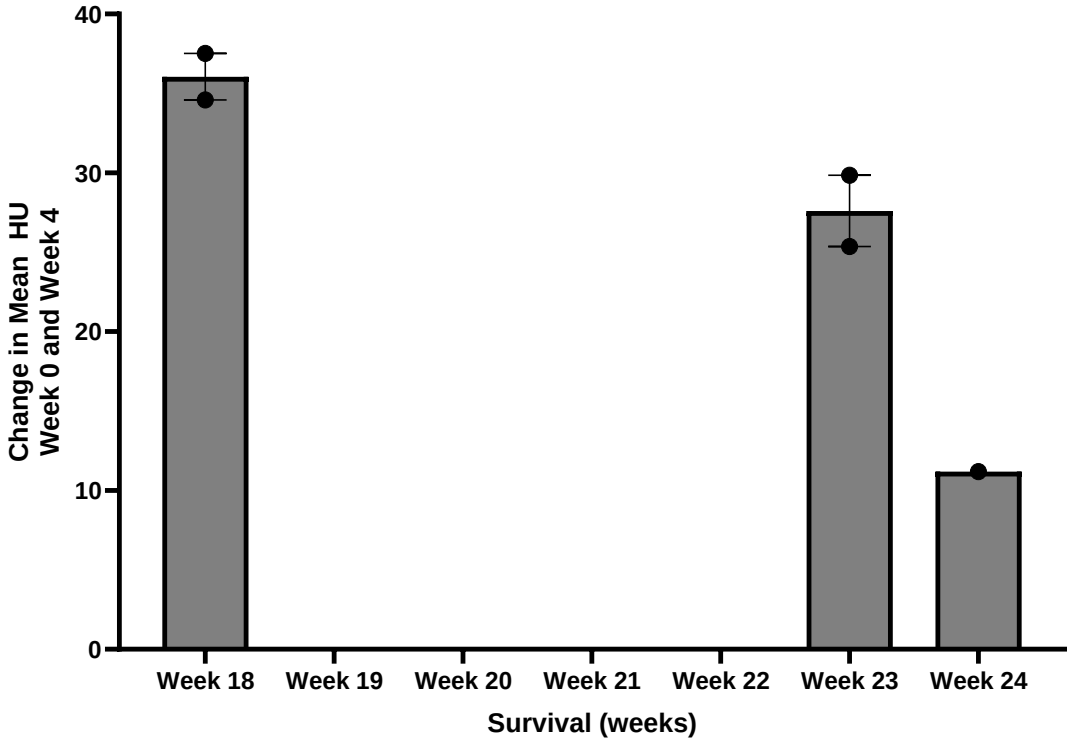

Figure 31. Bar chart illustrating the relationship between survival time (in weeks) and the change in mean Hounsfield Units (HU) between Week 0 and Week 4 CT scans for mice in the whole lung irradiation group (N=5).

The bars represent the mean and the individual values for each mouse are represented by the dots. A Spearman's rank correlation found no statistically significant correlation between the two (r_s = -0.73786, *p* (2-tailed) = 0.15462).

4.4 Discussion

4.4.1 Summary of Objectives

- Determine how radiation induced normal tissue damage might affect weights and clinical signs over time independently of tumour burden.

Weights for the group that had whole lung irradiation dropped at week 2 until the introduction of the grain-based wet food nutra-gel. This caused weights to recover and was then used for treated and control mice in the GEMM experiments from the first ^{11}C-acetate PET scan until the final endpoint.

- Gauge whether the aeration ratio in early post treatment CT scans could be an early imaging biomarker of radiation response.

Both the change in mean HU and aeration ratio were assessed for correlations with survival using a simple linear regression. Only the whole lung data was assessed as all the control cohort survived to endpoint and all but one of the mice receiving targeted radiotherapy survived to endpoint. The mouse from the targeted group that was culled early was also culled due to erythema, not any clinical signs associated with lung damage. The aeration ratio (Figure 30) was found to be significantly correlated with survival while mean HU (Figure 31) was not.

4.4.2 Discussion

Of the 3 treatment groups the only mice that demonstrated signs of respiratory distress or hunching throughout the duration of the experiment were the mice treated with the whole lung irradiation. Only one mouse had to be culled from the targeted irradiation group and this was because of skin damage that had begun to look as if it might ulcerate. An important finding from this study was that nutra-gel administration could completely recover the weight of the whole lung irradiation mice and maintain it close to baseline for months. This could indicate that the radiation induced normal tissue damage that has the most limiting effect on mouse welfare is oesophageal as this is the OAR in the region of the lung that would be most likely to result in mice that had not lost their appetites but were unable to eat anything other than soft food. All whole lung irradiation mice bar the one that had to be culled in the first month developed radiation pneumonitis that was apparent either via CT imaging before being culled or upon dissection.

The comparison of the early predictive quality of the change in Mean HU (Figure 31) and aeration ratio between weeks 0 and 4 yields several interesting points. The first is that the results of this study validate the hypothesis that changes in the proportion of poorly aerated lung is more sensitive to changes than the Mean HU, which was also indicated in CT quantification work that we did for the Low Dose Radiotherapy for COVID-19 paper mentioned in the introduction to this Chapter (Jackson et al, 2022).

This does not mean that Mean HU cannot detect this damage at all; there is a trend in the Mean HU data which indicates that the measure may be confounded by the low sample size (n=5). This aligns with previous research that indicates that Mean HU is predictive of radiation pneumonitis (Du et al, 2021) but that it can lack the sensitivity to act as an early detection biomarker until after 3 months or more pass when the damage is more significant (Phernambucq et al, 2011). It was not possible to verify this in this study due to the issues with pleural effusion that the mice in the whole lung group began to develop after 12 weeks, although if the experiment were repeated with a strain less prone to pleural effusion such as C57L validating this could be possible.

It should still be noted that a high-quality CT scan analysed by a radiologist can provide information on whether a patient has normal tissue damage to their lung at 4 weeks using characteristic imaging biomarkers such as ground-glass opacities, (Benveniste et al, 2019) so an imaging modality and analysis technique being able to achieve this is not novel in and of itself. However, preclinical CBCT scanners such as the one at the SARRP do not detect subtle features as well as clinical CT scanners, and when they do the staff may not be trained to recognise them as reliably as a qualified radiologist. Calculating the aeration ratio in 3D slicer is an open source and accessible quantitative method that is reproducible.

The variation in the response of normal lung tissue across the whole lung irradiation group was also notable. Female C57BL/6 mice were ordered in rather than bred specifically to ensure that the cohort was as homogenous as possible, they received the same food and were treated within a few days of each other, but there was still noticeable intragroup variety in both the survival and the aeration ratio in the lungs. This is concerning because of the implications it might have for future GEMM studies, particularly considering how close together the KMyc tumours were; because of this it was not possible to perform targeted irradiation on that model's tumours, even when induced at a relatively low titre (5×10^5 PFU/ml), meaning that normal tissue was unavoidably irradiated in large quantities.

For the one week follow up study in this thesis the issue could be avoided because the outcomes were related to tumour growth and imaging data. In a longer treatment response study that looked at clinical signs and survival it could be difficult to distinguish which signs are the result of increasing tumour burden and which are the result of a particularly radiosensitive mouse in the treatment group. This emphasizes the importance of growing far apart tumours which are easier to target, something which will be discussed further in Chapter 7.

4.4.3 Limitations

A complication that affected the options to analyse the weight data was the inability to adequately outline the oesophagus on the CT scans. This meant that while it is possible to postulate that oesophageal damage is a major contributor to the low survival in mice that had their whole lungs irradiated, this cannot be verified. Integrating MRI imaging early and registering it with the CT could allowed for better OAR delineation at the cost of the mice being anaesthetised for a longer time. Collecting the oesophagus when culling the mouse that died at two weeks for histology would also have provided useful data.

Another major limitation of this study was the lack of verification of the findings with histology or other imaging modalities. It was originally intended that ^{18}F-FDG scans would be used to assess inflammation at 12 weeks and for these results to be compared to the early CT scans using image registration. However, it was not possible to fast the mice prior to the experiment for a sufficiently long-time to ensure optimal ^{18}F-FDG uptake as this would have breached the conditions of the license, so due to poor signal to noise ratio these data could not be used. Cross-referencing the CT scans with H&E and Masson's Trichrome staining to quantify the normal tissue abnormalities and compare them with the areas of poorly aerated lung on the CT would also have improved confidence in the results.

The low sample size posed problems when analysing the results. The statistical test used was a Spearman rank correlation test, and while this can be used with low sample sizes, the results cannot be generalised as there is a high chance that these samples may not be representative of the general population (Tipton et al, 2016). As a result, the results should only be taken as indicative of a possible association, although the analysis was useful for comparison between the change in Mean HU and change in aeration ratio.

One limiting factor that arose during the experiment is that this study was originally intended to compare aeration ratio longitudinally over the course of the study, but from weeks 12 onwards pleural effusion made this impossible for some of the mice. This limited the study to looking at aeration ratio as an early biomarker of imaging. C57BL/6 mice are known to present with pleural effusion

after radiotherapy more often that other strains such as C57L (Jackson et al, 2010). C57BL/6 mice were chosen to emulate the mice used in the PET experiments as closely as possible, but a different strain such as C57L could be used in a study looking at CT quantified aeration ratio more broadly.

Another limitation is that the earliest post treatment scan performed in the last experiment was at 4 weeks; a follow up experiment that investigated whether the same technique could be used to even earlier would be of interest, especially if supported by histology such as H&E and Masson's Trichrome staining to quantify normal tissue abnormalities. Mice could be scanned at 1, 2, 3 and 4 weeks with a proportion of mice being culled each week until week 4 to collect histology. After this the remaining mice would be entered into a survival study, and their survival time used to assess correlation between survival and aeration ratio at earlier weeks. The reason it would be useful is that it could determine exactly how early changes aeration ratio could begin to act as an imaging biomarker for radiation induced lung damage and support those findings with a histological ground truth.

5. POSITRON EMISSION TOMOGRAPHY IN SUBCUTANEOUS MOUSE MODELS OF LUNG CANCER

5.1 Introduction

5.1.1 Background

In this chapter, two in vivo ^{11}C-acetate imaging studies using subcutaneous mouse models of NSCLC are analysed. PET imaging of subcutaneous mouse models of lung cancer has been performed before; for example, human A549 lung carcinomas were implanted in mice and imaged with ^{18}F-FDG and ^{18}F-Fluoro Azomycin Arabinoside to investigate hypoxia (Graves et al, 2010), and in Liapis et al's 2021 paper ^{89}Zr-Zr-chDAB4 was explored as an imaging biomarker of chemotherapy response (Liapis et al, 2021). However, there are currently no studies using subcutaneous models of lung cancer to investigate ^{11}C-acetate PET as a radiotherapy biomarker.

Originally, more complex pre-and post-treatment comparisons were planned, but due to an ongoing technical fault at the PET centre during the experiments these plans could not be fully realised. As a result, the scope of the experiments was limited to a single treatment response study using ^{11}C-acetate and a second experiment looking at growth kinetics without PET. The aspects of the original experimental endpoints that were realised are still analysed in this chapter and are discussed in Section 5.1.2.

While it is more typical to use subcutaneous xenografts such as the abovementioned A549, in this study subcutaneous allografts from lung derived $Kras^{G12D/+\ p53-/-}$ (KP) tumours were used. This is because the purpose of this experiment was to complement the more complex GEMM studies. Had the subcutaneous allografts been used as extensively as originally intended, the use of subcutaneous implants derived from the tumours from one of the experimental GEMM models would have facilitated direct comparisons when analogous experiments were carried out on both subcutaneous and GEMM models.

There were several reasons why subcutaneous tumours were used in addition to GEMMs despite the advantages of the latter (such as better recapitulation of the tumour microenvironment); firstly, latency times for low titre GEMM experiments like those discussed in Chapter 6 can result in significant downtime experimentally. Secondly, the GEMM tumours display notable inter-tumour metabolic heterogeneity, a characteristic which is useful for exploring how metabolic differences can affect radiotherapy response but potentially problematic when it comes to ensuring that all arms of an experiment are adequately powered. By using data gathered from in vitro cell profiling performed on the cell lines previously by members of the lab (Dzien, Bielik and Lewis, 2017; 2018a; 2018b) we intended to investigate whether we could select cell lines with known acetate avidities that might translate into similar acetate avidities in vivo, enabling us to plan experiments with much more certainty than is possible with the GEMM mice.

5.1.2 Objectives and Analysis

- Identify metabolically heterogeneous models of lung cancer that would provide the variability in ^{11}C-acetate uptake necessary to determine an association between ^{11}C-acetate uptake and radioresistance.

  The data for this objective were gathered in Allograft Experiment 1, but the analysis for this will be carried out in Chapter 6 as these data must be compared to those gathered during the GEMM experiments

- Establish whether there is any change in ^{11}C-acetate acetate avidity post-radiotherapy

This was assessed in Allograft Experiment 1 by comparing the ^{11}C-acetate SUVMax on the PET scan taken on Day 14 to the ^{11}C-acetate SUVMax PET scan taken on Day 17. The purpose of this was to examine whether there were any differences in post treatment ^{11}C-acetate avidity that could be further investigated in Allograft Experiment 2. As Allograft Experiment 2 could not be fully realised due to an ongoing technical fault in the PET centre and the ^{11}C-acetate PET uptake in this experiment was ultimately not high enough to justify

further subcutaneous tumour implantations this aspect was not pursued further beyond the analysis of the initial results in section 5.3.

- Establish whether KP allografts have sufficiently varying radiotherapy treatment responses to be used to assess the relationship between fatty acid synthesis and radioresistance.

This was assessed in Allograft Experiment 2. This was originally intended to be a robust ^{11}C-acetate PET experiment that would look at the relationship between post-treatment growth and changes in acetate avidity. However, as there was an ongoing technical fault in the PET Centre that prevented the production of ^{11}C-acetate, the focus changed to studying the growth kinetics of the tumours. The relationship between cell line (T13, T19b and T25) and post-treatment growth was assessed using paired T tests.

5.2 Materials and Methods

5.2.1 Cell lines

Three different cell lines from lung-derived $Kras^{G12D/+}$ $p53^{-/-}$ (KP) tumour were selected. In vitro cell profiling performed previously by members of the laboratory group measuring ^{14}C-acetate uptake informed the decision regarding what cell lines to choose (Dzien, Bielik and Lewis, 2017; 2018a; 2018b). These experiments showed that T13, 19b and T25 represented the full range of acetate metabolism available in our cell lines; T13 had the highest normalised ^{14}C-acetate uptake across multiple experiments while T25 had the lowest, with T19b falling between the two (ibid). These cell lines were selected with the expectation that the range of acetate avidities observed in vitro would translate to a wide range of acetate avidities in our subcutaneous tumours. Additionally, all the cell lines selected were from different tumours in the same mouse with the intention of reducing non-metabolic variation between the tumours.

5.2.2 Cell culture

See section 3.2.2.

5.2.3 Implantation

See section 3.2.3.

5.2.4 Mouse Monitoring

Mice were monitored for body condition by visual inspection. They were checked for clinical signs such as hunching and ulceration, had allograft measurements taken and were weighed three times a week and culled if they showed signs that they might reach endpoint before the end of the experiment (body weight <80% of starting weight, hunching, or tumour ulceration).

5.2.5 Tumour measurement

Tumour measurements were taken using callipers and mice were shaved prior to measurement to ensure an accurate reading. The longest length of the tumour and the width were measured via callipers three times a week. Measurements were taken in two dimensions rather than three as this was the method that the

staff taking the measurements were most familiar with. However, due to concerns regarding the accuracy of estimating the volume with only two dimensions as that method assumes that the tumours are spheroids, which often inaccurate for subcutaneous tumours (Delgado-SanMartin et al, 2019) and to maintain consistency with the method used for our GEMM tumours the longest length was used in calculations.

5.2.6 Mice

Allograft Experiment 1

Female *NOD.Cg-Prkdcscid Il2rgtm1Wjl/SzJ* (NSG) mice (n = 12) were used for this experiment with 4 mice assigned to each of T25, T19b and T13. After implantation, tumours were monitored via calliper measurement and visible inspection for signs of ulceration for 14 days prior to the initial ^{11}C-acetate PET scan.

Allograft Experiment 2

Female *NOD.Cg-Prkdcscid Il2rgtm1Wjl/SzJ* (NSG) mice (n = 18) were used for this experiment, with 6 mice being assigned to each of T125, T19b and T13. After implantation, tumours were monitored by measuring them with callipers three times a week and ensuring no ulcerations had occurred for 10 days, irradiated, and then monitored as before for a further 7 days prior to culling. These mice were originally intended to be PET scanned to monitor radiotherapy response but due to ongoing technical issues at the PET centre this was not possible.

5.2.7 Imaging Protocol

Allograft Experiment 1

<u>PET/MRI protocol</u>

Mice received two ^{11}C-acetate PET scans on a NanoScan PET/MRI (Mediso, Hungary) on day 14 three days prior to radiotherapy and on day 17 immediately after radiotherapy. These timepoints were chosen based on the growth trajectory of the subcutaneous tumours; tumours were irradiated when they had a length of greater than 10mm, which all the tumours were expected to reach by 14 days based on early monitoring of the tumour length. The tumours all reached the desired length faster than anticipated (at 10 days), which informed Allograft

Experiment 2. The three-day gap between imaging and radiotherapy was to allow the mouse to recover, and the mouse was imaged and culled within two hours after the radiotherapy because we wanted to capture early, day one changes in metabolism and had to do this as a terminal procedure under the same anaesthetic (and within 4 hours) to avoid breaching license conditions. Prior to each imaging session a 1 ml volume of ^{11}C-acetate with an activity of 10 GBq was ordered from the West of Scotland PET Centre at Gartnavel General Hospital and was delivered on the morning of the experiment. Approximately 300 - 350 MBq of ^{11}C-acetate was injected via tail vein injection into anaesthetised mice. T1-weighted GRE MRI images with an echo time (TE) of 3.8 ms and a repetition time (TR) of 22.5 ms were acquired both to provide attenuation correction for the PET scan and for anatomical context to ensure accurate tumour delineation. 80 minutes after injection, at which point the activity will have decayed to approximately 15 – 20 MBq, a static 20-minute PET scan was acquired and reconstructed using native Mediso software (Nucline). The energy window of the scan's reconstruction was 400-600keV. The reconstructed PET images were transferred to Vivoquant for co-registration and analysis. The experimental timeline is summarised in Figure 32.

Cone Beam CT Protocol

Prior to treatment mice were scanned with the SARRP's onboard cone beam CT, with 1440 projections at 60 kVp and 0.8 mA using the fine focal spot (1 mm) being taken. The Feldkamp, Davis, and Kress CBCT algorithm (Feldkamp, Davis & Kress, 1984) was used for reconstruction of CT images.

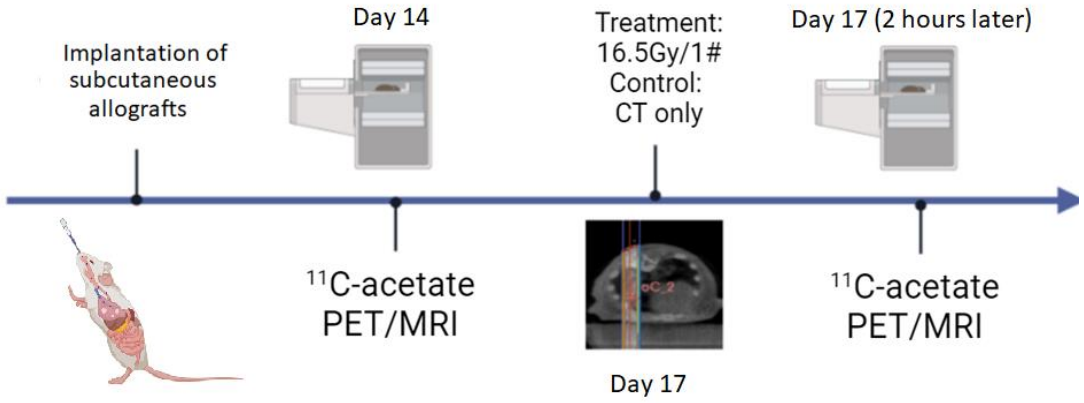

Figure 32. Experimental timeline for Allograft Experiment 1.

The timeline begins with the implantation of subcutaneous allografts into the mice. Subcutaneous tumours are measured 3 times a week to ensure that tumour does not exceed allowed dimensions and to ensure that tumours are big enough to be scanned. On day 14 post-implantation, the mice receive an 11C-acetate PET/MRI scan. Three days post PET/MRI, the treatment group receives 16.5 Gy/1#, while the control group is sham irradiated (only receives a CT scan). The mice are also measured with callipers on this day to define the pretreatment length. Another ^{11}C-acetate PET/MRI is performed, and the allografts are measured using callipers to assess the treatment response.

Allograft Experiment 2

These mice did not receive a PET/MRI scan due to an ongoing technical fault at the PET centre that lasted throughout this experiment. The Cone Beam CT protocol for these mice was the same as for Allograft Experiment 1 and the experimental timeline is summarised in Figure 33.

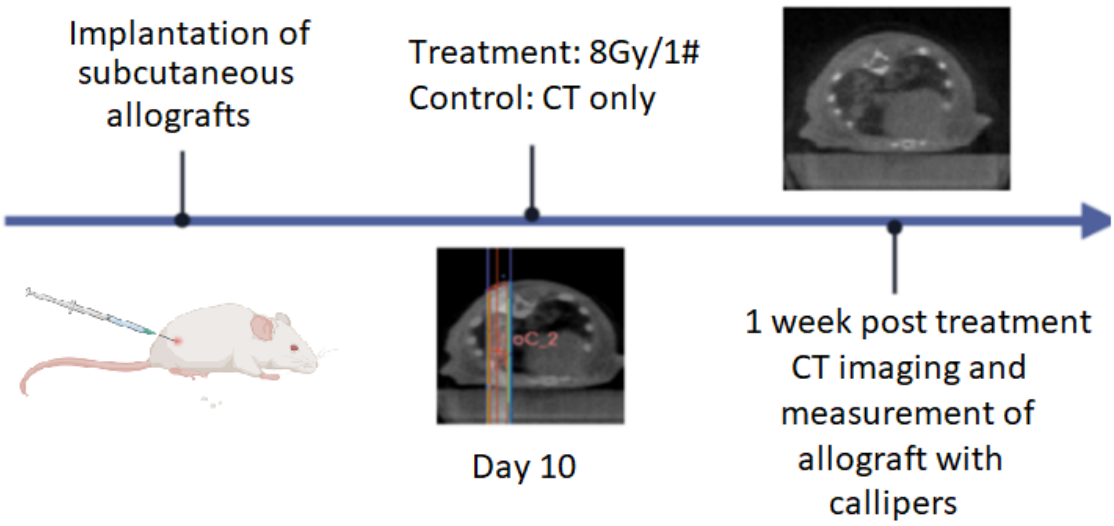

Figure 33. Experimental timeline for Allograft Experiment 2.

Allograft Experiment 2 is an experiment looking at the relationship between cell-line of origin and growth. The timeline begins with the implantation of subcutaneous allografts into the mice. On day 10 post-implantation, the treatment group receives with 8 Gy/1#, while the control group is sham irradiation (only receives a CT scan). One-week post-treatment, CT imaging is performed again, and the allografts are measured using callipers to assess the treatment response. The images included in the figure illustrate the key stages of the experiment: the implantation process, the CT imaging on day 10, and the post-treatment imaging and measurement.

5.2.8 Irradiation Protocol

Allograft Experiment 1

The mice were irradiated at 17 days with 16.5 Gy/1# using the SARRP. A parallel opposed beam arrangement angled to accommodate the size and shape of the tumour was used to deliver the dose. In cases where the 10 x 10 mm collimator was not sufficient to cover the tumour, a motorised variable collimator was used to ensure full tumour coverage. These collimators can adapt their shape to different sized tumours, although in the SARRP they always retain a rectangular shape (unlike clinical multileaf collimators which can adapt their shape more flexibly).

Allograft Experiment 2

Mice were irradiated at 10 days using the same beam arrangement and protocol as described above but with a lower treatment dose. The dose for this experiment was dropped from 16.5 Gy/1# to 8Gy/1# as NSG mice are more

radiosensitive than most other non-SCID strains as it is homozygous mutant for the Prkdc^{scid} gene mutation which affects double strand break repair, something that had not been realised when originally selecting the strain for this experiment.

5.2.9 Culling and sample collection

Allograft Experiment 1

Mice were culled on day 17 using a schedule 1 method (cervical dislocation while still anaesthetised from the final PET scan). Subcutaneous tumours were excised postmortem, formalin fixed, transferred to ethanol after 24 hours and then embedded in paraffin to create FFPE blocks for sectioning and staining.

Allograft Experiment 2

Mice were culled on upon reaching endpoint using a schedule 1 method (cervical dislocation while still anaesthetised from the final PET scan). Subcutaneous tumours were excised postmortem, formalin fixed, transferred to ethanol after 24 hours and then embedded in paraffin to create FFPE blocks for sectioning and staining.

5.2.10 Image Analysis

Allograft Experiment 1

The PET and MRI images were co-registered on Vivoquant using the tracer accumulation in the bladder and the heart as landmarks. Tumour delineation relied entirely on the anatomical information provided by the MRI as the ^{11}C-acetate uptake was relatively low, making it impossible to use the functional information provided by the PET scan to inform the creation of the ROIs. Tracer uptake is extracted from the ROI the SUV is calculated in accordance with the following formula in Equation 3:

$$SUVmax = \frac{Activity\ Concentration\ at\ Hottest\ Pixel\ (\frac{MBq}{g})}{(injected\ activity(MBq)/mass(g))}$$

Equation 3: Formula for the calculation of SUVMax

5.3 Results

5.3.1 Allograft Experiment 1

The ^{11}C-acetate SUVMax on the PET scan taken on Day 14 was compared to the ^{11}C-acetate SUVMax PET scan taken on Day 17 in Figure 34. Pre-treatment and post-treatment comparisons within each tumour type reveal variations in acetate uptake, with T25 showing an increase post-treatment (Pre-treatment SD = 0.234, Post-treatment SD = 0.391), T19b remaining relatively stable (Pre-treatment SD = 0.259, Post-treatment SD = 0.313), and T13 exhibiting a slight increase (Pre-treatment SD = 0.244, Post-treatment SD = 0.337). These data suggest differential responses to treatment among the tumour types, although this is not definitive due to the low sample size (N=8).

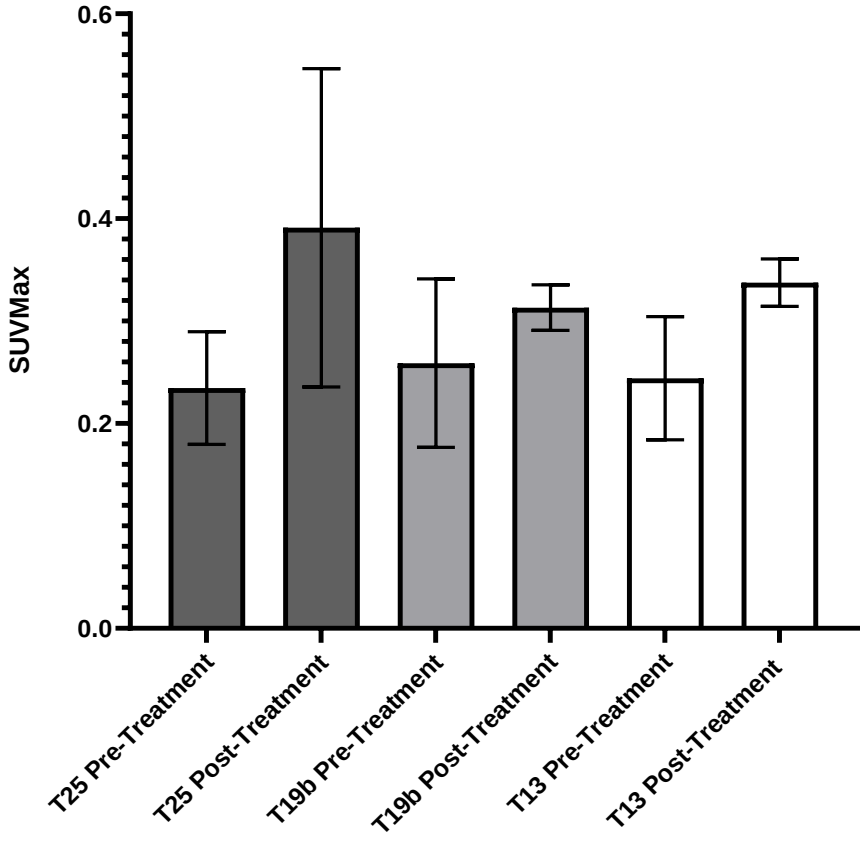

Figure 34. Maximum Standardized Uptake Values (SUVMax) of 11C-acetate in subcutaneous tumours pre- and post-treatment.

The bars represent the mean SUVMax for each treatment group with error bars indicating standard deviation. Tumours T25, T19b, and T13 were analysed before (Day 14) and approximately 2 hours after (Day 17) treatment.

Table 2 is an Analysis of Variance (ANOVA) table for the data presented in Figure 34. The results indicate that the treatment group has a significant effect on the change in ^{11}C-acetate SUVMax ($p = 0.0379$), while the cell line and the interaction between treatment group and cell line do not have significant effects ($p > 0.05$).

ANOVA table	SS	DF	MS	F (DFn, DFd)	P value
Row Factor x Column Factor	0.007967	2	0.003983	F (2, 5) = 0.7903	P=0.5032
Row Factor (treatment group)	0.03961	1	0.03961	F (1, 5) = 7.858	P=0.0379
Column Factor (cell line)	0.002367	2	0.001183	F (2, 5) = 0.1236	P=0.8863
Subject	0.04786	5	0.009571	F (5, 5) = 1.899	P=0.2493
Residual	0.0252	5	0.005041		

Table 2: Analysis of Variance (ANOVA) table for the change in ^{11}C-acetate SUVMax pre- and post-treatment in subcutaneous allografts.

Figure 35 shows typical mice from each of the cohorts for each cell line T25, T19b and T13. Pre-treatment SUVMax values are 0.25 for A1, 0.23 for B1, and 0.22 for C1, while post-treatment SUVMax values are 0.30 for A2, 0.33 for B2, and 0.32 for C2. The colour bar on the left indicates the range of SUVMax values from 0.2 to 1.2. These images show that, bar outliers, the uptake in the tumours does not differ noticeably from background.

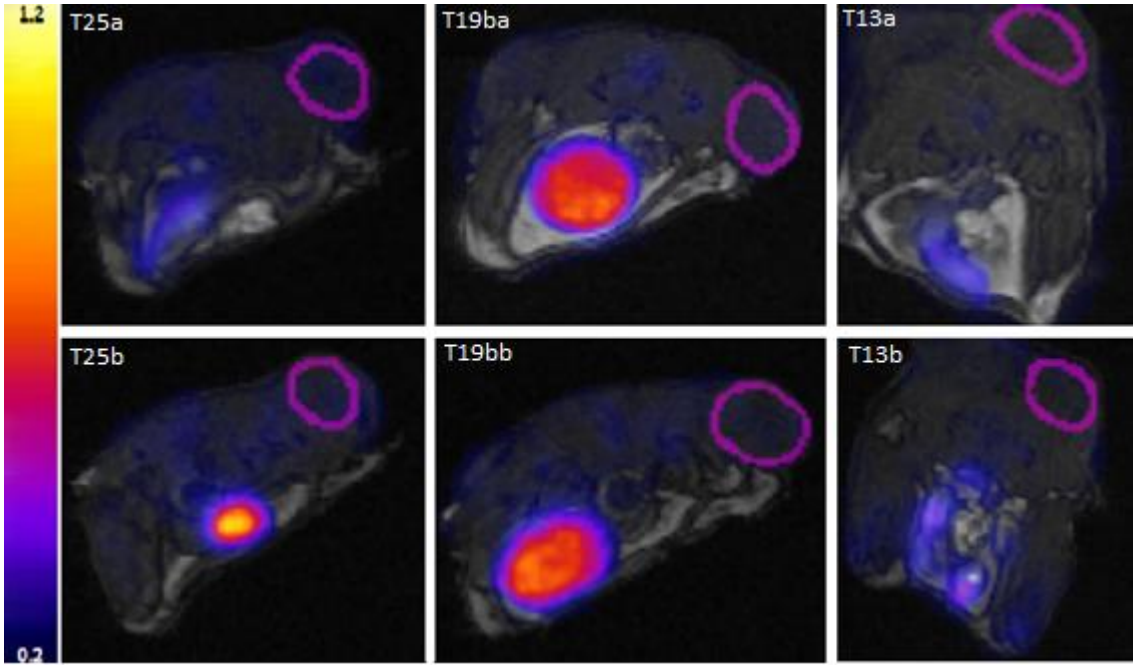

Figure 35. ^{11}C-Acetate PET/MRI scans of mice with subcutaneous tumours from different cell lines are displayed in panels A, B, and C.

Each column represents a cell line (from left, T25, T19b and T13). The first row includes pre-treatment scans (labelled "a"), and the second row includes post-treatment scans (labelled "b"). Pre-treatment SUVMax values are 0.25 for A1, 0.23 for B1, and 0.22 for C1, while post-treatment SUVMax values are 0.30 for A2, 0.33 for B2, and 0.32 for C2. The colour bar on the left indicates the range of SUVMax values from 0.2 to 1.2.

5.3.2 Allograft Experiment 2

Figure 36 shows the data from Allograft Experiment 2. The relationship between cell line (T13, T19b and T25) and post-treatment growth was assessed using paired T tests. Measurements taken on days 10 and 17 as standard but measurements normalised to 'per day' to align with the GEMM mice as there were delays with measuring some of their tumours via CT on certain weeks due to machine malfunction, making direct comparisons easier when considered on a 'per day' basis. Statistically significant differences in the length of the longest diameter pre- and post-treatment were observed in the control and treatment groups for cell lines T19b ($p = 0.0142$) and T13 ($p = 0.0078$), indicating that the cell lines responded to the radiation. Cell line T25 did not show a statistically significant difference between the control and treatment groups ($p = 0.1398$).

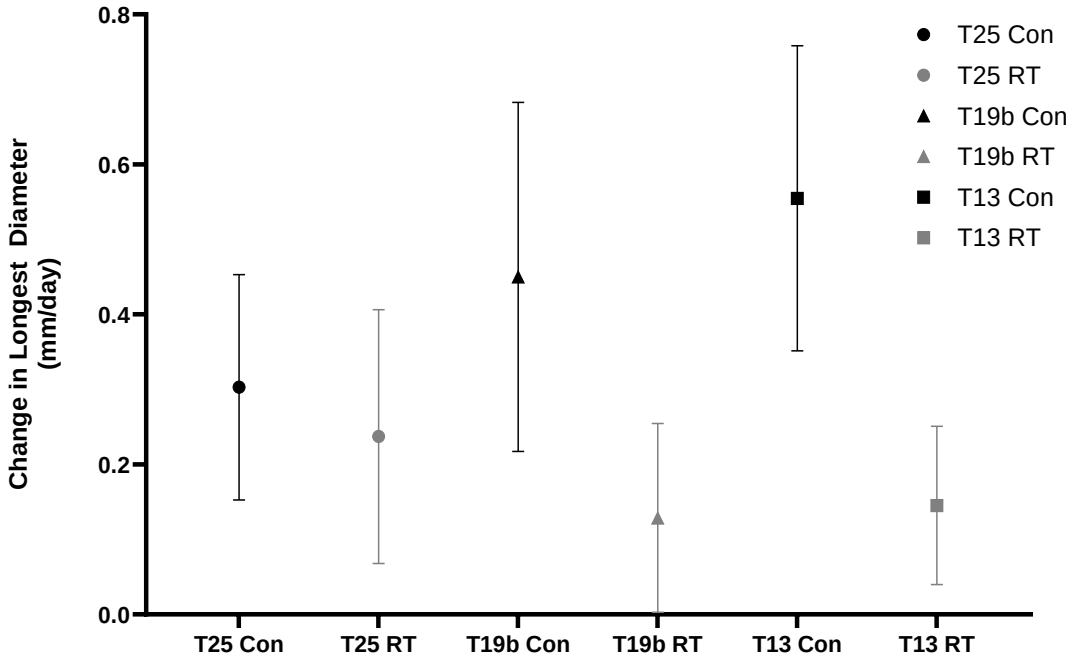

Figure 36. Change in the longest diameter of subcutaneous tumours (mm/day) in control (con) and radiotherapy treatment (RT) groups for cell lines T25, T19b, and T13.

The markers represent the mean change in the longest diameter, with error bars indicating standard deviation. Statistically significant differences in the length of the longest diameter pre- and post-treatment were observed in the control and treatment groups for cell lines T19b ($p = 0.0142$) and T13 ($p = 0.0078$). Cell line T25 did not show a statistically significant difference between the control and treatment groups ($p = 0.1398$). Paired t-tests were used to statistically analyse the data.

5.4 Discussion

5.4.1 Summary of Objectives

- Identify metabolically heterogeneous models of lung cancer that would provide the variability in 11C-acetate uptake necessary to determine an association between 11C-acetate uptake and radioresistance.

Figure 34 shows that the pre-and post-treatment SUVMax was barely distinguishable from background in most of the mice. A full analysis of the range in acetate uptake will be assessed by comparing pre-treatment ^{11}C-acetate SUVMax data from Allograft Experiment 1 to the GEMM control ^{11}C-acetate uptake data to determine which models have the highest variance in Chapter 6.

- Establish whether there is any change in ^{11}C-acetate acetate avidity post-radiotherapy

Table 2 analysing the data from Allograft Experiment 1 indicates that there is a significant difference in ^{11}C-acetate uptake between the pre- and post-treatment groups, but that the cell line and the interaction between treatment group and cell line do not have significant effects.

- Establish whether KP allografts have sufficiently varying radiotherapy treatment responses to be used to assess the relationship between fatty acid synthesis and radioresistance.

Figure 36 shows significant differences between the pre- and post-treatment groups of two of the cell lines (T19b and T13) but not the third (T25), indicating that there is a range of different radiotherapy responses across the cohort that is linked to cell line. However, given the low ^{11}C-acetate uptake shown across the cell lines in Figure 34.

5.4.2 Discussion

Metabolic Changes in Subcutaneous Allografts

Figure 34 and Table 2 illustrate how the ^{11}C-acetate SUVMax varies according to treatment group and cell line. One of the key findings from this table is that

little of the small variation in the pretreatment ^{11}C-acetate scans is attributable to the cell line. This is noteworthy given that in the characterisation of these GEMM cell lines in vitro, across several different experiments, T13 exhibited far higher ^{14}C-acetate uptake than either T19b or T25, while T19b's ^{14}C-acetate uptake was less than T13 but higher than T25 (Dzien, Bielik, and Lewis, 2017; 2018a; 2018b). Given that the ^{14}C-acetate uptake in these cell lines was consistently in this order across different experiments in 2017 and 2018, it seems likely that either an aspect of the cell culturing technique used or the change in the tumour microenvironment caused by the cells being implanted in the flank resulted in the observed metabolic change.

It is possible that the nutrient availability in the growth medium may have affected the type of cells that survived. Cells were cultured in basic DMEM supplemented with 10% FBS and 8 mM of glutamine. In vivo, less well-perfused tumours (and less well-perfused regions within the tumour) may have lower glucose levels (Vanhove et al., 2019), which in NSCLC can result in metabolic reprogramming of the tumour to ensure continued proliferation of the cancer cells (Li et al., 2022). As DMEM contains glucose that is more readily available to cells than it is in the blood vessels of the tumour (Bergers & Benjamin, 2003), it is possible that this may affect the metabolic profile of the cells, either through metabolic reprogramming or by favouring glucose-avid cells, allowing them to proliferate more readily. A dual tracer study with ^{11}C-acetate and ^{18}F-FDG could probe these potential metabolic changes in vivo, as if this hypothesis is correct, it would be expected that the ^{18}F-FDG uptake in these tumours would be higher than the ^{11}C-acetate uptake.

The use of a 50% Matrigel/50% PBS suspension for cells prior to implantation may also have influenced the metabolic profile of the tumour. Matrigel has been shown to impact the growth of subcutaneous tumours, increasing the number of tumours that grow after implantation and the rate at which they grow (Sweeney et al., 1991). Breast cancer cells grown in Matrigel cultures also increase their glucose uptake and subsequent lactate production relative to Collagen I and animal-derived tissue matrix gel (Ruud et al., 2020). While there does not seem to be a similar study examining this in NSCLC, it does indicate that Matrigel can affect tumour metabolism.

Alternatively, the effect of the differing tumour microenvironments could account for the changes. Subcutaneous tumours do not adequately recapitulate the tumour microenvironment of most cancer sites, and as NSCLC cells have the capacity to metabolically reprogramme themselves in response to changes in their environment (Eltayeb et al., 2022), this could result in differing metabolic phenotypes depending on the site of implantation rather than reflecting the characteristics of the original tumour from which the cell lines were derived. The claim that subcutaneous tumours are often reflective of the site they were implanted in rather than their site of origin is further supported by the fact that subcutaneous tumours display differing characteristics depending on their injection site on the body. For example, tumours implanted into the feet of mice exhibit a more aggressive phenotype and higher metastatic potential than subcutaneous flank allografts due to differences in immune response at each site (Speroni et al., 2009).

Relationship between Cell Line and Radiation-Induced Response in SUVMax

Figure 34 and Table 2 also demonstrate the degree to which the variation in ^{11}C-acetate SUVMax of the KP allografts depends on the treatment group, with the pre-treatment SUVMax across all cell lines differing from the post-treatment SUVMax, with T25 showing the greatest mean increase in SUVMax. If pretreatment ^{11}C-acetate uptake is correlated with treatment resistance, as hypothesised in this thesis, then it is also possible that an increase in ^{11}C-acetate uptake post-irradiation could result in increased resistance to subsequent fractions of radiotherapy. Additionally, uptake of ^{11}C-acetate could correspond with radioresistance as fatty acid synthesis is one of the metabolic pathways necessary for the production of substrates needed to repair DNA damage (Yu et al., 2023). While it was not possible to study this in the GEMM model as mice struggled to survive pre- and post-radiotherapy scans due to the high tumour burden in their lungs, if there is merit to this hypothesis then in the second allograft experiment the T25 group should have shown increased radioresistance relative to T19b and T13.

However, as shown in Figure 35, in most of the mice the ^{11}C-acetate SUVMax barely registered above background; the difference between the treated and untreated groups was largely driven by one outlier in the T25 group which had a pretreatment SUVMax of 0.227 and a post-treatment SUVMax of 0.571. As a result, no firm conclusions can be drawn from these data until a larger, adequately powered experiment using a more relevant model is performed.

Growth Kinetics of Subcutaneous Tumours and Treatment Response

Figure 36 shows that among the subcutaneous tumours derived from the three KP cell lines, T13, T19b, and T25, both T19b and T13 had a statistically significant difference between their irradiated and control groups. However, the T25 allografts did not show a statistically significant difference between the control and treatment groups. This suggests that T25 is potentially more radioresistant than T19b and T13, which could indicate that the change in ^{11}C-acetate uptake post-irradiation may be predictive of radioresistance if it was assumed that the findings in the first Allograft Experiment are generalisable to the cell lines in the second.

However, because this finding was observed in the subcutaneous model rather than the more clinically relevant GEMM model and the sample size in Allograft Experiment 1 was very small, caution should be exercised when interpreting the results. The fact that subcutaneous allografts and xenografts lack the inflammatory responses (Tan et al., 2021) and immune microenvironment (Horton et al., 2021) of orthotopic or GEMM models can result in therapies being far more effective on subcutaneous tumours than on tumours in the lung. It is further complicated by the fact that the data indicating that T25 may have a greater increase in post-treatment acetate avidity is largely skewed by one T25 mouse with a pretreatment SUVMax of 0.227 and a post-treatment SUVMax was 0.571. Given the sample size and the uncertainties associated with the model, these findings would require further investigation using adequately powered, more clinically relevant models such as a GEMM or orthotopic models.

5.4.3 Limitations

When planning the experiment, suspension in Matrigel was chosen specifically because slow growing tumours can be induced to grow faster by its presence (Sweeney et al., 1991). From this perspective, it was very effective; across the two experiments, all implanted subcutaneous tumours grew to a measurable volume within two weeks. In retrospect, given that the full effects of Matrigel on metabolism in NSCLC are not fully understood, it would be recommended to suspend the cells in 100% PBS instead, even if that resulted in fewer allografts growing and a slower experiment. The use of an acetate-spiked growth media during the cell culture stage may also be prudent.

Another limitation that arose from the desire to maximise tumour growth was the potential confounding factors associated with the use of *NOD.Cg-Prkdcscid Il2rgtm1Wjl/SzJ* (NSG) mice. These mice were chosen specifically because their immunocompromised state would ensure adequate tumour growth. However, the fact that NSG mice are more radiosensitive than most other non-SCID strains as this strain is homozygous mutant for the *Prkdcscid* gene mutation which affects double strand break repair was overlooked, which could potentially have compromised the results of Allograft Experiment 2 as these mice were irradiated and kept alive for a week post radiotherapy to monitor growth of their subcutaneous implants. This oversight directly led to the necessary exclusion of supporting weight data for this experiment as it was compromised by the radiosensitivity of the mice. If this experiment were to be run again with a subcutaneous model, an immunocompetent model would be chosen to make the model more clinically relevant and avoid the issues associated with the radiosensitivity of the NSG mice.

To determine the degree to which tumour metabolism and treatment response were affected by the tumour microenvironment, cells could be administered via tail vein injection to create an orthotopic model of NSCLC. If these cells respond less strongly to radiation than the subcutaneous allografts and have ^{11}C-acetate uptakes that resemble the characterisation of the cell lines in vitro, this could indicate that the tumour microenvironment was partially responsible for the metabolic shifts. If the model works, it may provide a useful compromise

between the speed, practicality, and statistical power that the higher throughput subcutaneous allografts offer and the clinical relevance of the GEMMs.

To confirm the hypothesis that a higher increase in ^{11}C-acetate uptake post-radiotherapy is indicative of radioresistance, an ^{11}C-acetate PET radiotherapy treatment response study similar to that originally planned for the second allograft experiment could be initiated with GEMM models (or orthotopic models if the tail vein injection method proved viable).

6. ^{11}C-ACETATE POSITRON EMISSION TOMOGRAPHY IN GENETICALLY ENGINEERED MOUSE MODELS OF LUNG CANCER

6.1 Introduction

6.1.1 Background

In this chapter, the relationship between the change in tumour size post irradiation and the ^{11}C-acetate PET SUVMax will be explored using both subcutaneous and GEMM models of NSCLC, comparing subcutaneous xenograft data presented in chapter 5 with newly presented GEMM data. There is a growing body of papers discussing irradiation of GEMM mice, including studies exploring the radiosensitivity of specific GEMM models (Herter-Sprie et al, 2014) and therapeutic irradiation in the abdomen (Schmidt et al, 2021). While ^{11}C-acetate PET imaging of GEMM models of NSCLC has been performed before (Lewis et al, 2014), combining this imaging modality with a follow up study on the effect of irradiation on change in tumour longest length is novel, especially in the lung as there are additional challenges that arise from respiratory motion, which explains the importance given in this work to the establishment of appropriate beam arrangements and margins(cf. Chapters 2 and 3).

Two GEMM genotypes, *Kras$^{G12D/+}$ p53$^{-/-}$* (KP) GEMMs and *LSL-Kras$^{G12D/+}$ Rosa26-LSL-Myc* (KMyc) adenocarcinoma mouse models were chosen as this is the most common form of NSCLC and adenocarcinoma's intertumour response to radiation varies significantly (Carmichael et al, 1989). KMyc was selected because ^{11}C-acetate PET uptake experiments on this GEMM model by members of the lab have indicated that there is high intertumour heterogeneity in ^{11}C-acetate metabolism, and the Myc gene has been found to regulate fatty acid synthesis at other sites (Singh et al, 2021), although this hasn't been confirmed for NSCLC yet. The KP model was selected because of its noted radio-resistance relative to other GEMM models (Herter-Sprie et al, 2014).

6.1.2 Objectives and Analysis

- Identify metabolically heterogeneous models of lung cancer that would provide the variability in ^{11}C-acetate uptake necessary to determine an association between ^{11}C-acetate uptake and radioresistance.

The data for ^{11}C-acetate uptake from Allograft Experiment 1 in Chapter 5, the KP GEMM and the KMyc GEMM were plotted alongside one another, and their standard deviations compared.

- Establish whether KMyc GEMMs or KP GEMMs or KP allografts have sufficiently varying radiotherapy treatment responses to be used to assess the relationship between fatty acid synthesis and radioresistance.

Changes in longest diameter length were compared to assess the treatment response of the tumours in the models that had sufficient ^{11}C-acetate avidity. Longest diameter was calculated after segmentation using the oriented bounding box feature in 3D Slicer, a method which has been utilized as a more reproducible alternative to visual assessment for over a decade (Preim & Botha, 2014). A Mann-Whitney test was performed to assess whether there is a statistically significant difference in pre- and post-treatment growth rate. The change in longest length was used rather than volume as measurement errors can be compounded when using volume rather than length in very small tumours, and to maintain consistency with the subcutaneous allografts.

- Using any models that have both varied radiosensitivity and a range of acetate avidities, calculate whether there is a relationship between pretreatment growth rate and radioresistance.

A simple linear regression between the SUVMax and the post treatment growth rate was performed to assess whether there is a correlation between the acetate uptake and the treatment response of the tumour. This was compared to controls to determine if any correlation is related to the radiotherapy response.

- Ensure that any established correlation cannot be explained by factors that are known to contribute to radioresistance.

This was resolved in two ways. First, as pretreatment size is a recognised prognostic marker, we established whether there is a correlation between the

SUVMax and the pretreatment tumour size by performing a simple linear regression. Second, by establishing whether there is a statistically significant correlation between FASN, a surrogate for ^{11}C-acetate avidity, and GLUT1 staining, a surrogate for ^{18}F-FDG avidity, in a sample of the GEMM tumours. The rationale for this is that if the tumours are both ^{11}C-acetate and ^{18}F-FDG avid, ^{18}F-FDG imaging would be more practical and efficient as it is already well established in the clinic.

6.2 Materials and Methods

6.2.1 Mice

Mice were induced between 8 and 15 weeks using AdenoCre inhalation after being anesthetized with isoflurane in oxygen. A mix of male and female mice were used. These mice were induced low titres (5×10^4 – 5×10^5 PFU/ml) to ensure large, isolated tumours suitable for individual targeting.

The following criteria had to be met for mice to be recruited onto the ^{11}C-acetate PET study once the presence of tumours had been established via imaging:

- At least two tumours with diameters >1 mm should be visible on CT.
- Mice cannot have lost more than 10% of their body weight or be hunched/ inactive as there is a post PET follow-up period of at least 10 days and mice that are already declining will be unlikely to survive.
- Mice that struggle to recover after scruffing cannot be recruited as the protocol requires extended anaesthesia, which could cause unnecessary suffering in mice experiencing symptoms of respiratory distress.
- No large areas of inflammation or collapsed lung on the CT both for the welfare of the mouse and because it complicates post treatment monitoring of the tumours.
- Tumours that are pressed against the rib cage or diaphragm to the extent that differentiating them from the surrounding tissue becomes difficult in the treatment day or follow up scans cannot be counted due to the potential for errors in measurement.

25 KP and 21 KMyc mice were induced in total, with the number induced limited by availability of the mice. In total 6 KP and 6 KMyc mice had tumours that were analysed in the final experiment. Flowcharts showing causes of losses in the cohort can be found in Figures 37 and 38.

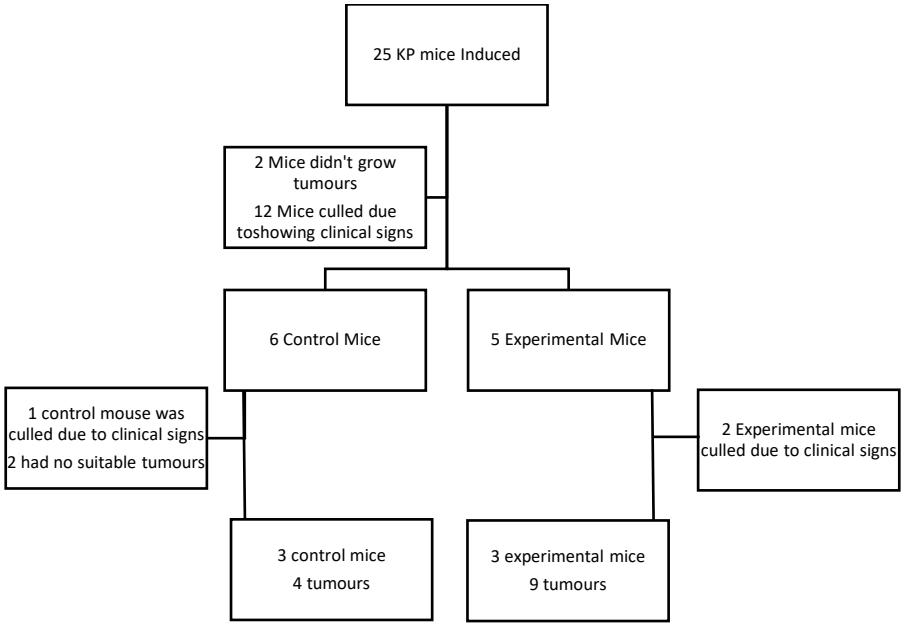

Figure 37. Flowchart showing causes of losses in the KP cohort of the ^{11}C-acetate PET GEMM experiment.

25 KP mice were recruited and 6 survived until endpoint. This indicates that a cohort at least 4.2 times the desired sample size should be used for similar experiments in the future.

Figure 38. Flowchart showing causes of losses in the KMyc cohort of the ^{11}C-acetate PET GEMM experiment.

21 KMyc mice were recruited and 6 survived until endpoint. This indicates that a cohort at least 3.5 times the desired sample size should be used for similar experiments in the future.

6.2.2 Cone Beam CT protocol

Prior to treatment mice were scanned monthly with the SARRP's onboard cone beam CT, with 1440 projections at 60 kVp and 0.8 mA using the fine focal spot (1 mm) being taken. The Feldkamp, Davis, and Kress CBCT algorithm (Feldkamp, Davis & Kress, 1984) was used for reconstruction of CT images. Tumour size and adverse effects on normal lung tissue such as inflammation or collapsed lobes were recorded.

6.2.3 MRI Protocol

The imaging protocol for the GEMMs is the same as that described in section 5.1.2: Allograft experiment 1 (TE=3.8 ms, TR=22.5 ms), with T1-weighted GRE MRI preset adapted to the lungs.

6.2.4 Irradiation Protocol

In the KP model each tumour was irradiated with 16.5 Gy/1# with a margin of at least 1 mm using a parallel opposed beam arrangement. This arrangement was chosen because of findings in Chapter 3, where γH2AX staining was used to show that a 1mm margin was sufficient to cover the tumour while using a parallel opposed beam arrangement. When tumours were clustered closely together, a single beam was used for to avoid the potential for two overlapping fields. When this method was employed, the dose distribution across each tumour was visually assessed to ensure acceptable coverage.

It proved more challenging to administer targeted radiation to the KMyc model. This is because the tumours in this model tend towards being smaller and closer together, often appearing in very close proximity to each other even when induced at lower titres. As a result, it was deemed necessary to perform whole lung irradiation on these mice rather than the targeted radiation that had been planned. While some of the mice had tumours that were distinct and large enough for individual irradiation it was deemed more important to ensure that a consistent protocol was applied across the cohort.

6.2.5 Image Analysis

The image analysis protocol for the GEMMs is the same as that described in section 5.1.2 for the allografts.

6.2.6 Sample Collection

Mice were culled after their final CT scan culled using a schedule 1 method (CO_2 inhalation), lungs were extracted, put into cassettes to ensure that the orientation was clear for identification of tumours later as they need to be cross referenced with our scans, formalin fixed for 24 hours and transferred to ethanol prior to being embedded in paraffin blocks for analysis.

6.2.7 Staining

Sections for fatty acid synthase (FASN) staining (3180, Cell Signalling) were stained on an Agilent AutostainerLink48. Sections were loaded into an Agilent pre-treatment module to be dewaxed and undergo heat induced epitope retrieval (HIER) using a high target retrieval solution (TRS) where sections were heated to 97°C for 20 minutes. After HIER sections were washed thoroughly with flex wash buffer (K8007, Agilent) prior to being loaded onto the Agilent Autostainer link48. The sections underwent peroxidase blocking (S2023, Agilent) for 5 minutes and rinsed with flex buffer. FASN antibody staining was at 1/300 dilution for 30 minutes. Following staining sections were rinsed with flex buffer before application of rabbit envision secondary antibody for 30 minutes. Flex buffer rinsing took place before applying Liquid DAB (K3468, Agilent) for 10 minutes. After staining sections were washed in tap water and counterstained with haematoxylin z (RBA-4201-00A, CellPath), washed in tap water, differentiated in 1% acid alcohol, washed and the nuclei were stained blue in scotts tap water substitute (in-house).

The following antibodies were stained on a Leica Bond Rx autostainer, αGlut-1 (G12-A, Alpha Diagnostics). All FFPE sections underwent on-board dewaxing

(AR9222, Leica) and epitope retrieval using ER2 solution (AR9640, Leica) at 95°C where sections for αGlut-1 were retrieved for 30 minutes. Sections were rinsed with Leica wash buffer (AR9590, Leica) before peroxidase block was performed using an Intense R kit (DS9263, Leica) for 5 minutes. Sections were rinsed with wash buffer before application of primary antibodies at an optimised dilution (αGlut-1, 1/250) for 30 minutes. Sections were rinsed with wash buffer, and all had rabbit envision secondary antibody (K4003, Agilent) applied for 30 minutes. Sections were rinsed with wash buffer and visualised using DAB in the Intense R kit.

To complete the IHC staining sections were rinsed in tap water, dehydrated through graded ethanol solutions and placed in xylene. A cover slip was placed over stained sections in xylene using DPX mountant (SEA-1300-00A, CellPath).

6.3 Results

Figure 39 shows tumours from the cohort of GEMM mice used in the experiments detailed in Figures 40 to 45. This figure shows 1 KP GEMM (G-I) and two KMyc GEMMs (A-C and D-F).

The SUVMax of A's outlined tumour is 0.314, meaning it has low acetate avidity. The tumour is clearly radiosensitive as it is one of the few tumours in the experiment that shrunk (had a decrease in longest length of nearly 4.464%/day between B and C, aligning with our theory that acetate uptake predicts radioresistance.)

The KMyc control mouse (D) had an SUVMax of 0.424 and a % increase in longest length of 2.85%/day between E and F. This is included as a contrast to the strong treatment response in the irradiated KMyc in A-C. The mouse G's tumour had the second highest SUVMax out of the treated KP GEMMs (0.751) and had an increase in longest length of 1.07% a day between H and I.

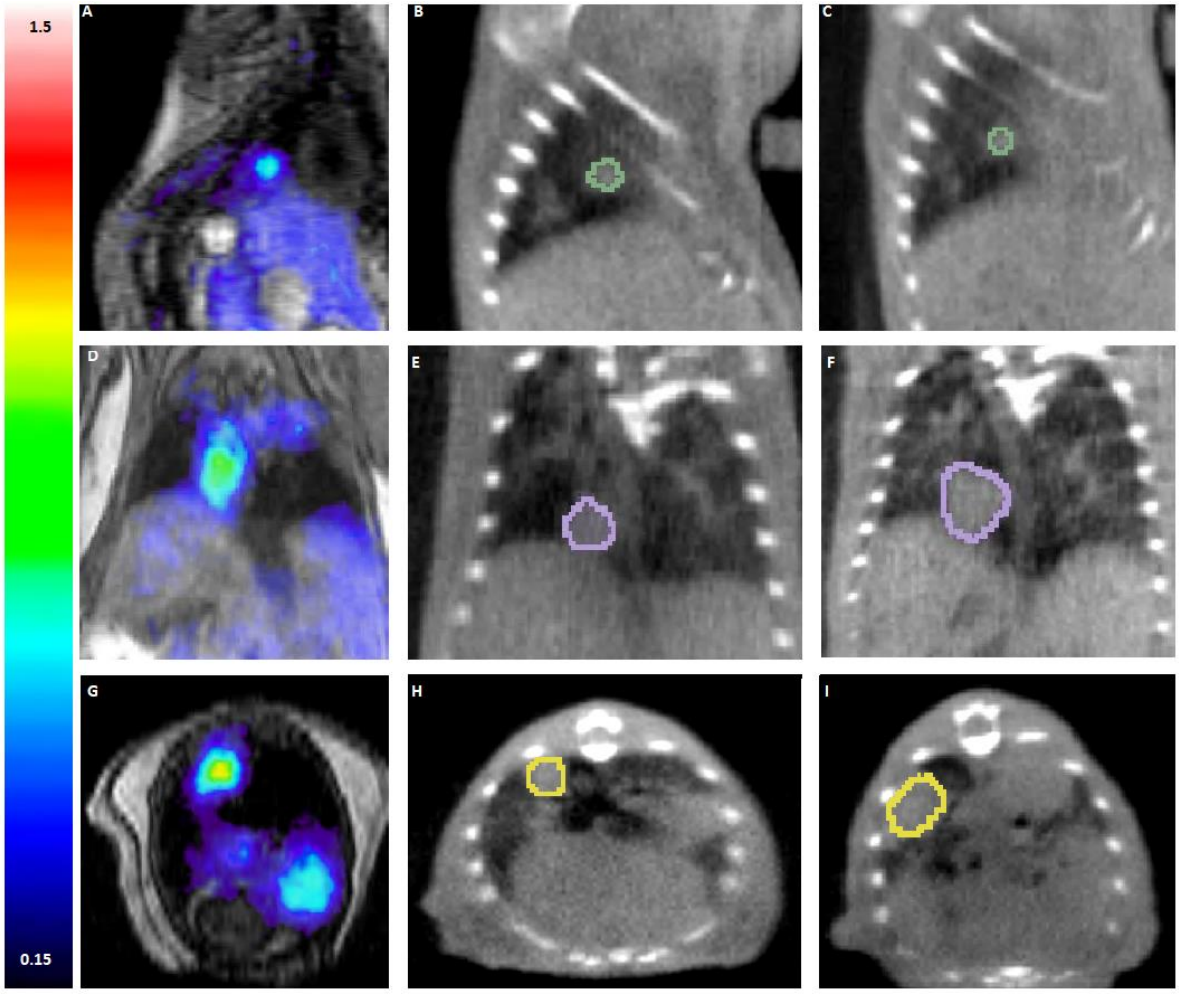

Figure 39. Comparison of ^{11}C-acetate SUVMax uptake (A, D and G) and subsequent change in tumour size after 1 week in 3 GEMM tumours including KMycs and KPs (N. KP= 1, N. KMyc=2).

A, D and G are ^{11}C-acetate PET scans and B, C, E, F, H and I are CT scans. Two of the mice have been irradiated (the KMyc in pictures A-C and the KP in G-I). A-C are images in the sagittal plane, D-F in the coronal and G-I in the axial plane.

Figure 40 compares ^{11}C-acetate SUVMax in subcutaneous KP derived allografts, KP GEMMs and KMyc GEMMs. The purpose of this analysis is to determine which models have the highest intertumour heterogeneity in ^{11}C-acetate SUVMax. This is because mice with a range of acetate avidities to test the hypothesis. This was determined by comparing the standard deviations of each model. The low variation in ^{11}C-acetate SUVMax in the subcutaneous allograft model makes it unsuitable for determining the relationship between baseline ^{11}C-acetate uptake and differential radiotherapy response. The difference between the KP allograft and the KP GEMM was expected given the fact that the allografts do not recapitulate the tumour microenvironment, although the scale of the difference was not anticipated.

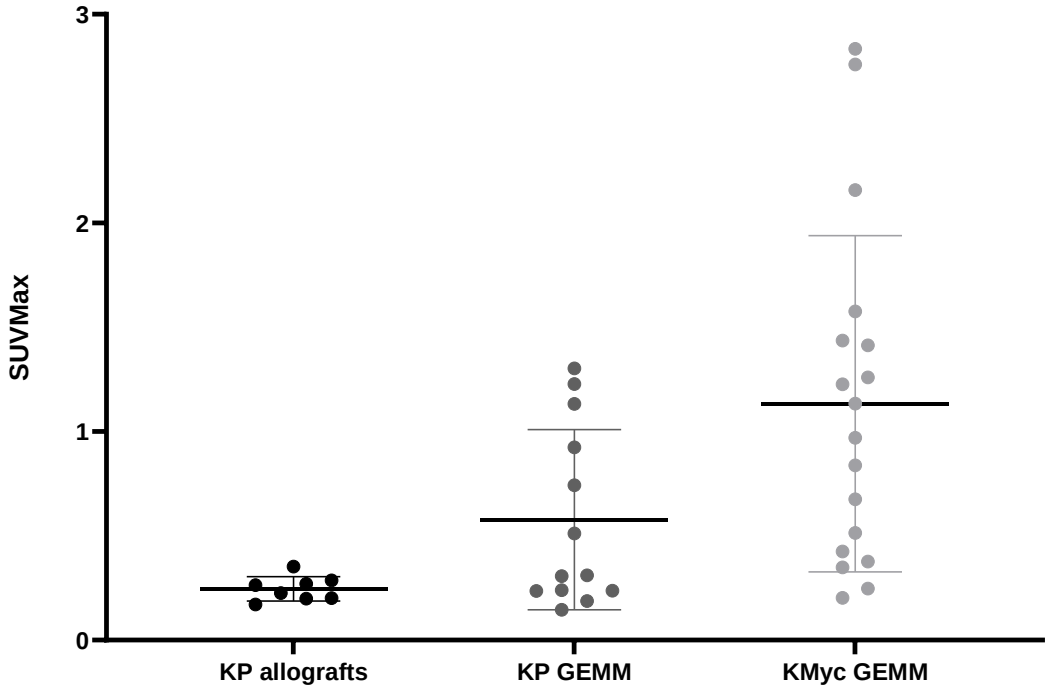

Figure 40. Comparison of ^{11}C-acetate SUVMax in subcutaneous KP derived allografts, KP GEMMs and KMyc GEMMs. (KP Allografts: n. mouse= 17, n. tumour=34, KP GEMM: n. mouse=6, n. tumour=13, KMyc GEMM: n. mouse=6, n. tumour=12)

Intertumour variation in ^{11}C-acetate SUVMax uptake is greater in KMyc GEMMs (s.d.=0.8055) than KP GEMMs (s.d.=0.4318) and subcutaneous KP allografts (s.d.=0.05870).

Figure 41 compares the post-treatment change in longest length in KMyc and KP mice treated with 16/1#. The purpose of this analysis was to determine whether radiotherapy affected the size of the tumours in any of the models. This was determined by measuring the change in longest length from the baseline scan to one week post irradiation, which was then subdivided into days for direct comparison as some of the endpoint scans were delayed by a day. The results of the Mann Whitney tests comparing the control and intervention groups shows that the KMyc GEMM model displays a greater slowing in change of longest length in response to radiation, while the KP GEMM displays greater radioresistance with no significant difference being found in the control and treatment groups. The KP allograft model was the most radiosensitive of the three models.

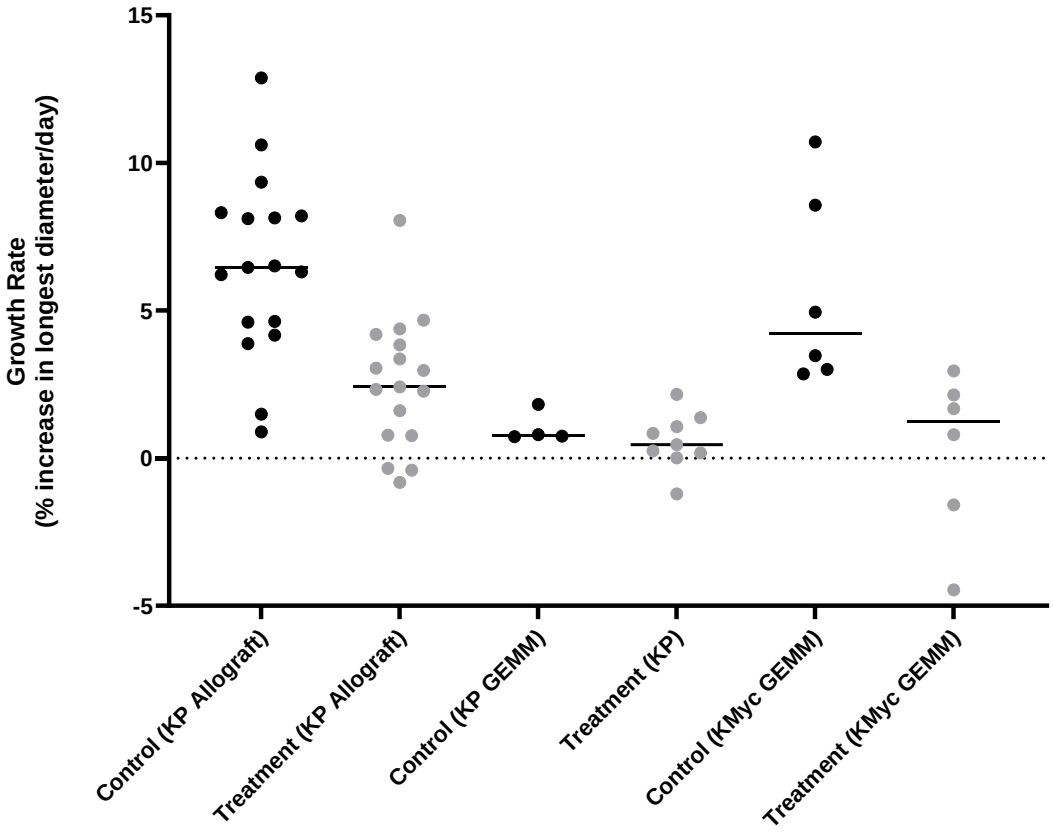

Figure 41. Comparison of post-treatment change in longest length in KMyc and KP mice treated with 16/1# (KP Allograft: n. mouse=17, n. tumour=34, KP GEMM: n. mouse=6, n. tumour=13, KMyc GEMM: n. mouse=6, n. tumour=12)

Radiotherapy has a statistically significant effect on the change in longest length of KP allografts (p=0.0002) and KMyc GEMM tumours (p=0.0043) but not on the change of longest length of KP GEMM tumours (p=0.5035).

Figure 42 shows simple linear regressions showing the relationship between the post-treatment change in longest length and the SUVMax in the KP group. The purpose of this analysis was to investigate whether there was a correlation between the change in longest length post treatment and the SUVMax of ^{11}C-acetate in the control and treated groups for the KP cohort. SUVMax of ^{11}C-acetate appears to be predictive of change in longest length in the KP treatment group but not in the control group. This suggests that the difference in response is in fact a response to the irradiation and not variation innate to the tumour.

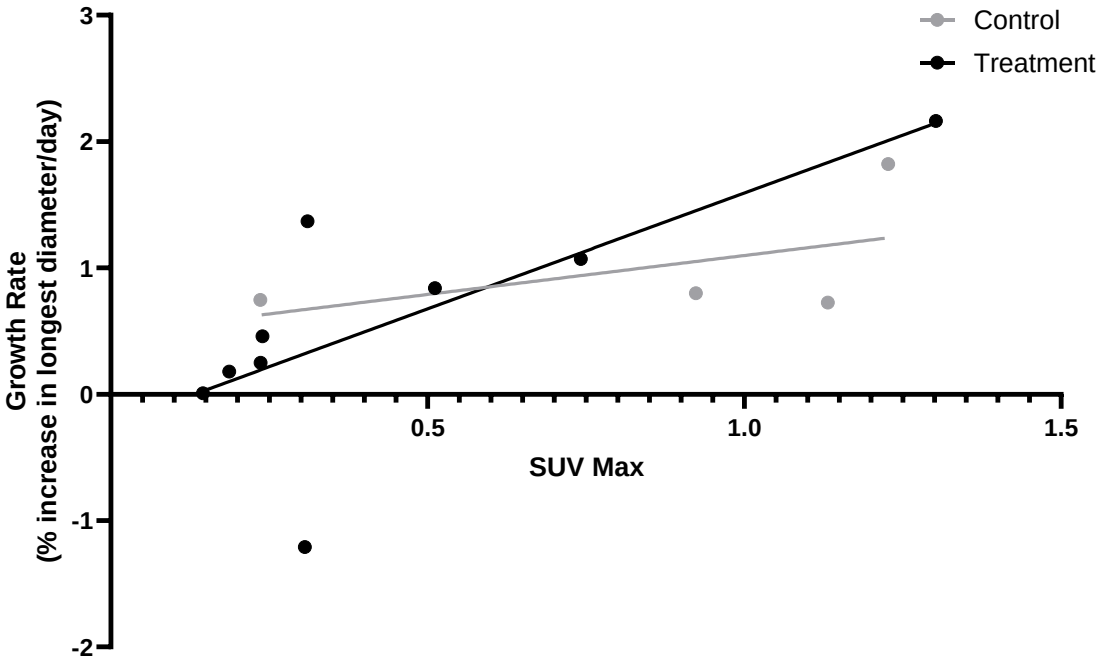

Figure 42. Simple linear regressions showing the relationship between the post-treatment change in longest length and the SUVMax in the KP group (N. mouse=6, N. tumour=12). SUVMax of ^{11}C-acetate is Predictive of Radiotherapy Response in the Irradiated KP Group (R2=0.6743, p=0.0298) but not the Control KP Group (R2= 0.2681, p=0.4822)

Figure 43 shows a simple linear regression analysis of the relationship between post-treatment change in longest length and ^{11}C-acetate SUVMax in control and treated groups. ^{11}C-acetate SUVMax predicts changes in longest length in the treatment group but not in the control group, suggesting that the observed differences in response could be due to a response to the radiotherapy rather than intrinsic tumour variation.

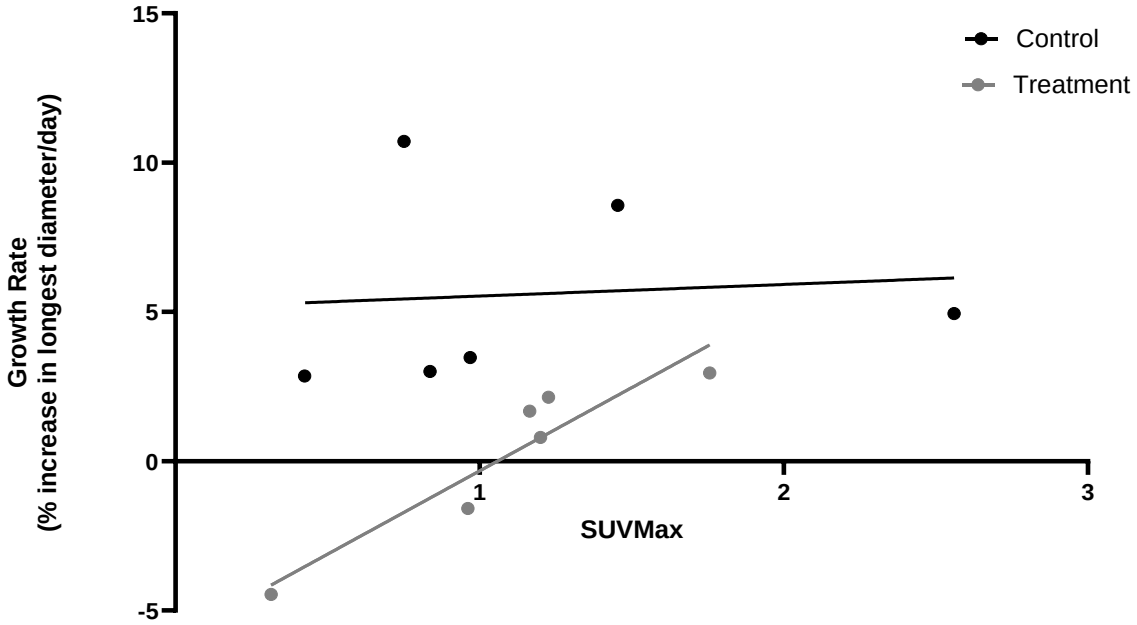

Figure 43. Simple linear regression analysis of the relationship between post-treatment change in longest length and ^{11}C-acetate SUVMax in control and treated groups (N. mouse=6, N. tumour=12) in the KMyc model.
This demonstrates that ^{11}C-acetate SUVMax is predictive of radioresistance as the SUVMax in the treatment group is correlated with the longest length (R^2=0.8786, p=0.0058) and but this is not the case with the control group (R^2=0.008072, p=0.8656).

Figure 44 explores whether there is a correlation between the SUVMax and the pretreatment tumour size by performing a simple linear regression. There was no statistically significant correlation between ^{11}C-acetate SUVMax and the pretreatment tumour size (R^2=0.1892, p=0.1576) in the KMyc model. This suggests that the SUVMax is not just a correlate of the pretreatment longest diameter but has independent predictive value.

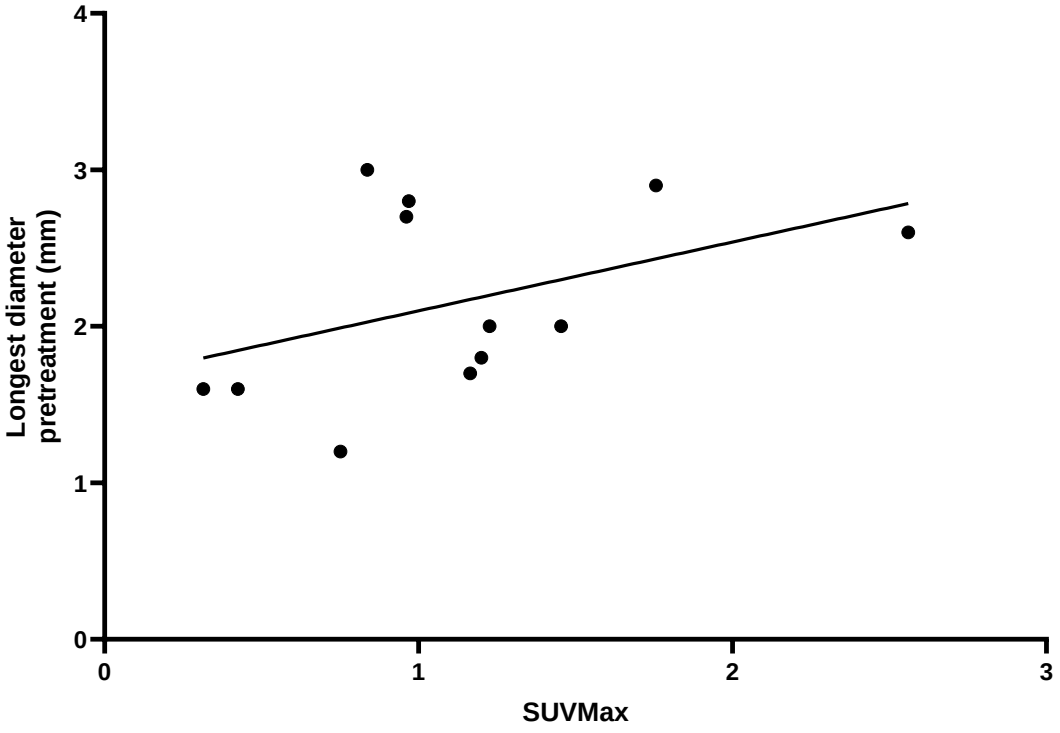

Figure 44. Simple linear regression analysis of the relationship between 11C-acetate uptake and pretreatment longest diameter in the KMyc model (N. mouse=6, N. tumour=12)

Graph showing that there is no statistically significant correlation between ^{11}C-acetate SUVMax and the pretreatment tumour size (R^2=0.1892, p=0.1576) in the KMyc model.

Figure 45 examines whether there is a statistically significant correlation between FASN, a surrogate for ^{11}C-acetate avidity, and GLUT1 staining, a surrogate for ^{18}F-FDG avidity, in a sample of the GEMM tumours. There was no statistically significant correlation between the percentage of FASN positive cells and GLUT1 positive cells (p=0.1540). The lack of a significant correlation between the GLUT1 and FASN expression indicates that the information gained from an ^{11}C-acetate scan could not be more easily obtained through an ^{18}F-FDG scan.

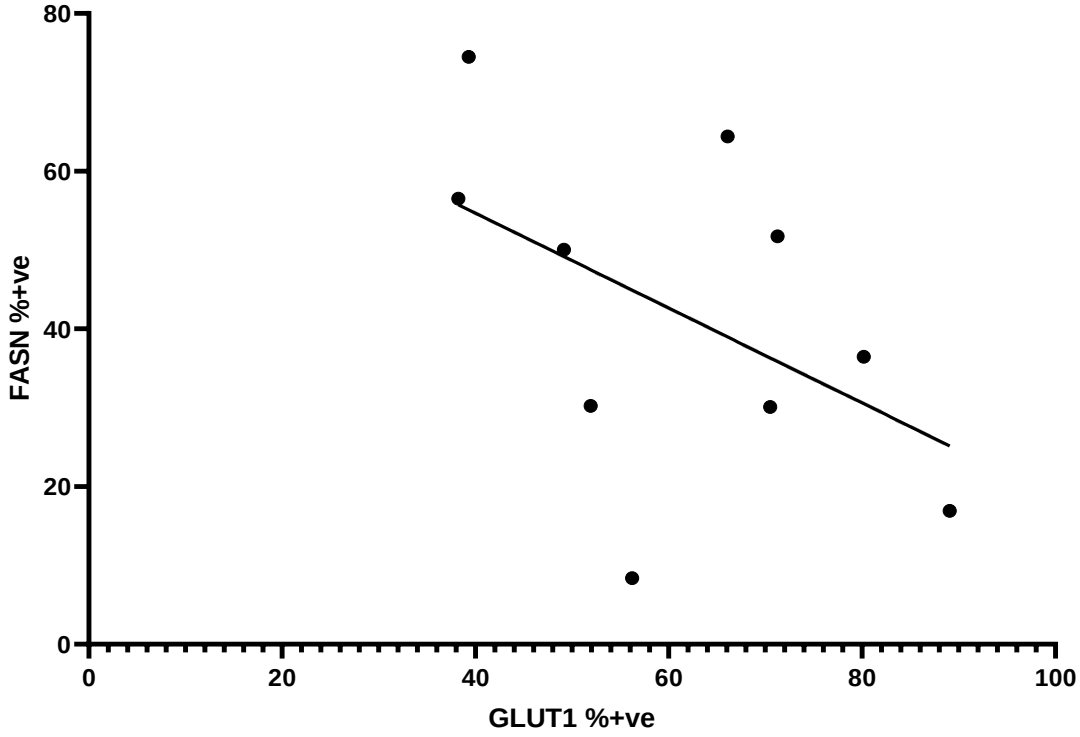

Figure 45. Analysis of the relationship between FASN and GLUT1 expression in a KP GEMM (N. mouse=1, N. tumour=10).

A simple linear regression shows that is no statistically significant correlation between the percentage of FASN positive cells and GLUT1 positive cells (p=0.1540).

6.4 Discussion

6.4.1 Summary of Objectives

- Identify metabolically heterogeneous models of lung cancer that would provide the variability in ^{11}C-acetate uptake necessary to determine an association between ^{11}C-acetate uptake and radioresistance.

The ^{11}C-acetate uptake for the KMyc GEMM had the largest standard deviations of the three models examined, as shown in Figure 40. Figure 39 also visually shows that the ^{11}C-acetate uptake in the GEMMs is greater than that shown in Figure 35 for the subcutaneous allografts.

- Establish whether KMyc GEMMs or KP GEMMs or KP allografts have sufficiently varying radiotherapy treatment responses to be used to assess the relationship between fatty acid synthesis and radioresistance.

Figure 41 and the accompanying Mann-Whitney test showed that of the two GEMM models only the KMyc model showed a statistically significant difference in pre- and post-treatment change in longest length.

- Using any models that have both varied radiosensitivity and a range of acetate avidities, calculate whether there is a relationship between change in longest length pre and post treatment and radioresistance.

The simple linear regressions in figures 42 and 43 showed that there was a correlation between the ^{11}C-acetate SUVMax and the post treatment change in longest length in both the KMyc and KP models. ^{11}C-acetate SUVMax was not correlated to change in longest length post sham-treatment in the control group of either cohort.

- Ensure that any established correlation cannot be explained by factors that are known to contribute to radioresistance.

Figure 44 showed that there was no correlation between the SUVMax and the pretreatment tumour size by performing a simple linear regression. Figure 45 showed that there was no statistically significant correlation between FASN, a surrogate for ^{11}C-acetate avidity, and GLUT1 staining, a surrogate for ^{18}F-FDG avidity, in a sample of the GEMM tumours.

6.4.2 Discussion

Of the three mouse models of lung cancer studied, the model with the highest intertumour variation in ^{11}C-acetate SUVMax was the KMyc GEMM, as can be seen in Figure 40. This aligns with observations that had been made by other members of the lab previously about KMyc tumours having both the highest variation in acetate uptake and having individual tumours with the highest SUVMax of the different GEMM models. One potential reason for this is that Myc appears to have a role in regulating fatty acid synthesis, something which has been demonstrated at multiple sites such as the prostate (Singh et al, 2020), the breast (Furuya et al, 2012) and, most importantly for this thesis, the lung (Hall et al, 2016). Myc has been associated with the expression of fatty acid synthase (FASN), acetyl-CoA synthetase enzyme (ACSS2) (Comerford et al, 2014) and acetyl-CoA carboxylase 1 and 2 (ACC) (Singh et al, 2020; Dong, Liu & Qing, 2020). All three of these enzymes have been successfully targeted for inhibition in NSCLC (Chang et al, 2019; Ni et al, 2020; Svensson et al, 2016); of these, inhibition of FASN has been considered for radiosensitization of lung tumours. (Zhan et al, 2018). As Myc appears so strongly associated with regulating fatty acid synthesis it makes sense that the KMyc tumours appear to have the highest capacity for ^{11}C-acetate uptake.

KP allografts had the highest variation in response to radiation and overall showed the biggest disparity between the treatment groups. However, as mentioned in the discussion of the subcutaneous allograft chapter, subcutaneous tumours often respond more strongly to treatments as their implantation site means that factors in the tumour environment that usually promote radioresistance are not present (Tan et al, 2021; Horton et al, 2021). This means that the usefulness of inter-model comparisons is limited.

The distinction between the KP GEMM radioresistance and the KP allograft's radiosensitivity further emphasizes this point; KP tumours are known to be radioresistant, even compared to other GEMM models (Herter-Sprie et al, 2014), which makes sense as KRAS and P53 mutations are known to be associated with poor prognoses (Gurtner et al, 2019). However, while the KP model did not show a statistically significant difference between the control and treatment groups in

terms of radiotherapy response alone, in Figure 40 the tracer uptake in the KP treated group had a statistically significant correlation with the post-irradiation change in longest length while the control group did not. While this is of limited value alone because of the lack of demonstrable radiotherapy response, it lends weight to the correlation noted in the KMyc experiment.

While the KMyc model did not respond as strongly to radiation as the KP allografts, it did display a statistically significant difference between the control and treated groups. This combined with the variation in ^{11}C-acetate avidity means that it was deemed the model best suited to assessing whether there was a correlation between ^{11}C-acetate uptake and radioresistance.

This analysis found that there was a statistically significant correlation between the ^{11}C-acetate uptake in the KMyc tumours and the post-treatment change in longest length in the treated group but not in the control group. The tumours with a low SUVMax were growing slower and therefore responding more strongly to the radiation while high SUVMax tumours were growing more quickly. This means that in this model, the ^{11}C-acetate SUVMax appears to be predictive of radioresistance. This was further validated by the fact that there was no correlation between the SUVMax and the pretreatment size, indicating that a high SUVMax is not just a proxy measurement of a larger, more metabolically active tumour. There was also no correlation between the GLUT1 and FASN stains performed on GEMM tumours; this means that increased ^{11}C-acetate uptake is not just a correlate of ^{18}F-FDG but its own distinct phenotype that has independent predictive value.

6.4.3 Limitations

One of the biggest limitations associated with this study was the sample size. Approximately one-quarter of the initial cohorts of induced KP and KMyc GEMM mice survived to endpoint; had a higher survival rate been achieved then it may have been possible to show that there was a significant difference between the treatment and control groups in the KP GEMM cohort.

One way to boost tumour sample size without needing to increase survival would be to perform MRIs instead of CTs for the pre- and post-treatment scans as the

MRI has better soft tissue definition. CT images were originally chosen because the treatment planning image taken on the day of the irradiation is a CT. Using this as the baseline reduces both the number of times the mouse must be anaesthetised and the total amount of time the mouse is under per irradiation (a CT scan using the SARRP's native CBCT scanner takes five minutes, and an MRI 30-45 minutes). Given that the tumours were growing in the lung, which is one of the few areas with high contrast between the tumour and the surrounding normal tissue, it was assumed that a CT would be sufficient. However, because some of the tumours in the post-treatment scans grew large enough that they ended up pressed against the walls of the chest several tumours had to be excluded from the final study. Using the MRI instead of the CT would improve soft tissue definition and potentially mean that some of the tumours that would have been excluded in this study could be used in future experiments. If an MRI were to be used, performing an additional T2 scan or using contrast enhanced T1 scan could also make it easier to distinguish between the tumours.

Another limitation was the lack of clinical relevance of the fractionation schedule. When this series of experiments was originally planned a second fractionation schedule of 24Gy/3# was going to be delivered to a different cohort for comparison (24Gy/3# calculated to be the isoeffective dose in 3# to 16.5Gy/1#). Due to limits on mouse stocks and breeding during lockdown the scope of the project was reduced to one fractionation schedule; as the experiments with the 16.5Gy/1# regimen had already begun prior to lockdown this was expanded on and fractionated treatments were not assessed. Verifying these findings in a fractionated model would increase the clinical relevance of the findings.

7. CONCLUSION

7.1 Summary of Key Findings

Chapter 2 evaluates the precision and accuracy of the Small Animal Radiation Research Platform (SARRP) through an analysis of quality assurance (QA) protocols, treatment plans and gamma index analyses. A retrospective audit of QA data demonstrated that the SARRP consistently achieves sub-0.5 mm precision. The study assessed different treatment plans, revealing that while targeted parallel opposed beam plans spare the heart to an extent that's comparable to the arc plans, they result in a higher dose to the liver. Verification via gamma index analysis affirmed the SARRP's accuracy in delivering planned treatments. The work in this chapter indicates that the SARRP is capable of precise and accurate treatments.

Chapter 3 verifies the delivery of radiotherapy to subcutaneous allografts and GEMM tumours. Using γH2AX staining as an indicator that a region or tumour had been irradiated, the study shows that the SARRP was capable of individually targeting tumours within the 3 GEMM mice using 1mm margins. Closely situated allografts resulted in one of the subcutaneous only being partially irradiated, resulting in the use of 2mm margins instead of 1mm margins being used in later experiments. γH2AX staining also indicated that the proportion of the heart and the liver irradiated in the normal tissue study was similar to that calculated by the TPS, using V95 as an indicator of the proportion of the PTV that was covered by the full dose.

In Chapter 4, the whole lung irradiation group showed weight loss and increased lung density in the Week 4 scan, with the former being mitigated by the introduction of nutra-gel from Week 2 onwards. This indicates that oesophageal radiation exposure may be a limiting factor in the survival of mice treated with whole lung radiotherapy, although it is not definitive as more highly powered studies supported by histology and other imaging modalities would be needed to confirm this. The experiments in this chapter also indicated that the aeration ratio may be more sensitive to changes in the lung post radiotherapy, potentially resulting in it being more predictive of survival than changes in mean Hounsfield

Units (HU), although the sample size was not sufficient to demonstrate this definitively.

Chapter 5 explores subcutaneous allografts of KP tumours as a potentially suitable preclinical model of lung cancer for PET experiments using ^{11}C-acetate. 3 different cell lines with varying acetate avidities in vitro were selected to increase variability in acetate uptake amongst the cohort. This did not translate to the subcutaneous tumours, and in vivo the low radiotracer uptake meant that the usefulness of the model was highly limited. However, a comparison of change in longest lengths post radiotherapy across the three cells lines suggested that the different cell lines had varying radiosensitivities, which implies more variation in radioresistance in the KP model than was observed in the experiments in Chapter 6. These findings are however limited by the lack of clinical relevance of the subcutaneous models relative to the GEMMs.

Chapter 6 analyses whether there is a correlation between change in tumour longest length post-irradiation, which used as a metric of radiosensitivity, and ^{11}C-acetate PET SUVMax in models of NSCLC. SUVMax of ^{11}C-acetate appears to be highly predictive of change in longest length in the KMyc treatment group but not in the control group. This suggests that the difference in response is in fact a response to the irradiation and not variation innate to the tumour. This was also true of the KP group; however, the fact that only the KMyc model showed a statistically significant difference in pre- and post-treatment changes in longest length complicates the findings for the KP model. These findings suggest that ^{11}C-acetate SUVMax could be correlated with change in longest length post radiotherapy in the KMyc model, although the study's small sample size and lack of a fractionated treatment cohort for comparison limit its usefulness.

7.2 Clinical Relevance and Key Contributions

While due to the low sample sizes in many of the experiments the data in this thesis cannot be assumed to be generalisable, the studies still contribute to the field in a number of ways.

Firstly, the GEMM studies are not only novel as demonstrated by the literature search in the introduction, but also clinically relevant. The criteria for experiments on outlined in the 'Imaging biomarker roadmap for cancer studies' (O'Connor et al, 2016), indicates that new biomarkers should meet an unmet clinical need, in this case the need to identify potentially radioresistant tumours, and not have sufficient existing data that could be analysed instead. The lack of existing data can be demonstrated by the fact that while preclinical ^{11}C-acetate PET imaging experiments have been performed previously, such as Lewis et al's 2014 paper exploring late imaging with ^{11}C-acetate and Chung et al's 2017 paper looking at early response monitoring of prostate cancer xenografts, there are no papers using GEMMs to explore ^{11}C-acetate PET as an imaging biomarker of radioresistance. The experiments in this thesis suggest a relationship between acetate avidity and radioresistance that could be used for treatment personalisation if the imaging biomarker was validated, although further preclinical research would be required before to meet the benchmark suggested in the roadmap paper, as will be discussed in the 'Future Work' section below.

The data, specifically those shown in Figure 40, also suggest that GEMMs are more suitable for preclinical radiotherapy response research using ^{11}C-acetate PET than subcutaneous allografts due to higher variability in ^{11}C-acetate uptake. A number of papers already discuss the differences between GEMMs and subcutaneous tumours in the context of preclinical imaging or radiotherapy; for example, Becher & Holland's 2006 paper describes how the advancement of imaging techniques such as MRI should encourage the adoption of the more clinically relevant GEMMs by overcoming difficulties in tumour monitoring, while Castle et al's 2017 paper discusses how GEMMs recapitulate the tumour microenvironment more effectively, making them more suitable for radiobiology research. However, no paper has been written specifically comparing the

suitability of subcutaneous models to GEMMs for ^{11}C-acetate PET radiotherapy response research in NSCLC or other cancers. Using allografts of the KP model rather than patient derived xenografts allows for direct comparison between the subcutaneous allografts and the KP GEMMs, and the fact that the subcutaneous allografts differ from the KP GEMMs both in radiation sensitivity (Figure 41) and ^{11}C-acetate SUVMax range (Figure 40) indicates that subcutaneous tumours may be both less clinically relevant and display completely different characteristics in vivo to the tumours they are derived from. While this is the first experiment looking at this in relation to radiotherapy and ^{11}C-acetate PET imaging, the findings align with previous research that indicates that subcutaneous tumours lack the inflammatory responses (Tan et al., 2021) and immune microenvironment (Horton et al., 2021) of orthotopic tumours as well as having a greater number of functional blood vessels (Guerin et al, 2020). This is a problem because, as pointed out in the 'Roadmap for Precision Preclinical X-Ray Radiation Studies', while models with spontaneously grown tumours are often better for treatment response research most preclinical studies still use transplanted cell lines (Verhaegen et al, 2023). The data shown in Figures 40 and 41 add evidence to support the idea that, when possible, GEMM models should be used for preclinical PET and radiotherapy studies.

This thesis also highlights that different GEMMs produce tumours that vary in how practical they are to perform clinically relevant treatments on. As discussed in Chapter 3 and 6, the KP GEMMs had tumours that could usually be individually targeted, although as indicated by Mouse 3 in Figure 22 this varied between mice. In contrast, the spontaneous tumours in the KMyc GEMMs were too close together to individually target across the entire cohort, meaning that the entire lung had to be irradiated for each mouse. This is important because findings in Chapter 4 that indicated that the C57BL/6 mice of the same sex and age that were receiving the same whole-lung radiotherapy treatment regimen had different survival times and changes in aeration ratio and Mean HU. This thesis could both inform choices on model based on the potential clinical relevance of the eventual treatment and highlight confounding factors for tracking disease progression; the fact that the symptomatic mice in the normal tissue study displayed similar clinical signs to the mice with high tumour burdens in the

GEMM experiment, such as hunching, weight loss and difficulty recovering from scruffing, irradiation of large amounts of normal lung tissue could cause complications in longer studies tracking clinical signs and survival.

7.3 Future Work

The Imaging Biomarker roadmap refers to the Bradford Hill principles for establishing evidence for new imaging biomarkers (O'Connor et al, 2016), which include the following criteria that could be relevant to designing future experiments to build on the work in this thesis; scientific coherence, strength of association, specificity, effect gradient, temporality and consistency. Below I will outline experiments that could be performed to strengthen the evidence collected in this thesis in line with these principles.

Firstly, for the purposes of scientific coherence, the imaging results should be compared to a ground truth. This was attempted for a number of the mice in the experiments in Chapter 6, but it was difficult to determine exactly which tumour on the PET scan corresponded to the histology, especially in the KMyc mice due to the number of tumours in close proximity. One option to address this would be to use frozen sectioning with FASN staining, which should provide an image that is more directly comparable to the slices of the PET scan. This could show that ^{11}C-acetate uptake in our experiments reflects the underlying tumour biology.

Some aspects of specificity have been considered in the studies already performed, such as comparing the irradiated groups to control groups to isolate the effects of the radiotherapy. One aspect that would need to be improved if a longer-term study was to be performed to, for example, determine the relationship between ^{11}C-acetate PET, radioresistance and survival post treatment would be ensuring more conformal treatments to reduce the side effects from irradiation of normal tissue. This is because as discussed earlier in this Chapter, the clinical signs associated with irradiation of normal lung tissue (such as hunching and weight loss) can resemble those of high tumour burden NSCLC GEMM mice. If aeration ratio were validated as an early imaging biomarker of radiation induced lung damage, it could be possible to use the changes in lung aeration post-radiotherapy in tumour bearing mice to determine whether certain mice reach endpoint sooner because of normal tissue reactions rather than tumour burden. However, confounding factors such as the impact that the tumours could have on the density of normal lung tissue around them would also need to be considered.

Some evidence of the strength of association and effect gradient can already be found in the experiments in this thesis, with Figures 42 and 43 showing the statistically significant correlation between the ^{11}C-acetate SUVMax and the KP and KMyc models respectively. A more robust study with a larger cohort would be able to demonstrate this more strongly.

Finally, moving away from the criteria outlined in the roadmap, further research utilizing dual tracer technology should be undertaken to determine whether there are distinct imaging phenotypes that arise from the combination of the information from ^{11}C-acetate PET scans and another tracer. Early unpublished research from our lab has indicated that this relationship could exist between ^{18}F-FDG and ^{11}C-acetate, but combining ^{11}C-acetate with ^{18}F-MISO could also yield interesting results that could interrogate the relationship between ^{11}C-acetate and hypoxia.

Bibliography

Abramyuk, A., Tokalov, S., Zöphel, K., Koch, A., Szluha Lazanyi, K., Gillham, C., & Abolmaali, N. 2009. Is pre-therapeutical FDG-PET/CT capable to detect high risk tumor subvolumes responsible for local failure in non-small cell lung cancer? Radiotherapy and Oncology, 91(3), 399–404. https://doi.org/10.1016/j.radonc.2009.01.003

Aerts, H. J. W. L., Baardwijk, A. A. W., Petit, S. F., Offermann, C., Loon, J. van, Houben, R., & Ruysscher, D. D. 2009. Identification of residual metabolic-active areas within individual NSCLC tumours using a pre-radiotherapy 18Fluorodeoxyglucose-PET-CT scan. Radiotherapy and Oncology, 91(3), 386–392. https://doi.org/10.1016/j.radonc.2009.03.006

Ajdari, A., Shusharina, N., Liao, Z., Mohan, R., & Bortfeld, T. 2019. Mid-Treatment [18]F-FDG PET Uptakes Can Predict Symptomatic Radiation Pneumonitis in Non-Small Cell Lung Cancer Patients. International Journal of Radiation Oncology*Biology*Physics, 105(1), 224. https://doi.org/10.1016/j.ijrobp.2019.06.315

Ali, R., Apte, S., Vilalta, M., Subbarayan, M., Miao, Z., Chin, F. T., & Graves, E. E. 2015. PET Is Predictive of Response to Fractionated Radiotherapy in Preclinical Tumor Models. PLOS ONE, 10(10), 18–5. https://doi.org/10.1371/journal.pone.0139425

Ashland LLC. (n.d.). GAFCHROMIC™ DOSIMETRY MEDIA, TYPE EBT-3. Retrieved October 1, 2023, from http://www.gafchromic.com/documents/EBT3_Specifications.pdf

Benson, R., Madan, R., Kilambi, R., & Chander, S. 2016. Radiation induced liver disease: A clinical update. Journal of the Egyptian National Cancer Institute, 28(1), 7–11. https://doi.org/10.1016/j.jnci.2015.08.001

Bentourkia, M., alla Abdo, R., Shu Wang, C., Lavallee, E., Lessard, F., & Bentourkia, M. 2021. Early Detection of Response to Radiotherapy Treatment with 11C-Acetate PET Imaging. RCO, 1–3. https://doi.org/10.31487/j.rco.2021.01.03

Becher, O.J. and Holland, E.C. 2006. Genetically Engineered Models Have Advantages over Xenografts for Preclinical Studies. Cancer Research 66(7), pp. 3355–3359. Available at: http://dx.doi.org/10.1158/0008-5472.CAN-05-3827.

Beckers, C., Pruschy, M., & Vetrugno, I. 2024. Tumor hypoxia and radiotherapy: A major driver of resistance even for novel radiotherapy modalities. In Seminars in Cancer Biology (Vol. 98, pp. 19–30). Elsevier BV. https://doi.org/10.1016/j.semcancer.2023.11.006

Biglin, E. R., Price, G. J., Chadwick, A. L., Aitkenhead, A. H., Williams, K. J., & Kirkby, K. J. 2019. Preclinical dosimetry: exploring the use of small animal phantoms. Radiat Oncol, 14(1). https://doi.org/10.1186/s13014-019-1343-8

Briske-Anderson, M. J., Finley, J. W., & Newman, S. M. 1997. The Influence of Culture Time and Passage Number on the Morphological and Physiological Development of Caco-2 Cells. Experimental Biology and Medicine, 214(3), 248–257. https://doi.org/10.3181/00379727-214-44093

Cancer Research UK. (n.d.). Lung Cancer Statistics. Cancer Research UK. Retrieved September 1, 2023, from https://www.cancerresearchuk.org/health-professional/cancer-statistics/statistics-by-cancer-type/lung-cancer

Cancer Research UK. 2015, July 19. A Cancer of Substantial Unmet Need: Why We're Making Lung Cancer A Priority - Cancer Research UK - Cancer News. Cancer Research UK - Cancer News. https://news.cancerresearchuk.org/2015/07/20/a-cancer-of-substantial-unmet-need-why-were-making-lung-cancer-a-

Carmichael, J., Degraff, W. G., Gamson, J., Russo, D., Gazdar, A. F., Levitt, M. L., Minna, J. D., & Mitchell, J. B. 1989. Radiation sensitivity of human lung cancer cell lines. European Journal of Cancer and Clinical Oncology, 25(3), 527–534. https://doi.org/10.1016/0277-5379(89)90266-6

Castillo, R., Pham, N., Ansari, S., Meshkov, D., Castillo, S., Li, M., & Guerrero, T. 2014. Pre-radiotherapy FDG PET predicts radiation pneumonitis in lung cancer. Radiation Oncology, 9(1), 74. https://doi.org/10.1186/1748-717x-9-74

Castle, K. D., Chen, M., Wisdom, A. J., & Kirsch, D. G. 2017. Genetically engineered mouse models for studying radiation biology. AME Publishing Company. https://doi.org/10.21037/tcr.2017.06.19

Chang, D.S., Lasley, F.D., Das, I.J., Mendonca, M.S., Dynlacht, J.R. 2014. Therapeutic Ratio. In: Basic Radiotherapy Physics and Biology. Springer, Cham. https://doi.org/10.1007/978-3-319-06841-1_27

Chang, L., Fang, S., Chen, Y., Yang, Z., Yuan, Y., Zhang, J., Ye, L., & Gu, W. 2019. Inhibition of FASN suppresses the malignant biological behavior of non-small cell lung cancer cells via deregulating glucose metabolism and AKT/ERK pathway. Lipids Health Dis, 18(1). https://doi.org/10.1186/s12944-019-1058-8

Chaurasia, R.K., Bhat, N.N., Gaur, N., Shirsath, K.B., Desai, U.N., Sapra, B.K., 2021. Establishment and multiparametric-cytogenetic validation of 60Co-gamma-ray induced, phospho-gamma-H2AX calibration curve for rapid biodosimetry and triage management during radiological emergencies. Mutation Research/Genetic Toxicology and Environmental Mutagenesis. https://doi.org/10.1016/j.mrgentox.2021.503354

Cheng, H., Wang, M., Su, J., Li, Y., Long, J., Chu, J., Wan, X., Cao, Y., & Li, Q. 2022. Lipid Metabolism and Cancer. Life, 12(6), 784. https://doi.org/10.3390/life12060784

Cheng, M., Jolly, S., Quarshie, W. O., Kapadia, N., Vigneau, F. D., & Kong, F.-M. (Spring). 2019. Modern Radiation Further Improves Survival in Non-Small Cell Lung Cancer: An Analysis of 288,670 Patients. J. Cancer, 10(1), 168–177. https://doi.org/10.7150/jca.26600

Chung, Y.-H., Tsai, C.-K., Wang, C.-C., Chen, H.-M., Lu, K.-Y., Chiu, H., Lin, Y.-C., Yen, T.-C., & Lin, G. 2017. Early Response Monitoring Following Radiation Therapy by Using [18F] FDG and [11C]Acetate PET in Prostate Cancer Xenograft Model with Metabolomics Corroboration. In Molecules (Vol. 22, Issue 11, p. 1946). MDPI AG. https://doi.org/10.3390/molecules22111946

Cocco, E., Scaltriti, M., & Drilon, A. 2018. NTRK fusion-positive cancers and trk inhibitor therapy. Nature Reviews Clinical Oncology, 15(12), 731–747. https://doi.org/10.1038/s41571-018-0113-0

Corry, J., & Rischin, D. 2004. Strategies to overcome accelerated repopulation and hypoxia—what have we learned from clinical trials? Seminars in Oncology, 31(6), 802–808. https://doi.org/10.1053/j.seminoncol.2004.09.005

Craig, D.J., Nanavaty, N.S., Devanaboyina, M., Stanbery, L., Hamouda, D., Edelman, G., Dworkin, L., Nemunaitis, J.J., 2021. The Abscopal Effect of Radiation Therapy. Future Oncol. https://doi.org/10.2217/fon-2020-0994

Currie, E., Schulze, A., Zechner, R., Walther, T. C., & Farese, R. V. 2013. Cellular Fatty Acid Metabolism and Cancer. Cell Metabolism, 18(2), 153–161. https://doi.org/10.1016/j.cmet.2013.05.017

Das, A. K., Bell, M. H., Nirodi, C. S., Story, M. D., & Minna, J. D. 2010. Radiogenomics Predicting Tumor Responses to Radiotherapy in Lung Cancer. Seminars in Radiation Oncology, 20(3), 149–155. https://doi.org/10.1016/j.semradonc.2010.01.002

Das, S., Kharade, V., Pandey, V., KV, A., Pasricha, R. K., & Gupta, M. 2022. Gamma Index Analysis as a Patient-Specific Quality Assurance Tool for High-Precision Radiotherapy: A Clinical Perspective of Single Institute Experience. https://doi.org/10.7759/cureus.30885

de Bruin, E. C., McGranahan, N., Mitter, R., Salm, M., Wedge, D. C., Yates, L., Jamal-Hanjani, M., Shafi, S., Murugaesu, N., & Rowan, A. J. 2014. Spatial and temporal diversity in genomic instability processes defines lung cancer evolution. Science, 346(6206), 251–256. https://doi.org/10.1126/science.1253462

Deng, H., Kennedy, C. W., Armour, E., Tryggestad, E., Ford, E., McNutt, T., Jiang, L., & Wong, J. 2007. The small-animal radiation research platform (SARRP): dosimetry of a focused lens system. Phys. Med. Biol., 52(10), 2729–2740. https://doi.org/10.1088/0031-9155/52/10/007

Diessen, J., Ruysscher, D., Sonke, J.-J., Damen, E., Sikorska, K., Reymen, B., & Belderbos, J. 2018. The acute and late toxicity results of a randomized phase II dose-escalation trial in non-small cell lung cancer (PET-boost trial. Radiotherapy and Oncology. https://doi.org/10.1016/j.radonc.2018.09.019

Dong, Y., Tu, R., Liu, H., & Qing, G. 2020. Regulation of cancer cell metabolism: oncogenic MYC in the driver's seat. Sig Transduct Target Ther, 5(1). https://doi.org/10.1038/s41392-020-00235-2

Dove, A.P.H., Cmelak, A., Darrow, K., McComas, K.N., Chowdhary, M., Beckta, J., Kirschner, A.N., 2022. The Use of Low-Dose Radiation Therapy in Osteoarthritis: A Review. International Journal of Radiation Oncology*Biology*Physics. https://doi.org/10.1016/j.ijrobp.2022.04.029

Elmpt, W., Ruysscher, D., Salm, A., Lakeman, A., Stoep, J., Emans, D., & Belderbos, J. 2012. The PET-boost randomised phase II dose-escalation trial in non-small cell lung cancer. Radiotherapy and Oncology, 104(1), 67–71. https://doi.org/10.1016/j.radonc.2012.03.005

Eltayeb, K., La Monica, S., Tiseo, M., Alfieri, R., & Fumarola, C. 2022. Reprogramming of Lipid Metabolism in Lung Cancer: An Overview with Focus on EGFR-Mutated Non-Small Cell Lung Cancer. Cells, 11(3), 413. https://doi.org/10.3390/cells11030413

Ettinger, D. S., Wood, D. E., Aggarwal, C., Aisner, D. L., Akerley, W., & Bauman, J. 2020.. NCCN guidelines insights: non-small cell lung cancer, version 1. J Natl Compr Canc Netw, 17(12), 1464–1472. https://doi.org/10.6004/jnccn.2019.0059

Fernandez, J. L., Årbogen, S., Sadeghinia, M. J., Haram, M., Snipstad, S., Torp, S. H., Einen, C., Mühlenpfordt, M., Maardalen, M., Vikedal, K., & Davies, C. de L. 2023. A Comparative Analysis of Orthotopic and Subcutaneous Pancreatic Tumour Models: Tumour Microenvironment and Drug Delivery. In Cancers (Vol. 15, Issue 22, p. 5415). MDPI AG. https://doi.org/10.3390/cancers15225415

Fu, Y., Zou, T., Shen, X., Nelson, P. J., Li, J., Wu, C., Yang, J., Zheng, Y., Bruns, C., & Zhao, Y. 2021. Lipid metabolism in cancer progression and therapeutic strategies. MedComm, 2(1), 27–59. https://doi.org/10.1002/mco2.27

Giraud, P., & Houle, A. 2013. Respiratory Gating for Radiotherapy: Main Technical Aspects and Clinical Benefits. ISRN Pulmonology, 2013, 1–13. https://doi.org/10.1155/2013/519602

Guerin, M. V., Finisguerra, V., Van den Eynde, B. J., Bercovici, N., & Trautmann, A. 2020. Preclinical murine tumor models: A structural and functional perspective. eLife Sciences Publications, Ltd. https://doi.org/10.7554/elife.50740

Gradl, R., Dierolf, M., Günther, B., Hehn, L., Möller, W., Kutschke, D., Yang, L., Donnelley, M., Murrie, R., Erl, A., Stoeger, T., Gleich, B., Achterhold, K., Schmid, O., Pfeiffer, F., & Morgan, K. S. 2018. In vivo Dynamic Phase-Contrast X-ray Imaging using a Compact Light Source. In Scientific Reports (Vol. 8, Issue 1). Springer Science and Business Media LLC. https://doi.org/10.1038/s41598-018-24763-8

Gurtner, K., Kryzmien, Z., Koi, L., Wang, M., Benes, C. H., Hering, S., Willers, H., Baumann, M., & Krause, M. 2020. Radioresistance of KRAS/TP53-mutated lung cancer can be overcome by radiation dose escalation or EGFR tyrosine kinase inhibition in vivo. Intl Journal of Cancer, 147(2), 472–477. https://doi.org/10.1002/ijc.32598

Hall, E. J., & Giaccia, A. J. 2012. Radiobiology for the radiologist (7th ed.). Lippincott Williams & Wilkins.

Hall, Z., Ament, Z., Wilson, C. H., Burkhart, D. L., Ashmore, T., Koulman, A., Littlewood, T., Evan, G. I., & Griffin, J. L. 2016. Myc Expression Drives Aberrant Lipid Metabolism in Lung Cancer. 76(16), 4608–4618. https://doi.org/10.1158/0008-5472.can-15-3403

Hanahan, D. 2022. Hallmarks of Cancer: New Dimensions. 12(1), 31–46. https://doi.org/10.1158/2159-8290.cd-21-1059

Hanahan, D., & Weinberg, R. A. 2000. The Hallmarks of Cancer. Cell, 100(1), 57–70. https://doi.org/10.1016/s0092-8674(00)81683-9

Hanahan, D., & Weinberg, R. A. 2011. Hallmarks of Cancer: The Next Generation. Cell, 144(5), 646–674. https://doi.org/10.1016/j.cell.2011.02.013

Hassaballa, H. A., Cohen, E. S., Khan, A. J., Ali, A., Bonomi, P., & Rubin, D. B. 2005. Positron Emission Tomography Demonstrates Radiation-Induced Changes to Nonirradiated Lungs in Lung Cancer Patients Treated with Radiation and Chemotherapy. Chest, 128(3), 1448–1452. https://doi.org/10.1378/chest.128.3.1448

Hensley, C. T., Faubert, B., Yuan, Q., Lev-Cohain, N., Jin, E., Kim, J., Jiang, L., Ko, B., Skelton, R., & Loudat, L. 2016. Metabolic Heterogeneity in Human Lung Tumors. Cell, 164(4), 681–694. https://doi.org/10.1016/j.cell.2015.12.034

Heyden, B. V. D., van Hoof, S. J., Schyns, L. E. J. R., & Verhaegen, F. 2017. The influence of respiratory motion on dose delivery in a mouse lung tumour irradiation using the 4D MOBY phantom. BJR, 90(1069), 20160419. https://doi.org/10.1259/bjr.20160419

Hill, M. A., Thompson, J. M., Kavanagh, A., Tullis, I. D. C., Newman, R. G., Prentice, J., Beech, J., Gilchrist, S., Smart, S., Fokas, E., & Vojnovic, B. 2017. The Development of Technology for Effective Respiratory-Gated Irradiation Using an Image-Guided Small Animal Irradiator. In Radiation Research (Vol. 188, Issue 3, p. 247). Radiation Research Society. https://doi.org/10.1667/rr14753.1

Hill, W., Caswell, D. R., & Swanton, C. 2021. Capturing cancer evolution using genetically engineered mouse models (GEMMs). In Trends in Cell Biology (Vol. 31, Issue 12, pp. 1007–1018). Elsevier BV. https://doi.org/10.1016/j.tcb.2021.07.003

Horn, S., Barnard, S., Rothkamm, K., 2011. Gamma-H2AX-Based Dose Estimation for Whole and Partial Body Radiation Exposure. PLoS ONE. https://doi.org/10.1371/journal.pone.0025113

Jackson, I.L., Vujaskovic, Z., Down, J.D., 2010. Revisiting Strain-Related Differences in Radiation Sensitivity of the Mouse Lung: Recognizing and Avoiding the Confounding Effects of Pleural Effusions. Radiation Research. https://doi.org/10.1667/rr1911.1

Jackson, M.R., Stevenson, K., Chahal, S.K., Curley, E., Finney, G.E., Gutierrez-Quintana, R., Onwubiko, E., Rupp, A., Strathdee, K., Williams, K., MacLeod, M.K.L., McSharry, C., Chalmers, A.J., 2022. Low-Dose Lung Radiation Therapy for COVID-19 lung disease: A Preclinical Efficacy Study in a Bleomycin Model of Pneumonitis. International Journal of Radiation Oncology*Biology*Physics. https://doi.org/10.1016/j.ijrobp.2021.08.029

Jackson, M. R., Stevenson, K., Chahal, S. K., Curley, E., Finney, G. E., Gutierrez-Quintana, R., Onwubiko, E., Rupp, A., Strathdee, K., & Williams, K. 2022. Low-Dose Lung Radiation Therapy for COVID-19 Lung Disease: A Preclinical Efficacy Study in a Bleomycin Model of Pneumonitis. International Journal of Radiation Oncology*Biology*Physics, 112(1), 197–211. https://doi.org/10.1016/j.ijrobp.2021.08.029

Jasper, K., Liu, B., Olson, R., & Matthews, Q. 2021. Evidence-Based Planning Target Volume Margin Reduction for Modern Lung Stereotactic Ablative Radiation Therapy Using Deformable Registration. Advances in Radiation Oncology, 6(6), 100750. https://doi.org/10.1016/j.adro.2021.100750

Jing, Y., Zhang, Y., Pan, R., Ding, K., Chen, R., & Meng, Q. 2022. Effect of Inhalation Anesthetics on Tumor Metastasis. Technol Cancer Res Treat, 21, 153303382211210. https://doi.org/10.1177/15330338221121092

Josipovic, M., Aznar, M. C., Thomsen, J. B., Scherman, J., Damkjaer, S. M., Nygård, L., Specht, L., Pøhl, M., & Persson, G. F. 2019. Deep inspiration breath hold in locally advanced lung cancer radiotherapy: validation of intrafractional geometric uncertainties in the INHALE trial. BJR, 92(1104), 20190569. https://doi.org/10.1259/bjr.20190569

Kauczor, H.U., Plathow, C. 2006. Imaging tumour motion for radiotherapy planning using MRI. In Cancer Imaging (Vol. 6, Issue Special Issue A, pp. S140-S144). E-MED LTD. https://doi.org/10.1102/1470-7330.2006.9027

Keall, P., Vedam, S., George, R., Bartee, C., Siebers, J., Lerma, F., Weiss, E., & Chung, T. 2006. The clinical implementation of respiratory-gated intensity-modulated radiotherapy. In Medical Dosimetry (Vol. 31, Issue 2, pp. 152–162). Elsevier BV. https://doi.org/10.1016/j.meddos.2005.12.002

Kersten, K., de Visser, K. E., van Miltenburg, M. H., & Jonkers, J. 2016. Genetically engineered mouse models in oncology research and cancer medicine. In EMBO Molecular Medicine (Vol. 9, Issue 2, pp. 137–153). Springer Science and Business Media LLC. https://doi.org/10.15252/emmm.201606857

Kesner, A. L., Lau, V. K., Speiser, M., Hsueh, W.-A., Agazaryan, N., DeMarco, J. J., Czernin, J., & Silverman, D. H. 2008. Time-course of effects of external beam radiation on [18F]FDG uptake in healthy tissue and bone marrow. Journal of Applied Clinical Medical Physics, 9(3), 147–156. https://doi.org/10.1120/jacmp.v9i3.2747

Kiel, C., Benisty, H., Lloréns-Rico, V., & Serrano, L. 2016. The yin–yang of kinase activation and unfolding explains the peculiarity of Val600 in the activation

segment of BRAF. In eLife (Vol. 5). eLife Sciences Publications, Ltd. https://doi.org/10.7554/elife.12814

Kim, J., & Jung, Y. 2017. Radiation-induced liver disease: current understanding and future perspectives. Exp Mol Med, 49(7), e359–e359. https://doi.org/10.1038/emm.2017.85

Kitamura, H., Inoue, K., Sasaki, T., Tsuda, K., Fujimori, H., Tanaka, T., … & Fujii, H. 2010. Estimation of local statistical noise in pet images induced by attenuation inside the body. Annals of Nuclear Medicine, 24(3), 197-205. https://doi.org/10.1007/s12149-010-0355-0

Koundouros, N., & Poulogiannis, G. 2019. Reprogramming of fatty acid metabolism in cancer. In British Journal of Cancer (Vol. 122, Issue 1, pp. 4–22). Springer Science and Business Media LLC. https://doi.org/10.1038/s41416-019-0650-z

Ladbury, C.J., Rusthoven, C.G., Camidge, D.R., Kavanagh, B.D., Nath, S.K., 2019. Impact of Radiation Dose to the Host Immune System on Tumor Control and Survival for Stage III Non-Small Cell Lung Cancer Treated with Definitive Radiation Therapy. International Journal of Radiation Oncology*Biology*Physics. https://doi.org/10.1016/j.ijrobp.2019.05.064

Lewis, D.Y., Boren, J., Shaw, G.L., Bielik, R., Ramos-Montoya, A., Larkin, T.J., Martins, C.P., Neal, D.E., Soloviev, D., Brindle, K.M., 2014. Late Imaging with [1-11C]Acetate Improves Detection of Tumor Fatty Acid Synthesis with PET. J Nucl Med. https://doi.org/10.2967/jnumed.113.134437

Li, C., Zhang, X., Pang, L., Huang, Y., Gao, Y., Sun, X., & Meng, X. 2018. Spatial Concordance of Tumor Proliferation and Accelerated Repopulation from Pathologic Images to 3′-[18F]Fluoro-3′-Deoxythymidine PET Images: a Basic Study Guided for PET-Based Radiotherapy Dose Painting. Molecular Imaging and Biology. https://doi.org/10.1007/s11307-018-1292-x

Li, H., Feng, Z., & He, M.-L. 2020. Lipid metabolism alteration contributes to and maintains the properties of cancer stem cells. Theranostics, 10(16), 7053–7069. https://doi.org/10.7150/thno.41388

Li, X., Liu, M., Liu, H., & Chen, J. 2022. Tumor metabolic reprogramming in lung cancer progression (Review). Oncol Lett, 24(2). https://doi.org/10.3892/ol.2022.13407

Liberti, M. V., & Locasale, J. W. 2016. The Warburg Effect: How Does it Benefit Cancer Cells? Trends in Biochemical Sciences, 41(3), 211–218. https://doi.org/10.1016/j.tibs.2015.12.001

Liu, Y., Zheng, C., Huang, Y., He, M., Xu, W. W., & Li, B. 2021. Molecular mechanisms of chemo- and radiotherapy resistance and the potential implications for cancer treatment. In MedComm (Vol. 2, Issue 3, pp. 315–340). Wiley. https://doi.org/10.1002/mco2.55

Lung Cancer Statistics. (n.d.). Cancer Research UK. Retrieved October 1, 2023, from https://www.cancerresearchuk.org/health-professional/cancer-statistics/statistics-by-cancer-type/lung-cancer

Lv, X., Mao, Z., Sun, X., & Liu, B. 2023. Intratumoral Heterogeneity in Lung Cancer. Cancers, 15(10), 2709. https://doi.org/10.3390/cancers15102709

Ma, C. -M., Coffey, C. W., DeWerd, L. A., Liu, C., Nath, R., Seltzer, S. M., & Seuntjens, J. P. 2001. AAPM protocol for 40–300 kV x-ray beam dosimetry in radiotherapy and radiobiology. Medical Physics, 28(6), 868–893. https://doi.org/10.1118/1.1374247

McCurdy, M. R., Castillo, R., Martinez, J., Al Hallack, M. N., Lichter, J., Zouain, N., & Guerrero, T. 2012. 18F]-FDG uptake dose–response correlates with radiation pneumonitis in lung cancer patients. Radiotherapy and Oncology, 104(1), 52–57. https://doi.org/10.1016/j.radonc.2012.04.003

Méndez, I, Polšak, A., Hudej, R., & Casar, B. 2018. The Multigaussian method: a new approach to mitigating spatial heterogeneities with multichannel radiochromic film dosimetry. Phys. Med. Biol., 63(17), 175013. https://doi.org/10.1088/1361-6560/aad9c1

Méndez, Ignasi, Rovira-Escutia, J. J., & Casar, B. 2021. A protocol for accurate radiochromic film dosimetry using Radiochromic.com. 55(3), 369–378. https://doi.org/10.2478/raon-2021-0034

Miele, E., Spinelli, G., Tomao, F., Zullo, A., Marinis, F., Pasciuti, G., & Tomao, S. 2008. Positron Emission Tomography (PET) radiotracers in oncology – utility of 18F-Fluoro-deoxy-glucose (FDG)-PET in the management of patients with non-small-cell lung cancer (NSCLC. Journal of Experimental & Clinical Cancer Research, 27(1), 52. https://doi.org/10.1186/1756-9966-27-52

Mowday, A. M., Lieuwes, N. G., Biemans, R., Marcus, D., Rezaeifar, B., Reniers, B., Verhaegen, F., Theys, J., & Dubois, L. J. 2020. Use of a Luciferase-Expressing Orthotopic Rat Brain Tumor Model to Optimize a Targeted Irradiation Strategy for Efficacy Testing with Temozolomide. In Cancers (Vol. 12, Issue 6, p. 1585). MDPI AG. https://doi.org/10.3390/cancers12061585

Mylonis, I., Simos, G., & Paraskeva, E. 2019. Hypoxia-Inducible Factors and the Regulation of Lipid Metabolism. Cells, 8(3), 214. https://doi.org/10.3390/cells8030214

Ni, Y., Yang, Y., Ran, J., Zhang, L., Yao, M., Liu, Z., & Zhang, L. 2020. miR-15a-5p inhibits metastasis and lipid metabolism by suppressing histone acetylation in lung cancer. Free Radical Biology and Medicine, 161, 150–162. https://doi.org/10.1016/j.freeradbiomed.2020.10.009

National Institute for Health and Care Excellence. 2019. Lung cancer: diagnosis and management. NICE. https://www.nice.org.uk/guidance/ng122/resources/lung-cancer-diagnosis-and-management-pdf-66141655525573

National Institute for Health and Care Excellence. 2024. Tools and resources: Lung Cancer: Diagnosis and management: Guidance. NICE. https://www.nice.org.uk/guidance/ng122/resources

Nitsch, S., Hakenberg, O. W., Heuschkel, M., Drager, D., Hildebrandt, G., Krause, B. J., & Schwarzenbock, S. M. 2016. Evaluation of Prostate Cancer with 11C- and 18F-Choline PET/CT: Diagnosis and Initial Staging. Journal of Nuclear Medicine, 57(Supplement_3), 38–42. https://doi.org/10.2967/jnumed.115.169748

Nomori, H., Shibata, H., Uno, K., Iyama, K., Honda, Y., Nakashima, R., & Horio, H. 2008. 11C-Acetate can be Used in Place of 18F-Fluorodeoxyglucose for

Positron Emission Tomography Imaging of Non-small Cell Lung Cancer with Higher Sensitivity for Well-Differentiated Adenocarcinoma. Journal of Thoracic Oncology, 3(12), 1427–1432. https://doi.org/10.1097/jto.0b013e31818ddfdc

O'Connor, J. P. B., Aboagye, E. O., Adams, J. E., Aerts, H. J. W. L., Barrington, S. F., Beer, A. J., Boellaard, R., Bohndiek, S. E., Brady, M., Brown, G., Buckley, D. L., Chenevert, T. L., Clarke, L. P., Collette, S., Cook, G. J., deSouza, N. M., Dickson, J. C., Dive, C., Evelhoch, J. L., … Waterton, J. C. 2016. Imaging biomarker roadmap for cancer studies. In Nature Reviews Clinical Oncology (Vol. 14, Issue 3, pp. 169–186). Springer Science and Business Media LLC. https://doi.org/10.1038/nrclinonc.2016.162

O'Sullivan, É., Keogh, A., Henderson, B., Finn, S. P., Gray, S. G., & Gately, K. 2023. Treatment Strategies for KRAS-Mutated Non-Small-Cell Lung Cancer. In Cancers (Vol. 15, Issue 6, p. 1635). MDPI AG. https://doi.org/10.3390/cancers15061635

Owrangi, A. M., Greer, P. B., & Glide-Hurst, C. K. 2018. MRI-only treatment planning: benefits and challenges. Phys. Med. Biol., 63(5), 05TR01. https://doi.org/10.1088/1361-6560/aaaca4

Park, J. H., Pyun, W. Y., & Park, H. W. 2020. Cancer Metabolism: Phenotype, Signaling and Therapeutic Targets. In Cells (Vol. 9, Issue 10, p. 2308). MDPI AG. https://doi.org/10.3390/cells9102308

Petit, S. F., Elmpt, W. J. C., Oberije, C. J. G., Vegt, E., Dingemans, A.-M. C., Lambin, P., & Ruysscher, D. 2011. 18F]fluorodeoxyglucose Uptake Patterns in Lung Before Radiotherapy Identify Areas More Susceptible to Radiation-Induced Lung Toxicity in Non-Small-Cell Lung Cancer Patients. International Journal of Radiation Oncology*Biology*Physics, 81(3), 698–705. https://doi.org/10.1016/j.ijrobp.2010.06.016

Preim, B., & Botha, C. 2013. Labeling and Measurements in Medical Visualization. In Visual Computing for Medicine . Newnes.

Qu, B., Wang, H., Yu, W., Zhang, J., Zhang, H., & Tian, J. 2015. Evaluation of Therapeutic Effects of Radiotherapy during Treatment of Lung Adenocarcinoma in Mice with Positron Emission Tomography Imaging of 18F-FLT and 18F-FDG.

Tropical Journal of Pharmaceutical Research, 14(7), 1293. https://doi.org/10.4314/tjpr.v14i7.24

Rock, J. R., Onaitis, M. W., Rawlins, E. L., Lu, Y., Clark, C. P., Xue, Y., Randell, S. H., & Hogan, B. L. M. 2009. Basal cells as stem cells of the mouse trachea and human airway epithelium. In Proceedings of the National Academy of Sciences (Vol. 106, Issue 31, pp. 12771–12775). Proceedings of the National Academy of Sciences. https://doi.org/10.1073/pnas.0906850106

Rockwell, S., Dobrucki, I., Kim, E., Marrison, S., & Vu, V. 2009. Hypoxia and Radiation Therapy: Past History, Ongoing Research, and Future Promise. Current Molecular Medicine, 9(4), 442–458. https://doi.org/10.2174/156652409788167087

Royal College or Radiologists. 2021, March. Policy Priorities For Clinical Oncology | The Royal College Of Radiologists. https://www.rcr.ac.uk/press-and-policy/policy-priorities/policy-priorities-clinical-oncology

Ruscitti, F., Ravanetti, F., Essers, J., Ridwan, Y., Belenkov, S., Vos, W., Ferreira, F., KleinJan, A., van Heijningen, P., Van Holsbeke, C., Cacchioli, A., Villetti, G., Stellari, F.F., 2017. Longitudinal assessment of bleomycin-induced lung fibrosis by Micro-CT correlates with histological evaluation in mice. Multidiscip Respir Med. https://doi.org/10.1186/s40248-017-0089-0

Sazonova, E. V., Petrichuk, S. V., Kopeina, G. S., & Zhivotovsky, B. 2021. A link between mitotic defects and mitotic catastrophe: detection and cell fate. Biol Direct, 16(1). https://doi.org/10.1186/s13062-021-00313-7

Schmidt, D.R. 2021. 'Therapeutic radiation in genetically engineered mouse models of cancer', International Journal of Radiation Oncology, Biology, Physics, 111(3). https://doi:10.1016/j.ijrobp.2021.07.843

Schrevens, L. 2004. The Role of PET Scan in Diagnosis, Staging, and Management of Non-Small Cell Lung Cancer. The Oncologist, 9(6), 633–643. https://doi.org/10.1634/theoncologist.9-6-633

Singh, K. B., Hahm, E.-R., Kim, S.-H., Wendell, S. G., & Singh, S. V. 2021. A novel metabolic function of Myc in regulation of fatty acid synthesis in prostate cancer. Oncogene, 40(3), 592–602. https://doi.org/10.1038/s41388-020-01553-z

Singh, M., Murriel, C. L., & Johnson, L. 2012. Genetically Engineered Mouse Models: Closing the Gap between Preclinical Data and Trial Outcomes. In Cancer Research (Vol. 72, Issue 11, pp. 2695–2700). American Association for Cancer Research (AACR). https://doi.org/10.1158/0008-5472.can-11-2786

Socinski, M. A., Pennell, N. A., & Davies, K. D. 2021. METExon 14 Skipping Mutations in Non–Small-Cell Lung Cancer: An Overview of Biology, Clinical Outcomes, and Testing Considerations. In JCO Precision Oncology (Issue 5, pp. 653–663). American Society of Clinical Oncology (ASCO). https://doi.org/10.1200/po.20.00516

Soret, M., Bacharach, S. L., & Buvat, I. 2007. Partial-Volume Effect in PET Tumor Imaging. In Journal of Nuclear Medicine (Vol. 48, Issue 6, pp. 932–945). Society of Nuclear Medicine. https://doi.org/10.2967/jnumed.106.035774

Speroni, L., de los Angeles Bustuoabad, V., Gasparri, J., Chiaramoni, N. S., Taira, M. C., Ruggiero, R. A., & del Valle Alonso, S. 2009. Alternative site of implantation affects tumor malignancy and metastatic potential in mice: Its comparison to the flank model. Cancer Biology & Therapy, 8(4), 375–379. https://doi.org/10.4161/cbt.8.4.7452

Svensson, R. U., Parker, S. J., Eichner, L. J., Kolar, M. J., Wallace, M., Brun, S. N., Lombardo, P. S., Van Nostrand, J. L., Hutchins, A., & Vera, L. 2016. Inhibition of acetyl-CoA carboxylase suppresses fatty acid synthesis and tumor growth of non-small-cell lung cancer in preclinical models. Nat Med, 22(10), 1108–1119. https://doi.org/10.1038/nm.4181

Sweeney, T. M., Kibbey, M. C., Zain, M., Fridman, R., & Kleinman, H. K. 1991. Basement membrane and the SIKVAV laminin-derived peptide promote tumor growth and metastases. Cancer Metast Rev, 10(3), 245–254. https://doi.org/10.1007/bf00050795

Stenvall, A., Larsson, E., Holmqvist, B., Strand, S.-E. and Jönsson, B.-A. 2020. Quantitative γ-H2AX immunofluorescence method for DNA double-strand break analysis in testis and liver after intravenous administration of 111InCl3. EJNMMI Research 10(1). Available at: http://dx.doi.org/10.1186/s13550-020-0604-8.

Tan, Z., Xue, H., Sun, Y., Zhang, C., Song, Y., & Qi, Y. 2021. The Role of Tumor Inflammatory Microenvironment in Lung Cancer. Front. Pharmacol., 12. https://doi.org/10.3389/fphar.2021.688625

Tang, L., Wei, F., Wu, Y., He, Y., Shi, L., Xiong, F., Gong, Z., Guo, C., Li, X., & Deng, H. 2018. Role of metabolism in cancer cell radioresistance and radiosensitization methods. J Exp Clin Cancer Res, 37(1). https://doi.org/10.1186/s13046-018-0758-7

Teymurazyan, A., Riauka, T., Jans, H.-S., & Robinson, D. 2012. Properties of Noise in Positron Emission Tomography Images Reconstructed with Filtered-Backprojection and Row-Action Maximum Likelihood Algorithm. In Journal of Digital Imaging (Vol. 26, Issue 3, pp. 447–456). Springer Science and Business Media LLC. https://doi.org/10.1007/s10278-012-9511-5

Tesson, M., Stevenson, K., Karim, S. A., Nixon, C., Chalmers, A. J., Sansom, O. J., O'Neill, E., Jones, K., & Morton, J. P. 2024. Targeted irradiation in an autochthonous mouse model of pancreatic cancer. In Disease Models & Mechanisms (Vol. 17, Issue 3). The Company of Biologists. https://doi.org/10.1242/dmm.050463

Tipton, E., Hallberg, K., Hedges, L.V., Chan, W., 2016. Implications of Small Samples for Generalization: Adjustments and Rules of Thumb. Eval Rev. https://doi.org/10.1177/0193841x16655665

Thomlinson, R. H. & Gray LH. 1955. The histological structure of some human lung cancers and the possible implications for radiotherapy. Br J Cancer, 9, 539-549.

Thorwarth, D., Geets, X., & Paiusco, M. 2010. Physical radiotherapy treatment planning based on functional PET/CT data. Radiotherapy and Oncology, 96(3), 317–324. https://doi.org/10.1016/j.radonc.2010.07.012

Tong, J. and Hei, T.K. 2020. Aging and age-related health effects of ionizing radiation. Radiation Medicine and Protection 1(1), pp. 15–23. Available at: http://dx.doi.org/10.1016/j.radmp.2020.01.005.

Tsuji, A. B., Sugyo, A., Sudo, H., Suzuki, C., Wakizaka, H., Zhang, M.-R., Kato, K., & Saga, T. 2015. Preclinical assessment of early tumor response after

irradiation by positron emission tomography with 2-amino-[3-11C]isobutyric acid. Oncology Reports, 33(5), 2361–2367. https://doi.org/10.3892/or.2015.3868

Tubin, S., Gupta, S., Grusch, M., Popper, H.H., Brcic, L., Ashdown, M.L., Khleif, S.N., Peter-Vörösmarty, B., Hyden, M., Negrini, S., Fossati, P., Hug, E. 2020. Shifting the Immune-Suppressive to Predominant Immune-Stimulatory Radiation Effects by SBRT-Partial Tumor Irradiation Targeting Hypoxic Segment (SBRT-PATHY). Cancers. https://doi.org/10.3390/cancers13010050

Vanhove, K., Graulus, G.-J., Mesotten, L., Thomeer, M., Derveaux, E., Noben, J.-P., Guedens, W., & Adriaensens, P. 2019. The Metabolic Landscape of Lung Cancer: New Insights in a Disturbed Glucose Metabolism. Front. Oncol., 9. https://doi.org/10.3389/fonc.2019.01215

Verhaegen, F., van Hoof, S., Granton, P. V., & Trani, D. 2014. A review of treatment planning for precision image-guided photon beam pre-clinical animal radiation studies. Zeitschrift Für Medizinische Physik, 24(4), 323–334. https://doi.org/10.1016/j.zemedi.2014.02.004

Verhaegen, F., Butterworth, K. T., Chalmers, A. J., Coppes, R. P., de Ruysscher, D., Dobiasch, S., Fenwick, J. D., Granton, P. V., Heijmans, S. H. J., Hill, M. A., Koumenis, C., Lauber, K., Marples, B., Parodi, K., Persoon, L. C. G. G., Staut, N., Subiel, A., Vaes, R. D. W., van Hoof, S., … Dubois, L. J. 2023. Roadmap for precision preclinical x-ray radiation studies. In Physics in Medicine & Biology (Vol. 68, Issue 6, p. 06RM01). IOP Publishing. https://doi.org/10.1088/1361-6560/acaf45n

Vogel, W. V., van Dalen, J. A., Wiering, B., Huisman, H., Corstens, F. H. M., Ruers, T. J. M., & Oyen, W. J. G. 2007. Evaluation of Image Registration in PET/CT of the Liver and Recommendations for Optimized Imaging. In Journal of Nuclear Medicine (Vol. 48, Issue 6, pp. 910–919). Society of Nuclear Medicine. https://doi.org/10.2967/jnumed.107.041517

Wang, J.-Y., Chen, K.-Y., Wang, J.-T., Chen, J.-H., Lin, J.-W., Wang, H.-C., & Yang, P.-C. 2002. Outcome and prognostic factors for patients with non-small-cell lung cancer and severe radiation pneumonitis. International Journal of Radiation Oncology, Biology, Physics, 54(3), 735–741. https://doi.org/10.1016/s0360-3016(02)02994-2

Wang, L. M., Yadav, R., Serban, M., Arias, O., Seuntjens, J., & Ybarra, N. 2023. Validation of an orthotopic non-small cell lung cancer mouse model, with left or right tumor growths, to use in conformal radiotherapy studies. In Z. Wang (Ed.), PLOS ONE (Vol. 18, Issue 4, p. e0284282). Public Library of Science (PLoS). https://doi.org/10.1371/journal.pone.0284282

Wicki, A., & Christofori, G. (n.d.). The Angiogenic Switch in Tumorigenesis. 67–88. https://doi.org/10.1007/978-3-540-33177-3_4

Wirsdörfer, F., Jendrossek, V., 2016. The Role of Lymphocytes in Radiotherapy-Induced Adverse Late Effects in the Lung. Front. Immunol. https://doi.org/10.3389/fimmu.2016.00591

Woods, K., Neph, R., Nguyen, D., & Sheng, K. 2019. A sparse orthogonal collimator for small animal intensity-modulated radiation therapy. Part II: hardware development and commissioning. Medical Physics, 46(12), 5733–5747. https://doi.org/10.1002/mp.13870

Wu, Q., Allouch, A., Martins, I., Modjtahedi, N., Deutsch, E., & Perfettini, J.-L. 2017. Macrophage biology plays a central role during ionizing radiation-elicited tumor response. Biomedical Journal, 40(4), 200–211. https://doi.org/10.1016/j.bj.2017.06.003

XStrahl. 2018. SARRP Quick Start Guide.

Young, H., Baum, R., Cremerius, U., Herholz, K., Hoekstra, O., Lammertsma, A. A., & Price, P. 1999. Measurement of clinical and subclinical tumour response using [18F]-fluorodeoxyglucose and positron emission tomography: review and 1999 EORTC recommendations. European Journal of Cancer, 35(13), 1773–1782. https://doi.org/10.1016/s0959-8049(99)00229-4

Yu, Y., Nie, Q., Wang, Z., Di, Y., Chen, X., & Ren, K. 2023. Targeting acetyl-CoA carboxylase 1 for cancer therapy. Front. Pharmacol., 14. https://doi.org/10.3389/fphar.2023.1129010

Zhan, N., Li, B., Xu, X., Xu, J., & Hu, S. 2018. Inhibition of FASN expression enhances radiosensitivity in human non-small cell lung cancer. Oncology Letters. https://doi.org/10.3892/ol.2018.7896

Zhang, J., Guo, Y., Mak, M., & Tao, Z. 2024. Translational medicine for acute lung injury. In Journal of Translational Medicine (Vol. 22, Issue 1). Springer Science and Business Media LLC. https://doi.org/10.1186/s12967-023-04828-7

Zhang, Z., Werner, F., Cho, H.-M., Wind, G., Platnick, S. E., Ackerman, A. S., Girolamo, L., Marshak, A., & Meyer, K. 2017. A framework for quantifying the impacts of sub-pixel reflectance variance and covariance on cloud optical thickness and effective radius retrievals based on the bi-spectral method. In In Radiation Processes in the Atmosphere and Ocean (IRS2016): Proceedings of the International Radiation Symposium (IRC/IAMAS), 16-22 April 2016, Auckland, New Zealand, AIP Conference Proceedings, (Vol. 1810, p. 030002,). https://doi.org/10.1063/1.4975502.